



Libraries and Learning Services

# University of Auckland Research Repository, ResearchSpace

## Copyright Statement

The digital copy of this thesis is protected by the Copyright Act 1994 (New Zealand).

This thesis may be consulted by you, provided you comply with the provisions of the Act and the following conditions of use:

- Any use you make of these documents or images must be for research or private study purposes only, and you may not make them available to any other person.
- Authors control the copyright of their thesis. You will recognize the author's right to be identified as the author of this thesis, and due acknowledgement will be made to the author where appropriate.
- You will obtain the author's permission before publishing any material from their thesis.

## General copyright and disclaimer

In addition to the above conditions, authors give their consent for the digital copy of their work to be used subject to the conditions specified on the [Library Thesis Consent Form](#) and [Deposit Licence](#).

# Implementation of a Channel Sounder for Indoor Millimetre Wave Systems at 60 GHz

Damla Güven

*A thesis submitted in fulfilment of the requirements for the degree of  
Master of Engineering in Electrical and Electronic Engineering,  
the University of Auckland.*

November 2018



## Abstract

Wireless communication networks are facing new challenges as mobile data traffic grows. The currently underutilised millimetre wave spectrum is expected to be key to address these challenges. The unlicensed 60 GHz band is one of the candidate frequency bands being considered for fifth generation (5G) wireless systems, particularly for short-range (in-door) communications. The propagation characteristics at millimetre wave frequencies are largely unknown, and investigation of the indoor channel using experimental measurements are needed to effectively utilise this spectral resource.

The research presented in this thesis describes a series of experiments to investigate the angular dependency of the 60 GHz channel in confined office environments. As part of this research, a 60 GHz channel sounder with a 1 GHz measurement bandwidth based on off-the-shelf components has been developed. The performance of the channel sounder was validated through comparisons to known theoretical propagation models. The experimental investigations in confined office environments demonstrate that the propagation of 60 GHz millimetre waves is dominated by the line-of-sight path between the transmit and receive antennas, and by the first- and second-order reflections from objects with smooth surfaces in the environment. Beam misalignment due to the narrow beamwidths of directional transmit and receive antennas is shown to result in increased path loss, suggesting that achieving adequate indoor coverage will be challenging without beam-steering, even in confined offices. This thesis also investigates 60 GHz propagation when the line-of-sight path between the transmitter and receiver is obstructed by the human body. In this case, first- and second-order reflections within the office are the only propagation mechanisms contributing to the received power. Inter-office measurement results between two adjacent offices demonstrate that drywall partitions are largely transparent at 60 GHz.



## Acknowledgments

Firstly, I would like to express my sincere gratitude to my supervisors Andrew Austin and Michael Neve for their contributions and encouragement throughout this journey. Their guidance helped me in all the time of research and writing of this thesis.

I also wish to thank Wai Leung Yeung for his technical support, and Yuen Zhuang Goh for his insightful comments and encouragement.

Finally, I would like to give my greatest gratitude to my parents and my brother for providing me with unfailing support and continuous encouragement.



## TABLE OF CONTENTS

	Page
1 Introduction . . . . .	1
2 Millimetre Wave Communication Systems . . . . .	5
2.1 Introduction . . . . .	5
2.2 The Millimetre Wave Spectrum . . . . .	5
2.3 Free Space Path Loss . . . . .	7
2.4 Propagation Mechanisms . . . . .	8
2.5 Characterising the Millimetre Wave Propagation Channel . . . . .	11
2.5.1 Deterministic Models . . . . .	11
2.5.2 Empirical Models . . . . .	12
2.6 Summary . . . . .	13
3 Millimetre Wave Indoor Channel Characterisation . . . . .	15
3.1 Introduction . . . . .	15
3.2 Measurements of the Indoor Millimetre Wave Channel . . . . .	15
3.2.1 Large Indoor Environments . . . . .	15
3.2.2 Angular Dependency . . . . .	19
3.2.3 Confined Indoor Environments . . . . .	19
3.3 Contributions of this Research . . . . .	20
3.4 Summary . . . . .	21
4 Channel Sounder System Architecture . . . . .	22
4.1 Introduction . . . . .	22
4.2 System Objectives . . . . .	22
4.3 Overview of the Channel Sounder Architecture . . . . .	23
4.4 Baseband Tone Generation . . . . .	26
4.5 Up- and Down-Conversion . . . . .	29
4.6 Impact of Hardware Impairments . . . . .	32
4.7 Post-Processing of the Received Signal . . . . .	34

	Page
4.8 Summary . . . . .	38
5 Channel Sounder Performance Validation . . . . .	39
5.1 Introduction . . . . .	39
5.2 The Two-Ray Propagation Model . . . . .	39
5.3 Description of the Experimental Configuration . . . . .	41
5.4 Extension to the Three-Ray Model . . . . .	44
5.5 Free Space Measurement in the Anechoic Chamber . . . . .	47
5.5.1 The Measurement Procedure . . . . .	47
5.5.2 Link Budget Analysis . . . . .	49
5.6 Summary . . . . .	50
6 Office Measurements with the Channel Sounder . . . . .	51
6.1 Introduction . . . . .	51
6.2 An Overview of the Measurement Phases . . . . .	51
6.3 The Measurement Procedure . . . . .	53
6.4 Phase A: In-Office Measurements . . . . .	56
6.4.1 Transmitter and Receiver Parameters . . . . .	56
6.4.2 LOS Measurement Results . . . . .	58
6.4.3 Corridor Measurement Result . . . . .	62
6.4.4 Path Loss Analysis . . . . .	63
6.5 Phase B: Impact of the Human Body . . . . .	65
6.6 Phase C: Inter-Office Measurements . . . . .	67
6.7 Summary . . . . .	71
7 Recommendations for Future Work . . . . .	72
7.1 Introduction . . . . .	72
7.2 System Hardware . . . . .	72
7.3 Experimental Recommendations . . . . .	73
7.3.1 LOS Measurement Recommendations . . . . .	73
7.3.2 NLOS Measurement Recommendations . . . . .	74
7.4 Summary . . . . .	74
8 Conclusions . . . . .	76

	Page
A An Alternative Transmitter Location . . . . .	79
B Impact of Increased Transmitter Height . . . . .	81
C Analysis of the Multipath Component . . . . .	83
REFERENCES . . . . .	85



## 1. INTRODUCTION

The wireless communications industry has a history of overcoming great obstacles. A new mobile generation has appeared nearly every 10 years since the first generation (1G) cellular systems were introduced in the early 1980s. Second generation (2G) digital systems were commercially deployed in 1992 with improved spectral efficiency and voice quality [1, p. 9]. The two most widely deployed 2G cellular systems were global system for mobile communications (GSM) based on time-division multiple access (TDMA) and IS-95 based on code division multiple access (CDMA) [1, p. 11–14]. In later releases of 2G standards, capabilities were introduced to support data transmission. However, the data rates were lower than existing dial-up connections, and the ever-increasing subscriber numbers made it obvious that new capacity was needed [2].

Third generation (3G) systems were first deployed in 2001, introducing high-speed mobile internet access for the first time. The air interface technology developed by the 3G partnership projects (3GPP) was called wideband CDMA, also known as the universal telecommunications systems (UMTS). Building on 3G systems, fourth generation (4G) system, e.g., Long Term Evolution (LTE), were first standardised in 2012 [1, p. 19]. Both 3G and 4G systems are widely deployed in current cellular networks [2]. It should be noted that 1G–4G systems have all used carrier frequencies below 3 GHz.

The introduction of smartphones and tablets in the past 10 years has enabled new capabilities, such as streaming high-definition video and many other data-heavy applications [3]. In 2016, approximately 1.5 billion smartphones were sold in the global mobile market [4]. Cisco has forecasted that by 2021, approximately 80 percent of global internet consumption will be video content, with an estimated growth in mobile video consumption of 54 percent per year [4]. This rapid growth implies cellular networks may need to deliver as much as 1000 times the capacity than current levels [5]. At the same time, future networks have to support massive connectivity with a diverse set of applications and services, such

as machine-to-machine communication and the Internet-of-things [3]. Efficient use of the limited spectral resources is required to accommodate these new and developing network deployment scenarios.

The initial obvious option to meet this large increase in data requirements is to improve the throughput of current LTE systems below 3 GHz, for example, via multiple-input-multiple-output (MIMO), carrier aggregation, heterogeneous networks, and a number of new interference management techniques. However, these techniques alone are not sufficient to meet the projected increase in data traffic, given the limited spectrum currently available below 3 GHz [6].

The alternative approach to address these challenges in increased data traffic is to use the currently underutilised millimetre wave spectrum between 30 and 300 GHz. The available bandwidth at these higher frequencies can easily be 200 times greater than current cellular allocations under 3 GHz [5], [7]. In particular, millimetre wave technologies can achieve much higher data rates by using simple air interfaces due to the large bandwidth. The candidate bands considered for the next generation (i.e., 5G) systems include 28 GHz, 38 GHz, 60 GHz and the 70 – 80 GHz bands [8, p. 5]. In particular, the unlicensed 60 GHz band (with a frequency range 57 to 66 GHz) has spurred the interest of radio engineers due to the availability of 5 – 7 GHz contiguous bandwidth in most countries.

The propagation characteristics at millimetre wave frequencies are considerably different from the currently used sub-3 GHz frequency bands. For example, these microwave bands provide favourable propagation characteristics, however, bandwidth is scarce. The millimetre wave frequencies do not penetrate solid materials very well, and experience high diffraction loss compared to sub-3 GHz frequency bands [8, p. 111]. However, there is an abundance of vacant spectrum in the millimetre wave bands. Accordingly, the move to millimetre wave frequencies necessitates an investigation of the propagation characteristics to understand how millimetre waves propagate in a variety of typical environments. As capacity challenges are mainly experienced in user-dense indoor environments (e.g., offices, shopping malls, train stations and airports [9]) millimetre wave systems are expected to be

widely deployed in such locations. However, each use-case scenario is required to be investigated *individually*, in order to gain insight into the design and deployment requirements at millimetre wave frequencies.

The primary focus of this thesis is to experimentally investigate the 60 GHz indoor propagation channel, and is organised as follows. Chapter 2 provides an overview of the millimetre wave spectrum and the propagation characteristics at millimetre wave frequencies. Also discussed in this chapter are deterministic and empirical modelling techniques to characterise the millimetre wave channel.

With this background on millimetre wave propagation, Chapter 3 reviews the literature related to measurements of the indoor channel at 60 GHz. In the published literature, several measurement configurations to characterise the propagation channel, and to investigate the angular dependency, are considered in large indoor environments. It is noted that confined office environments require further investigation, particularly at 60 GHz, and the major contributions of this thesis are outlined.

Chapter 4 introduces the channel sounder that has been developed for experimental measurements. The system objectives are used to propose a 60 GHz swept-tone channel sounder using off-the-shelf components. Chapter 4 also describes the stages in the signal chain to achieve frequency up- and down-conversion, and the impact of the hardware impairments. This is concluded by a discussion on the post-processing methodologies used to obtain an accurate estimate of the channel.

Before proceeding with experimental measurements to investigate the indoor millimetre wave channel, it is necessary to validate the performance of the channel sounder. In Chapter 5 the channel sounder performance is validated by comparing the measured signal to known theoretical propagation models. The frequency response of the channel sounder is also investigated in an anechoic chamber.

In Chapter 6 the angular response of the 60 GHz channel in a confined office environment is investigated using the channel sounder through a series of experiments. Also considered are inter-office propagation between two adjacent offices and the impact of obstructing the line-of-sight (LOS) path between the transmit and receive antennas. Recommendations for future work are presented in Chapter 7, which focuses on hardware improvements and future experimental investigations. This thesis is concluded in Chapter 8.

## 2. MILLIMETRE WAVE COMMUNICATION SYSTEMS

### 2.1 Introduction

In Chapter 1 it was noted that the increase in projected traffic demand can be met by (currently) underutilised millimetre wave bands. However, the considerably smaller wavelength can significantly change the propagation characteristics. The goal of this chapter is to provide an overview of the propagation characteristics of millimetre waves, and outline modelling techniques to investigate the millimetre wave channel.

Section §2.2 outlines the millimetre wave spectrum, focusing specifically on the unlicensed spectrum available in New Zealand. Section §2.3 investigates the free space path loss at millimetre wave frequencies which is a useful starting point to estimate the large-scale channel characteristics. In section §2.4, the interaction of millimetre waves with the environment is discussed. This is further developed in section §2.5, which focuses on methods to characterise the millimetre wave channel. The major findings of this chapter are summarised in section §2.6.

### 2.2 The Millimetre Wave Spectrum

The millimetre wave spectrum is formally defined as the spectrum between 30 to 300 GHz [8, p. 6]. The available spectrum at these higher frequencies can be 200 times higher than current cellular allocations under 3 GHz [5], [7]. To address the challenges of rapid growth in traffic and achieve considerably high network capacity, one possibility is to use large bandwidth available in this underutilised millimetre wave spectrum.

Many countries worldwide have followed the recommendations of the International Telecommunications Union (ITU), and designated frequencies between 57 to 66 GHz (the 60 GHz band) for use in unlicensed communications applications. For example, in the United States, the Federal Communications Commission has made bands from 57 to 64 GHz available [10].

Similarly, Korea and Japan designated bands from 57 to 66 GHz and 59 to 66 GHz [11], respectively. Australia has allocated a smaller portion of spectrum, from 59.4 to 62.9 GHz [12], while New Zealand has presently unallocated spectrum from 66 GHz to 71 GHz [13]. It should be noted that the Radio Spectrum Management unit within the New Zealand government plans to revisit allocation of frequency bands above 30 GHz after 2019 World Radiocommunication Conference [14].

While a significant portion of the 60 GHz spectrum remains unlicensed worldwide, the propagation characteristics at these frequencies are different in many respects compared to the currently used sub-3 GHz spectrum. For example, at 60 GHz a propagating electromagnetic wave interacts strongly with atmospheric oxygen, experiencing an attenuation of 20 dB/km attenuation [15]. However, this high absorption is not present at other millimetre wave bands, such as 28, 38, and 72 GHz, providing feasibility for long-range outdoor communication at these frequencies [15]. In particular, systems operating around 28 GHz, which is the boundary between microwave and millimetre waves, is currently being considered by many countries for early 5G deployments. For example, in Korea and the United States 5G systems operating at frequencies between 27.5 to 29.5 GHz have been proposed. Similarly, in New Zealand frequency ranges from 24.25 to 27.5 GHz are also being considered [14]. Hereafter, the propagation characteristics of millimetre waves in the 60 GHz band will be discussed.

Atmospheric attenuation and increased path loss (discussed in section §2.3) at 60 GHz make this frequency band unfavourable for long-range (outdoor) communications. While this is initially considered as a disadvantage, the shift from long-range communications actually benefits short-range applications. Examples of short-range applications are systems reusing same frequencies and deployed in close proximity to each other, e.g., wireless local area network (WLAN) and cellular systems. Analogous to femtocell concept [5], 60 GHz systems could potentially be placed in user dense (indoor) environments which rely on short-range communications.

In order to gain insight into planning and deployment strategies for millimetre wave systems, it is essential to investigate the propagation characteristics. The analysis of free space propagation of electromagnetic waves is a useful starting point, in order to illustrate the differences between millimetre wave bands and conventional microwave bands.

### 2.3 Free Space Path Loss

For a receiver located at a separation distance  $d$  from the transmitter in free space, the received power,  $P_r$  (in Watts), is proportional to the product of effective isotropic radiated power ( $\text{EIRP} = P_t G_t$ ), the effective aperture of the receiver antenna ( $A_e = e_{max} A_{max}$ ), and the inverse square of the propagation distance  $d$ , that is given by Friis path loss equation [8], [8, p. 102]

$$P_r = \frac{\text{EIRP}}{4\pi d^2} (A_e) = \frac{P_t G_t G_r}{L} \left( \frac{\lambda}{4\pi d} \right)^2, \quad (2.1)$$

where  $\lambda$  is the wavelength,  $P_t$  (in Watts) is the transmitted power,  $G_t$  and  $G_r$  are the linear transmitter and receiver antenna gains, relative to an isotropic antenna, respectively, and  $L$  is the system loss factor not related to propagation. The system loss factor accounts for losses associated with antennas and components (e.g., filters, feeders). In (2.1) the path gain is denoted with the term  $\left( \frac{\lambda}{4\pi d} \right)^2$ , and the path loss is the reciprocal of the path gain, i.e.,

$$\text{PL} = \left( \frac{4\pi d}{\lambda} \right)^2. \quad (2.2)$$

(2.2) indicates that path loss increases with separation distance,  $d$ , or as the wavelength is decreased. The wavelength ( $\lambda$ ) and frequency ( $f$ , in Hz) of a propagating wave are related by the speed of light,  $c_o = \lambda f$ , where  $c_o \approx 3.0 \times 10^8$  m/s. Thus, for a fixed separation distance, and assuming isotropic transmitting and receiving antennas (with gains of  $G_r = G_t = 1$ ), the free space path loss is proportional to the square of the operating frequency.

In order to illustrate the impact of frequency on path loss, in Table 2.1 the free space path loss (in dB) at 5 GHz (modern WLAN) is compared to 60 GHz. For this comparison, no system losses ( $L = 1$ ), equal transmitted powers and omnidirectional antennas are assumed,

	$f_c = 5 \text{ GHz}$	$f_c = 60 \text{ GHz}$
$d = 1 \text{ m}$	46.4 dB	68 dB
$d = 10 \text{ m}$	66.4 dB	88 dB
$d = 100 \text{ m}$	86.4 dB	108 dB
$d = 1000 \text{ m}$	106.4 dB	128 dB

Table 2.1.: Path loss (in dB) at 5 GHz and 60 GHz in free space.

and the linear path loss is calculated using (2.2) for  $d = 1, 10, 100 \text{ m}$  and  $d = 1000 \text{ m}$ . As shown in Table 2.1, there is an additional 21.6 dB path loss at 60 GHz compared to 5 GHz, when omnidirectional antennas are assumed.

However, the benefit of millimetre wave frequencies is that shorter wavelengths allow directional antennas with higher gain and smaller physical size than a comparable sub-millimetre wave antenna. Additionally, the smaller wavelength enables large numbers of miniaturised antennas to be packed in radio frequency circuits, which can be used to form very high gain and electrically steerable arrays at the base station and in the skin of a cellphone [5, 16, 17].

However, without a clear line-of-sight (LOS) propagation path, the Friis path loss equation does not represent indoor (and urban) millimetre wave channel. In reality, these propagation environments are rich in various types of environmental clutter that interact with the electromagnetic waves, resulting in a variety of propagation mechanisms. In the following subsection, the three dominant propagation mechanisms will be outlined and their relevance to millimetre wave system explained.

## 2.4 Propagation Mechanisms

*Diffraction* is the mechanism by which electromagnetic waves ‘bend’ around obstacles in an environment. This propagation mechanism also allows electromagnetic waves to be received in regions not in the LOS of the transmitter, i.e., in the ‘radio shadow’ [18, p. 128]. Fig. 2.1 shows some of the potential propagation mechanisms for a generalised indoor en-

vironment. Energy of propagating waves arrive at the receiver via several paths simultaneously and a *multipath* situation exists in which various incoming electromagnetic waves arrive from different directions with different time delays [19, p. 114]. In the case of diffraction, the propagating wave between TX and RX 1 bends around the object obstructing RX 1, as shown in Fig. 2.1. While in current cellular systems (typically operating below 3 GHz) diffraction is responsible for carrying a large proportion of the power to shadowed regions, at millimetre wave frequencies the diffraction loss for the same scenario is considerably higher with ‘sharp’ shadow boundaries. For example, the difference in received signal power as a receiver is moved around a building corner, i.e., transitioning from LOS to non-line-of-sight (NLOS), was found to be 30 dB over approximately 20 cm at 60 GHz [20].

*Reflection* occurs when a wave propagating in a medium encounters an object with a ‘relatively’ smooth surface. When a wave is incident upon a smooth surface, a *specular reflection* occurs, such that the energy of the propagating wave is reflected at an angle equal to the angle of incidence. In Fig. 2.1, a first order reflection occurs from the smooth surface of a glass before reaching RX 2. Higher order ( $n$ th order) reflections can also exist, where  $n$  refers to the number of times a component is reflected before reaching the receiver.

Additionally, *scattering* of energy can also contribute toward the received power. Electromagnetic waves can be scattered from objects with rough surfaces, or objects that are physically smaller than the wavelength. In contrast to specular reflection, when a wave is incident upon a rough surface, the reflected wave is diffused over a range of angles. As shown in Fig. 2.1, electromagnetic waves can be scattered from rough surfaces, such as wooden doors, and other furniture. It should be noted that scattered components measured by RX 2 are represented by a single ray. Fig. 2.1 also shows the LOS (direct) path between TX and RX 2, which is free of obstructions. RX 2, thus, measures a combination of the LOS path and multipath components, including the scattered components and first order reflection.

At millimetre wave frequencies diffraction losses are considerably high, and accordingly, reflection and scattering propagation mechanisms dominate the received power. For example, outdoor measurements performed at 38 GHz and 60 GHz suggested that urban reflectors

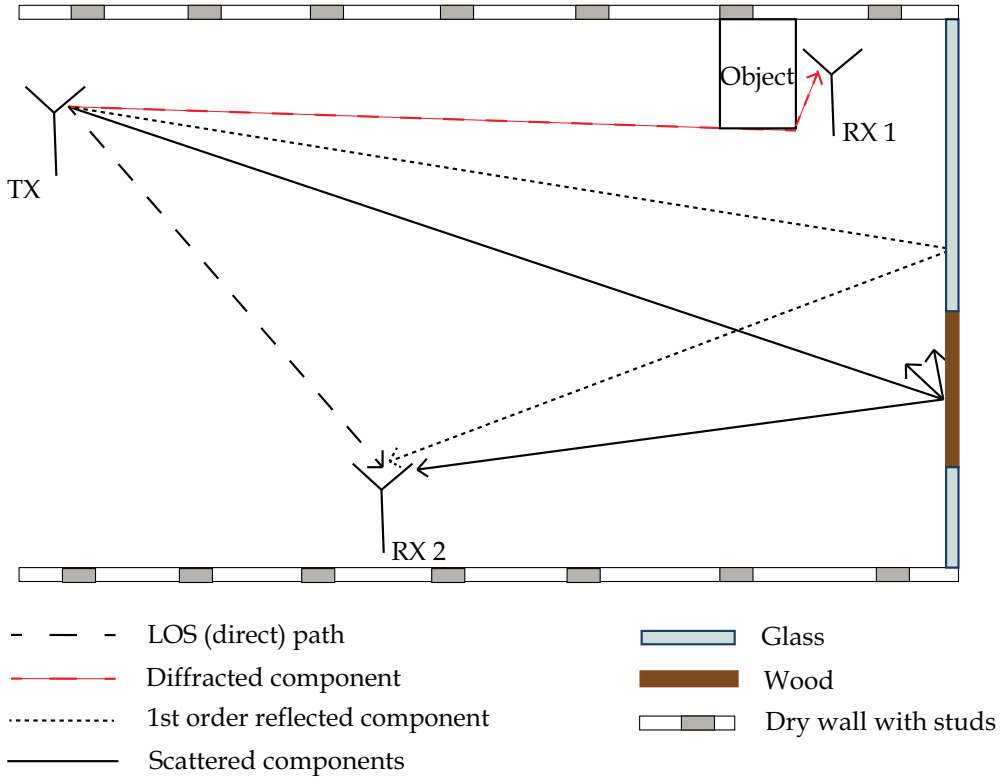


Fig. 2.1.: Propagation mechanisms in an indoor environment.

and scatterers, such as aluminum-sided buildings and lampposts, can aid in establishing viable communication links between the transmitter and receiver [21]. Similarly, measurement results performed at Helsinki airport showed reflections dominated the indoor propagation channel, where reflection from walls, floors and ceiling structures had a significant contribution to the received power levels [22].

The migration to millimetre wave frequencies introduces changes to the propagation channel, such as increased path loss and less reliance on diffracted components. These changes will also have an impact on system deployment strategies. Knowledge of the radio channel is crucial for design, deployment and optimisation of future millimetre wave systems. Accordingly, there is a need for further investigations of the millimetre wave propagation channel using *deterministic* and *empirical* techniques.

## 2.5 Characterising the Millimetre Wave Propagation Channel

### 2.5.1 Deterministic Models

Propagation models are widely used in routine wireless system planning, particularly for conducting feasibility studies, and can be broadly categorised into two categories: *deterministic* and *empirical*. Deterministic propagation models are based on electromagnetic theory, and typically require a detailed characterisation of the propagation environment. An example is the finite-difference time-domain (FDTD) method, which is based on numerical approximations to Maxwell's equations [23]. In the FDTD method, Maxwell's equations in partial differential form are discretised to central-difference equations and implemented on a computer. The FDTD method offers many advantages as a time-domain modelling and simulation tool, including implementation over wide range frequencies and accurate estimates of electric and magnetic field distributions [24]. However, the major disadvantage of the FDTD method is the excessive computational resources required, particularly for electrically large problems, such as propagation modelling at high frequencies [25].

Another category of deterministic methods are based on ray-optical approximations, i.e., geometrical optics (GO) and the uniform theory of diffraction (UTD) [19, p. 203–210]. While ray-optical models can accurately determine the reflection effects, the complex scattering phenomenon are only approximated via the UTD. In particular, the UTD is only strictly valid for perfectly conducting wedges [24]. However, for many commonly encountered indoor and outdoor environments diffraction occurs around inhomogeneous dielectric objects. Thus, in general ray-optical methods must be applied to propagation problems with caution.

A detailed description of the propagation environment, such as accurate sizes of objects and composition of indoor partitions, are essential for the successful application of deterministic methods to model the propagation channel. In particular, resolution of the geometrical model of the environment is required to be on the order of the wavelength (e.g.,  $\lambda = 5$  mm for 60 GHz band). The inherent trade-off between the detail included into the model to obtain accurate results, and the computational cost, suggests that deterministic models *alone* cannot be used to characterise the millimetre wave propagation channel. Furthermore, in

many cases the high level of uncertainty in the geometrical description of the environment leads to large uncertainties in the results produced by deterministic methods [26]. Given the limitations of deterministic models, a widely used alternative are empirical models, based on experimental measurements performed in actual propagation environments.

### 2.5.2 Empirical Models

Empirical models are based on experimental measurements, and therefore avoid approximations about the geometry of the propagation environment and the dielectric properties of materials. A variety of wideband channel measurements in the literature have been performed with a vector network analyser (VNA) [27], [28]. A major advantage of the VNA-based approach is the considerably large frequency bandwidth that can be measured (e.g., 4 GHz [29]). However, a disadvantage is that the transmitter and receiver subsystems are physically contained within the same unit, restricting the maximum achievable separation distance between the transmit and receive antennas. Furthermore, VNA-based systems can be expensive, particularly at millimetre wave frequencies.

As an alternative to VNA-based systems, channel sounders can be constructed from off-the-shelf (OTS) components at relatively little cost. A widely used channel sounding method is based on *sliding correlation* [19, p. 238]. The sliding correlator channel sounder uses pulse compression techniques based on pseudo noise sequences, and the channel impulse response is obtained by correlating the received baseband signal with the original transmitted sequence. However, the system architecture of sliding correlator channel sounders can be relatively complex, particularly, due to difficulties inherent in implementing floating point gate arrays and direct frequency synthesisers [30].

Similarly, channel sounders based on a *swept-tone* architecture can also be implemented using OTS components. The swept-tone approach enables characterisation of the propagation channel via a frequency sweep, where complex frequency tones are transmitted and received at each frequency step over the channel bandwidth.

The major disadvantage of channel sounders implemented with OTS components compared to the VNA-based approach, besides the higher development effort required to construct the system hardware, is that the maximum bandwidth is limited by suitable OTS components, e.g., most analog-to-digital converters (ADC) have limited sampling bandwidth. However, as the transmitter and receiver subsystems are located on separate modules, larger separation distances between the transmit and receive antennas can be considered for experimental measurements.

The channel measurements presented in this thesis are performed with a channel sounder based on a swept-tone architecture. The system architecture will be described in detail in Chapter 4.

## 2.6 Summary

The unlicensed 60 GHz band is one of the candidates considered for millimetre wave systems. The propagation characteristics of millimetre waves are different in many respects compared to sub-3 GHz radio waves currently used. In particular, smaller wavelength leads to increased path loss, and accordingly need for highly directional antennas. Furthermore, reflection and scattering become the primary propagation mechanisms, as diffraction loss increases significantly.

While ray-optical methods are reasonable deterministic methods to model the propagation channel, especially to identify multipath components, the high computational time due to need to finely resolve the propagation environment, suggests that models based on experimental measurements are needed to investigate and characterise the propagation channel. Channel sounders constructed with OTS components are widely used for wideband channel characterisation at millimetre wave frequencies due to the advantages in terms of cost and usability.

The intrinsic properties of the 60 GHz band, such as the oxygen absorption and increased path loss, makes this frequency band viable for short-range communications. In particular, user-dense indoor environments in need of capacity favour short-range communications

systems. Examples of such indoor environments are, office-buildings, train stations and airports. In Chapter 3, various indoor studies performed at 60 GHz will be discussed, with a particular focus on the measurement configurations and observations about the propagation characteristics.

### 3. MILLIMETRE WAVE INDOOR CHANNEL CHARACTERISATION

#### 3.1 Introduction

In current cellular communication systems operating with frequencies less than 3 GHz, propagation of radio waves from outdoor base stations plays a major role in providing coverage to indoor users. These radio waves have to propagate through building walls and windows, which cause high penetration loss resulting in a significant degradation in received data rates and spectral efficiencies. The penetration loss will be higher at millimetre-wave frequencies, which do not penetrate solid materials very well and can be easily absorbed by rain and foliage [31]. Additionally, as discussed in section §2.4, diffraction loss at millimetre wave frequencies is significantly higher than at microwave frequencies. Therefore, one of the key considerations for designing future 5G cellular architectures is to separate outdoor and indoor use-case scenarios, so that penetration loss through building materials can be avoided, and the capacity issues experienced in areas with high user density can be mitigated [32], [5]. The aim of this chapter is to present the findings of literature studies on indoor measurements at 60 GHz, and outline the contributions of this thesis.

The literature consists of various studies and measurement methodologies which consider different indoor environments for millimetre wave deployment at 60 GHz. The findings of these indoor studies are presented in section §3.2, which is followed by the contributions of this thesis in section §3.3. Section §3.4 provides a brief summary of this chapter.

#### 3.2 Measurements of the Indoor Millimetre Wave Channel

##### 3.2.1 Large Indoor Environments

Extensive research has been conducted on indoor propagation channel in the 60 GHz band, one of the most promising candidates for multi-gigabit short-range wireless communi-

cations systems. Table 3.1 summarises the indoor studies reported in this section, where the main outcomes of the research, measurement methods, considered bandwidths, and antenna types are provided.

The preliminary research in early 1990s mainly focused on the statistical parameters and models at 60 GHz. Smulders *et al.* performed frequency domain measurements using a VNA across a 2 GHz bandwidth centred at 58 GHz in small and large indoor environments [33]. Using biconical horn antennas for the wideband channel measurements, the results showed an increasing delay spread with increasing size of the room.

Geng *et al.* performed channel measurements in various indoor environments at 60 GHz using a VNA with directional horn antennas for the transmitter and receiver [34]. The propagation mechanisms were investigated based on direction-of-arrival (DOA) measurements. A strong relationship between the multipath channel structure and propagation environment was observed. In LOS cases, it was observed that the direct path and first-order reflected waves from glass window and doors (with smooth surfaces) were the main contributors to the received power. In NLOS locations, the received signals were found to be highly dependent on the wall composition [34]. This study also measured the path loss exponents (PLEs), which were found to be 1.6 in the LOS corridor, 2.2 in the LOS hallway, and 3.0 in the NLOS hallway cases.

Reference	Year	Measurement Method	Bandwidth	TX/RX Antenna Type	Indoor Measurement Environment	Main Research Outcomes
Smulders <i>et al.</i> [33]	1992	VNA-based channel sounder	2 GHz	Biconical horn	Small and large room	Delay spread increases with the size of the room.
Xu <i>et al.</i> [28]	2002	Sliding correlator	200 MHz	Directional horn	Hallway, medium room	LOS: Image-based ray tracing techniques can be applied to determine the multipath components.
Anderson and Rappaport [35]	2004	Sliding correlator	400 MHz	Pyramidal horn	Building floor	NLOS: Penetration losses depend on the position of the wall studs.
Zwick <i>et al.</i> [36]	2005	Sliding correlator	5 GHz	Omnidirectional	Corridor, office	Propagation of 60 GHz confined to small areas due to high penetration losses.
Maltsev <i>et al.</i> [37]	2009	Channel Sounder	800 MHz	Directional horn	Conference room	Multipath propagation can benefit the channel when the strongest transmission path is blocked.
Geng <i>et al.</i> [34]	2009	VNA-based channel sounder	100 MHz	Directional horn	Hallway, corridor	Received power obtained through LOS and reflected paths of first and second orders.
Sawada <i>et al.</i> [38]	2010	VNA-based channel sounder	3 GHz	Conical horn	Cubicle Office	LOS: Direct path and first-order reflections main contributors to received power. NLOS: Propagation is dependent on wall composition.
Kyro <i>et al.</i> [39]	2011	VNA-based channel sounder	4 GHz	Omnidirectional biconical and open-ended waveguide	Confined hospital room	Reflected waves can be treated as a single cluster for LOS cases.
Haneda <i>et al.</i> [29]	2015	VNA-based channel sounder	4 GHz	Directional horn/ Biconical omnidirectional	Railway station, shopping mall, office	Low path loss values are measured due to the presence of metal objects in the confined room.
Wu <i>et al.</i> [40]	2017	VNA-based channel sounder	2 GHz	Directional horn and uniform virtual array	Laboratory	Specular reflections contribute to 90% of the received power in the shopping mall, and railway station, 70% in the office environment.
Andrew C. M. Austin Michael J. Neve Danla Guven [41]	2018	Channel Sounder based on off-the-shelf components	1 GHz	Pyramidal horn	Confined office	Azimuth departure angles depend on antenna position and the environment, elevation departure angles on the antenna height difference.
						This paper reports on the development of a millimetre wave measurement channel sounder for characterising indoor wireless channels.

Table 3.1.: An overview of indoor propagation studies at 60 GHz.

In contrast to VNA-based measurements, Xu *et al.* used a sliding correlator with a bandwidth of 200 MHz [28]. The 60 GHz multipath components were resolved by mechanically rotating directional antennas. One of the main findings in LOS environments was that multipath components can be well predicted from image-based ray optical techniques. Furthermore, the LOS measurements indicated a PLE less than 2 in hallways. Similar to [34], the direct path and first-order reflections were found to contribute to the majority of the received power. Additionally, strong multipath components were introduced by metal furniture in the environment. For the NLOS measurements performed in a hallway, metal studs were found to introduce significant penetration loss of 35.5 dB, compared to 8.8 dB when these studs did not block the transmission path [28].

Zwick *et al.* studied the indoor channel at 60 GHz using a sliding correlator channel sounder with a heterodyne architecture. A total measurement bandwidth of 5 GHz was obtained by concatenating of multiple frequency bands [36]. A PLE of 1.33 was measured in the LOS office environment. Path loss values between 55 dB and 90 dB were measured with increasing transmitter and receiver separation distances in corridor and office environments. Additionally, it was observed that a wideband 60 GHz system can take advantage of multipath propagation in the environment when the strongest transmission path is blocked. This observation was made by subtracting the strongest multipath component from the received power delay profiles which resulted with a reduction of 6 dB in the total received power.

Similar results were also observed in experimental measurements of 60 GHz channel in a railway station, shopping mall, and office environment using a VNA-based channel sounder over a 4 GHz bandwidth [29], [42]. These measurements were performed using a directional horn antenna at the transmitter and a biconical (omnidirectional) antenna at the receiver. Specular reflections were observed to account for 90% of the received power in the shopping mall and railway station, and 70% in the office environment. In general, specular reflections dominated diffuse scattering due to the large size of the physical environments.

### 3.2.2 Angular Dependency

The inherently high path loss at millimetre wave frequencies necessitates the use of high gain directional antennas. However, the narrow beamwidth means the transmission path can be easily obstructed by objects, such as furniture in the environment [43], a moving person, or by the body of a user simply holding their device [44], [45]. In a residential environment, measurements performed with and without the presence of furniture indicated that objects obstruct walls and floors which are “quasi-specular” reflectors, noticeably increasing the energy dispersion for LOS situations [43]. Blockage of the LOS path by a person can result with attenuation of 20 dB in the direct path [44], [45].

A further complicating factor is the potential for beam misalignment between the transmitter and receiver, which may result in reduced received power levels. Urban measurements at 60 GHz showed that the strongest LOS/NLOS links suffer a 20% data rate drop due to a  $10^\circ$  beam misalignment, and an average drop of 50 – 100% due to a  $20^\circ$  beam misalignment [46]. In particular, NLOS links with weak received power levels were observed to be more sensitive to beam misalignment.

Therefore, angular characteristics of multipath propagation channels are essential for millimetre wave systems to utilise directional steering antennas and adaptive arrays [40]. Wu *et al.* investigated the 60-GHz channel in three-dimensional space by simultaneously measuring azimuth and elevation planes. During comparisons of the rotated directional antenna and uniform virtual-source methods in a VNA-based channel sounding system, azimuth departure angles were found to be highly diverse and related to the physical environment and antenna position, while the elevation departure angles were found to be related to antenna height differences [40].

### 3.2.3 Confined Indoor Environments

In 2004, Anderson and Rappaport conducted indoor wideband measurements at 2.5 GHz and 60 GHz using a broadband vector sliding correlator channel sounder [35]. For the 60 GHz

measurements performed on a floor of a modern office building, vertically polarised pyramidal horn antennas were used both at the transmitter and receiver. The PLE was found to be 2.1 with a standard deviation of 7.9 dB for the LOS cases on a building floor. Moreover, the results showed that the 60 GHz band would be more suitable for single-cell-per-room applications, as opposed to long-range systems, as millimetre wave signals were observed to experience high attenuation when propagating through internal partitions in a building [35].

It should be noted that little research has focused on the propagation of millimetre waves in confined office-type environments. Interestingly, measurements performed in hospital rooms (with medical equipment) revealed generally lower path loss and delay spread values compared to regular indoor offices and residential environments, which is thought to be affected by the presence of metal objects in the hospital environment [39].

The indoor propagation studies outlined in this chapter show that 60 GHz propagation is dominated by LOS path. Accordingly, a number of millimetre wave access points will be required to provide adequate coverage for indoor environments, possibly in multiple rooms for a residential house, and in every office for a business unit. In order to gain insight into deployment strategies, beam steering requirements, system performance, reliability and potential co-channel interference at these frequencies, it is essential to perform channel measurements in each type of indoor environment.

### **3.3 Contributions of this Research**

The majority of the published research on experimental measurements of the 60 GHz indoor propagation channel have focused on ‘large’ environments, such as laboratories or portions of a building floor. One indoor scenario that needs further investigation is 60 GHz propagation in a confined office environment. Such environments represent a likely deployment case for millimetre wave systems. Propagation in these environments is complicated by varying levels of environmental clutter. Moreover, system performance challenges could be faced, when an adjacent office is deployed with a separate access point reusing the same frequency, or when the transmission path of the antenna is obstructed by a person. There-

fore, the main contribution of this thesis is to develop a channel sounder to help improve the understanding of millimetre wave propagation at 60 GHz in confined office environments. Other contributions of this thesis include:

- performing experimental measurements with the channel sounder to characterise the indoor channel;
- investigation of the potential impact of human body blockage on the millimetre wave propagation; and
- analysis of inter-office propagation of millimetre waves at 60 GHz.

However, the channel sounder must be validated through comparisons to known theoretical channel models before proceeding with these measurements.

### **3.4 Summary**

This chapter described a number of studies that reported propagation measurements performed in various indoor environments at 60 GHz. Indoor environments were found to provide rich multipath, especially reflected and scattered energy in the 60 GHz band, particularly from objects with smooth surfaces. Moreover, the studies greatly reported that millimetre waves rely on the LOS path to achieve adequate received signal power, and that NLOS propagation depends on the composition of the internal partitions. Additionally, the need for directional high gain antennas to overcome the increased path loss requires an investigation of the angular dependency of the millimetre wave channel.

As previous research mainly focused on measurements performed in large propagation environments, the main contribution of this thesis is to investigate the 60 GHz propagation in a confined office environment. Chapter 4 describes the system architecture of the channel sounder that will be used to perform experimental measurements in a confined office.

## 4. CHANNEL SOUNDER SYSTEM ARCHITECTURE

### 4.1 Introduction

One of the main contributions of this thesis is to undertake a preliminary investigation of the 60 GHz indoor channel via experimental measurements. A variety of different channel measurement techniques have been reported to date (e.g., in Table 3.1). As mentioned in section §2.5, channel sounding techniques constructed with OTS components provide advantages in terms of cost and usability. Therefore, a channel sounder using OTS components will be developed to characterise the propagation channel at 60 GHz.

Section §4.2 outlines the objectives the hardware design must fulfil to perform channel characterisation at 60 GHz. These objectives are used to propose a channel sounder architecture as described in section §4.3. A discussion of baseband tone generation is then provided in section §4.4, followed by a discussion on the up- and down-conversion processes of the channel sounder in section §4.5. The homodyne transceiver architecture used in the system introduces unique challenges that are identified in section §4.6. Finally, section §4.7 describes the post-processing methodologies that are applied to obtain an accurate estimate of the channel. Section §4.8 briefly summarises this chapter.

### 4.2 System Objectives

The primary objective of the channel sounder is to enable a channel characterisation based on a *swept-tone* architecture at 60 GHz. Depending on the application, the new generation (5G) systems require instantaneous bandwidths of at least 500 MHz [3]. Accordingly, the proposed system needs a radio-frequency (RF) bandwidth of 1 GHz and must be assembled from available OTS components. The analog-to-digital converter (ADC) requires a high sampling rate to capture the entire 1 GHz bandwidth of the received signal. The system specifications of the channel sounder are summarised in Table 4.1.

Measurement Technique	Swept-tone architecture
Carrier Frequency	60 GHz
RF Bandwidth	1.0 GHz
Dynamic Range	60 dB
TX/RX Antenna Type	Pyramidal horn (Gain=17 dBi)
Sampling Rate	$\sim 2.0$ GSa/s

Table 4.1.: System specifications of the channel sounder.

Additionally, the channel sounder is required to provide a dynamic range of approximately 60 dB, as the indoor studies discussed in section §3.2 report path loss values in the range of 20 to 70 dB in indoor environments (for LOS and NLOS scenarios). High gain directional transmit and receive antennas are also required to account for the high path loss at 60 GHz. The use of high gain directional antennas necessitates an investigation of the angular dependency of the channel.

As the system specifications are now established, section §4.3 provides an overview of the channel sounder architecture.

### 4.3 Overview of the Channel Sounder Architecture

The swept-tone channel sounder uses a *frequency sweep* to characterise the millimetre wave channel. A frequency sweep is performed at a specified frequency step (e.g., 20 MHz) from 59.5 GHz to 60.5 GHz over a 1 GHz channel bandwidth. The passband is centred at 60 GHz corresponding to  $-500$  MHz to  $+500$  MHz in the baseband. At each given frequency step, complex frequency tones are generated and transmitted through the channel sounder. These frequency tones are sequentially captured by the receiver. The frequency response of each complex frequency tone provides the magnitude information. Accordingly, the frequency sweep consists of the received powers of the complex frequency tones that have been transmitted over the channel. The phase information in the frequency response is not preserved, however the angular dependency of the 60 GHz channel is investigated by

rotation of the receiver antenna in the azimuth plane.

Fig. 4.1 shows the system block diagram of the channel sounder. The transmitter and receiver subsystems operate over a bandwidth of 1 GHz with the local oscillator (LO) frequency,  $f_c$ , tuned to 60 GHz. Two phase-locked signal generators (Agilent E4438C) are used to generate the baseband in-phase (I) and quadrature (Q) sinusoidal signals with the same amplitudes. In this chapter, the signal generators generating the in-phase and quadrature signals will be referred to as ‘I-signal generator’ and ‘Q-signal generator’, respectively. The quadrature signal is obtained by introducing a phase offset of  $\phi = \pi/2$ , relative to the in-phase signal.

While the phase-locked signal generators share the same 10 MHz reference clock, each of them utilises an individual phase-locked-loop (PLL) that introduces a random phase error upon generation of a new sinusoidal signal. This random phase error adds to the target phase offset ( $\phi = \pi/2$ ) for the quadrature signal. Therefore, this phase error introduced by the signal generators needs to be measured and compensated before the in-phase and quadrature signals are fed into the transmitter. This is achieved by the oscilloscope feedback loop shown in Fig. 4.1. The in-phase and quadrature signals are connected to separate power splitters with one terminal connected to a balun [47] to obtain a differential signal, and the other terminal connected to the oscilloscope (MSO6104A). Section §4.4 focuses specifically on the baseband tone generation stage and describes the method for resolving the phase error introduced by the signal generators.

The channel sounder consists of the following OTS components:

- 57 – 66 GHz IQ up- and down-converters (SiversIMA FC2121V/01 and FC2221V/01, respectively [48], [49]);
- Two converter control boards (SiversIMA CO2201A<sup>1</sup>);

---

<sup>1</sup>The datasheet no longer available on: [www.siversima.com/product/converter-evaluation-board](http://www.siversima.com/product/converter-evaluation-board).

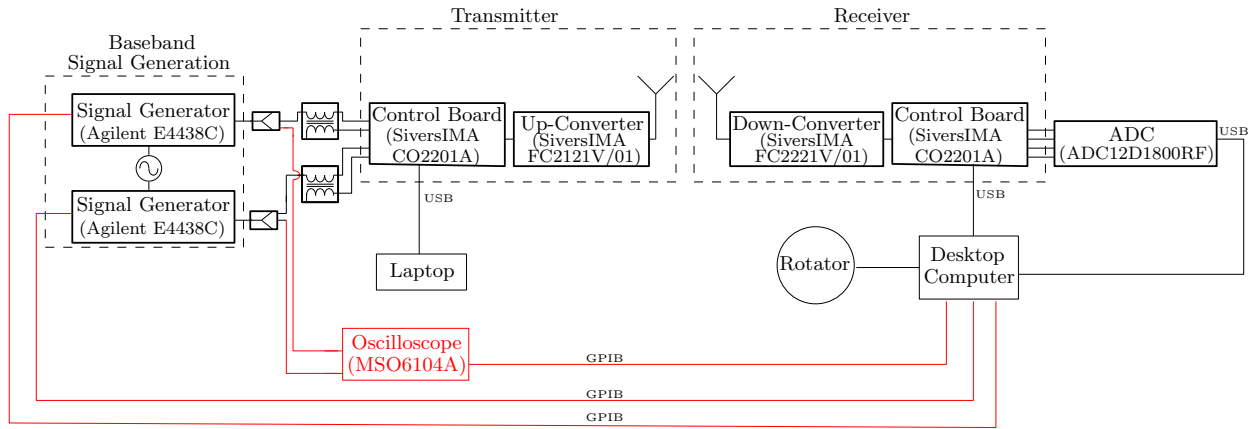


Fig. 4.1.: System block diagram with the baseband signal generation, oscilloscope feedback loop (in red), the transmitter and receiver, and the ADC.

- 50 – 75 GHz identical pyramidal horn antennas for the transmitter and receiver with a nominal gain of 17 dBi at 60 GHz, 26° vertical and 25° horizontal half-power beamwidths (Sage Millimeter SAR-1725-15-S2 [50]);
- ADC for baseband signal capture (Texas Instruments ADC12D1800RFRB [51]).

A dual-channel 12-bit ADC is used for baseband signal capture with a maximum sampling rate of 1.8 GSa/s [51] which samples the I- and Q-channels separately, and therefore, is sufficient to capture the entire 1 GHz bandwidth of the baseband signal. The total number of samples for the I- and Q- channels is  $2 \times 2^{14} = 32768$ .

As shown in Fig. 4.2, the up-converter is installed onto a vertical mount which has an open-ended waveguide aperture. The vertical mount with WR-15 mounting holes acts as an adapter between the up-converter and the transmit horn antenna. Also shown in Fig. 4.2 is the control board attached to a base mount. The receiver is similarly configured.

In Fig. 4.3 the ADC board is mounted above the receiver control board which is fixed onto a rotator that enables angular rotation in the azimuth plane. The angular dependency of the channel is investigated by rotating the receiver in the azimuth plane (from 0° to 360°). The axis of rotation is aligned with the centre of the waveguide aperture. The separation distance between the transmit and receive antennas is measured between the

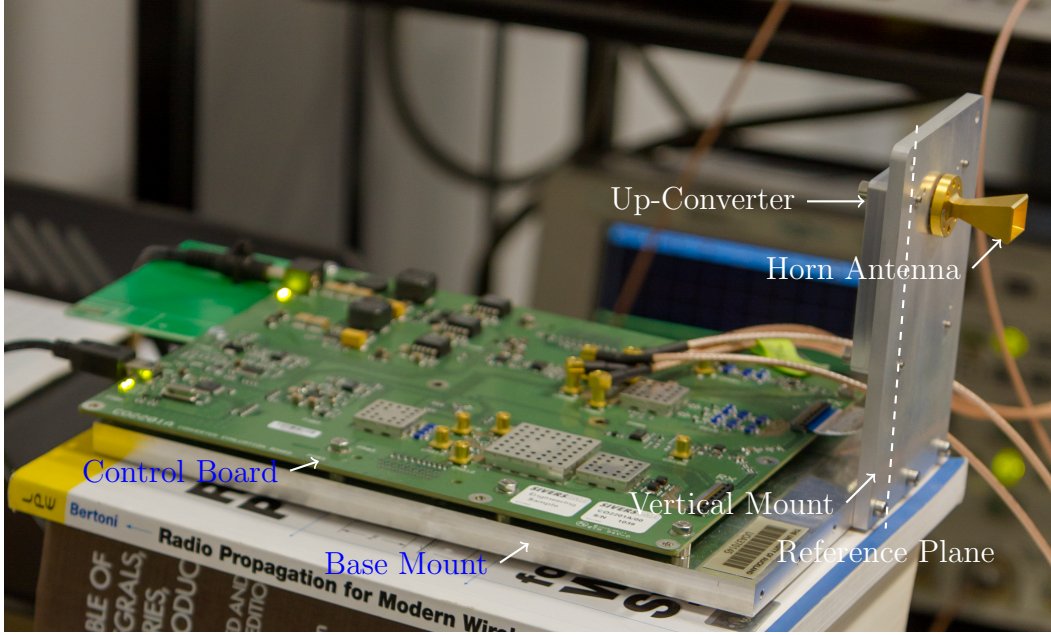


Fig. 4.2.: The transmitter configuration.

reference planes shown in Fig 4.2 and Fig. 4.3.

The up- and down-converter settings are configured via the control boards using the SiversIMA CO2201A control software<sup>1</sup>. The signal generators are connected via General Purpose Interface Bus (GPIB) and controlled using MATLAB®. The GPIB cables support a maximum distance of 20 m which corresponds to the maximum achievable separation distance between the transmitter and receiver with this configuration. However, this separation distance is sufficient to perform channel measurements in the proposed confined office environment. Similarly, the rotator is also controlled using MATLAB®. The data capture of the ADC is initiated and controlled via a C-program, and the post-processing of the received samples is performed using MATLAB®.

#### 4.4 Baseband Tone Generation

A homodyne architecture is used to modulate and demodulate the in-phase and quadrature signals. This architecture is also known as direct-conversion or zero-intermediate fre-

---

<sup>1</sup>This software is provided on a USB flash drive with the delivery of the SiversIMA CO2201A control boards.

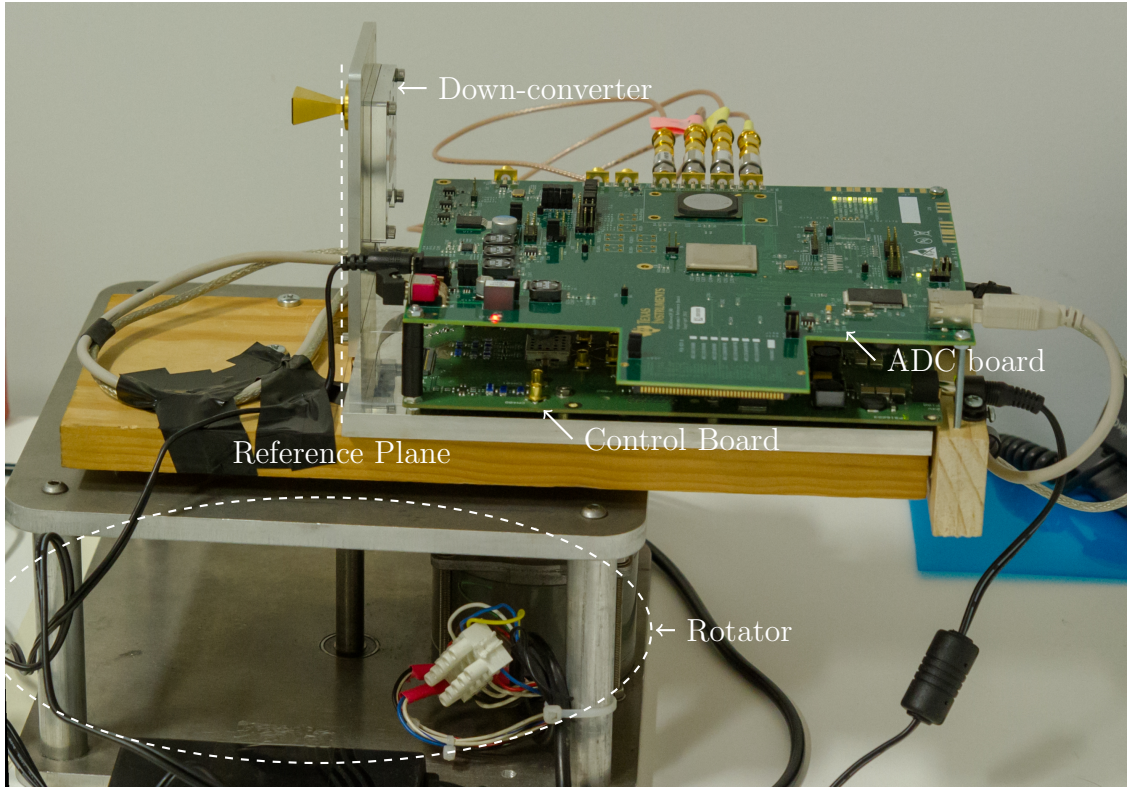


Fig. 4.3.: The receiver and ADC board are mounted onto the rotator.

quency (IF) transceiver, as the baseband signal is directly frequency up-converted to RF in transmission, and the RF signal is directly down-converted to a baseband signal in reception. [52, p. 10]. Fig. 4.4 shows the signal chain block diagram of the channel sounder. This section focuses on the first stage of this block diagram, i.e., the baseband tone generation.

The baseband in-phase signal at the transmitter input is

$$x_i(t) = A \cos(2\pi f t) , \quad (4.1)$$

where  $f$  is the baseband frequency, and  $A$  is the amplitude of the in-phase signal. The baseband quadrature signal is

$$x_q(t) = A \cos(2\pi f t + \phi) , \quad (4.2)$$

where  $\phi$  is the phase offset and ideally is equal to  $\pi/2$ . The baseband in-phase and quadrature signals given by (4.1) and (4.2), respectively, are generated using the signal generators shown in Fig. 4.1. Thus, the complex baseband signal at the transmitter input is given by

$$s_{BB}(t) = x_i(t) + jx_q(t). \quad (4.3)$$

Substituting (4.1) and (4.2) into (4.3), results in a single complex frequency tone at the transmitter input.

The baseband complex frequency in (4.3) is converted to a real passband signal by *up-conversion*, and its corresponding estimated received signal at the receiver is recovered to a complex baseband signal by *down-conversion* [8, p. 35]. Assuming ideal components and neglecting noise, signal propagation can be modelled as a linear time-invariant system,  $h(t)$  [8, p. 37]. The received passband signal is related to the transmitted passband signal through the convolution of the channel,  $y(t) = h(t) * x(t)$ , which is equivalent to  $Y(s) = H(s)X(s)$  in the frequency domain. For a sinusoidal input at a frequency, the output signal from the channel is a sinusoid at the same frequency, which is scaled in amplitude (and phase-shifted) [53, p. 472]. This property enables the channel sounder to recover the amplitude information of a transmitted frequency tone. In particular, the channel is characterised through a frequency sweep which necessitates each transmitted signal to be a single frequency tone.

The oscilloscope feedback loop shown in Fig. 4.1 corrects the initial phase error introduced by the signal generators. Specifically, the phase error of the quadrature signal is

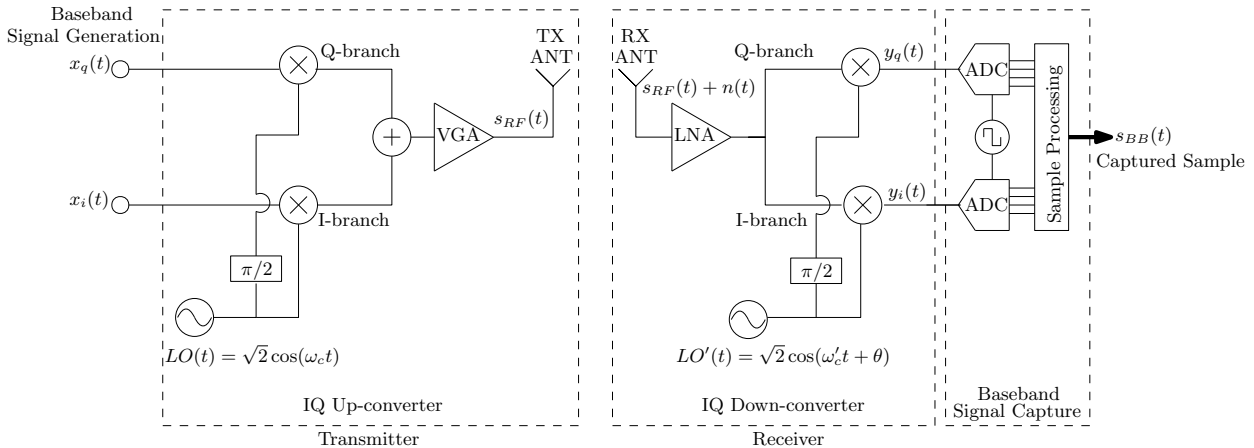


Fig. 4.4.: Signal chain block diagram of the channel sounder.

measured relative to the in-phase signal. This phase error is then subtracted, such that the in-phase and quadrature signals are aligned with zero phase offset. Once these signals are aligned, the Q-signal generator sets the target phase offset of  $\pi/2$ .

In order to investigate the case when  $\phi \neq \pi/2$  in (4.2), identical in-phase and quadrature signals with baseband frequencies of  $f = +200$  MHz have been generated, such that  $x_i(t) = x_q(t)$ . This baseband signal is directly connected to the ADC board via baluns. Fig. 4.5 shows the magnitude spectrum when the in-phase and quadrature signals are frequency tones at +200 MHz with  $\phi = 0^\circ$ . The strong DC tone observed in the centre of the spectrum is suppressed in the post-processing stage (described in section §4.8).

Fig. 4.5 shows two complex frequency tones at +200 MHz and -200 MHz with magnitudes of approximately 8 dBm. The tone observed at +200 MHz is the input frequency tone and its image is observed at -200 MHz. As shown in Fig. 4.5 the baseband spectrum consists of two frequency tones when  $\phi = 0^\circ$ . In order to obtain an accurate estimate of the amplitude information of the received frequency tone through the channel sounder, it is necessary that the baseband signal at the transmitter input consists of a single (complex) frequency tone. The two signal generators and the oscilloscope feedback loop shown in Fig. 4.1 ensure that the in-phase and quadrature signals described by (4.1) and (4.2), respectively, are generated and fed into the transmitter. The received magnitude spectrum of a single complex frequency tone will be investigated later in this chapter.

## 4.5 Up- and Down-Conversion

This section focuses on the IQ up-conversion and IQ down-conversion stages shown in Fig. 4.4. The up-converter consists of four variable gain amplifier (VGA) stages to amplify the RF signal to the desired amplitude for transmission [48]. In Fig. 4.4, these four VGA stages are represented by one VGA. In order to maximise the dynamic range of the system, all four transmit VGA stages are set to the maximum permitted value. It should be noted that the exact output transmit power from the VGA stages is undocumented and the thru standard to calibrate the system is unavailable. Thus, the transmit power will be

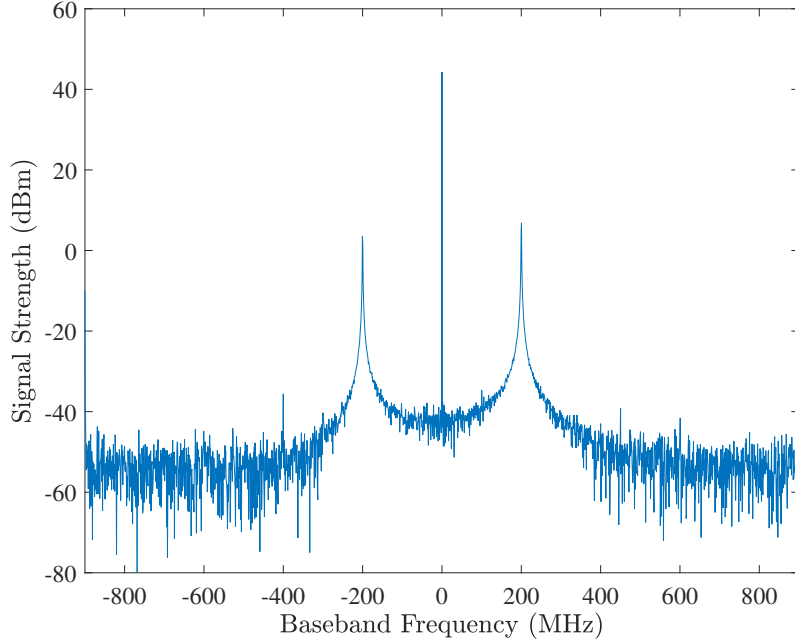


Fig. 4.5.: Received magnitude spectrum consisting of two frequency tones at  $-200$  MHz and  $+200$  MHz.

determined through free-space measurements in the anechoic chamber which is discussed in section §5.5. Additionally, the gain of the low-noise amplifier (LNA) in the down-converter is set to a third of the maximum linear gain, as this value was observed to provide an adequate trade-off between the received power and separation distances between the transmitter and receiver.

During the mathematical analysis to investigate the impact of frequency- and phase-offset of the receiver LO signal, the general expressions of  $x_i(t)$  and  $x_q(t)$  will be used, although the in-phase and quadrature signals are sinusoidal described by (4.1) and (4.2), respectively.

During the IQ modulation process,  $x_i(t)$  is mixed by the LO signal of  $\sqrt{2} \cos(\omega_c t)$  and  $x_q(t)$  by  $\sqrt{2} \cos(\omega_c t + \frac{\pi}{2})$ , as shown in Fig. 4.4. The modulated in-phase and quadrature signals are added and amplified by four VGAs before transmission (represented as a single VGA in Fig. 4.4). The signal at the transmitter output is [52, p. 32]

$$s_{RF}(t) = \sqrt{2} \Re \left[ s_{BB}(t) e^{j2\pi f_c t} \right] = x_i(t) \sqrt{2} \cos(\omega_c t) - x_q(t) \sqrt{2} \sin(\omega_c t), \quad (4.4)$$

where  $\omega_c = 2\pi f_c$  and  $f_c = 60$  GHz. The first stage of the receiver chain is the amplification of the received signal by the LNA. Ideally, the receiver LO signal should be identical to the LO signal in the transmitter. However, as the transmitter and receiver operate on separate LO sources, the received signal gets mixed with an LO signal which consists of the carrier frequency with a frequency- and phase-offset. Thus, the LO signal in the receiver is given by

$$LO'(t) = \sqrt{2} \cos(\omega'_c t + \theta), \quad (4.5)$$

where  $\omega'_c = \omega_c + \Delta\omega$  is the frequency-offset, and  $\theta$  is the phase-offset, relative to the transmitter LO signal. In the receiver, the real passband signal is recovered into a complex baseband signal. For simplification, the additive noise introduced by the channel is ignored. The baseband signal recovery is achieved as

$$\begin{aligned} s_{BB}(t) &= \left[ x_i(t) \sqrt{2} \cos(\omega_c t) - x_q(t) \sqrt{2} \sin(\omega_c t) \right] \sqrt{2} \cos(\omega'_c t + \theta) \\ &\quad + j \left[ x_i(t) \sqrt{2} \cos(\omega_c t) - x_q(t) \sqrt{2} \sin(\omega_c t) \right] \sqrt{2} \sin(\omega'_c t + \theta). \end{aligned} \quad (4.6)$$

After low-pass filtering to remove the  $2\omega'_c$  component, using trigonometric identities and substituting  $\omega'_c = \omega_c + \Delta\omega$ , the received complex baseband signal is

$$\begin{aligned} s_{BB}(t) &= x_i(t) \left[ \cos(\Delta\omega t + \theta) - j \sin(\Delta\omega t + \theta) \right] \\ &\quad + x_q(t) \left[ \sin(\Delta\omega t + \theta) - j \cos(\Delta\omega t + \theta) \right]. \end{aligned} \quad (4.7)$$

Additional to the transmitted baseband signal in (4.3), the recovered baseband signal in (4.7) consists of frequency tones, arising from the LO frequency- and phase-offsets. Thus, instead of recovering the received frequency tone as a pure signal, these non-linearities introduced during the demodulation can distort the received frequency tone [54].

While the homodyne receiver architecture is an attractive solution for the commercial market due to low-cost, low-power and wide bandwidth [55], it comes with a number of

unique challenges, including LO frequency- and phase-offsets, DC offset and I/Q imbalances. These hardware impairments will be discussed later in section §4.6.

#### 4.6 Impact of Hardware Impairments

In order to identify sources of hardware non-linearities in the channel sounder, a single complex frequency tone at +400 MHz is transmitted. In this measurement, the transmit and receive antennas were boresight aligned and placed approximately 800 mm apart, which is measured between the reference planes shown in Fig. 4.2 and Fig. 4.3.

Fig. 4.6 shows the received magnitude spectrum from the channel sounder when the input signal is a complex frequency tone at +400 MHz. A DC tone is observed at the centre of the baseband spectrum in Fig. 4.6 which results from the leakage of the receiver LO signal to the front-end LNA [55]. Specifically, the LO signal reflects from the LNA output back into the mixer RF input which then mixes with itself, resulting in a static DC tone [55]. In practice, the DC tone is suppressed in the post-processing stage with a digital filter (as discussed in section §4.7).

Moreover, homodyne transceiver systems suffer from additional errors that can take place as phase and amplitude imbalances in the local oscillator. These imbalances can be categorised either as a *phase mismatch* between the I- and Q- components of the local oscillator, or an *amplitude mismatch* due to gain differences of the mixers in the I- and Q-branches. These I/Q imbalances can occur during the modulation process in the transmitter and demodulation process in the receiver, resulting in an image tone of the originally transmitted frequency tone in the received baseband spectrum [52, p. 72].

In Fig. 4.6 the received baseband spectrum consists of two strong frequency tones at +400 MHz and -400 MHz with magnitudes of -9.4 dBm and -37.5 dBm, respectively. The frequency tone observed at +400 MHz corresponds to the originally transmitted frequency tone, and the tone at -400 MHz is its complex conjugate. The image rejection, i.e., the magnitude difference between the complex tone and its image, is 28.1 dB. In the literature carefully designed homodyne transceiver architectures were reported to be limited by

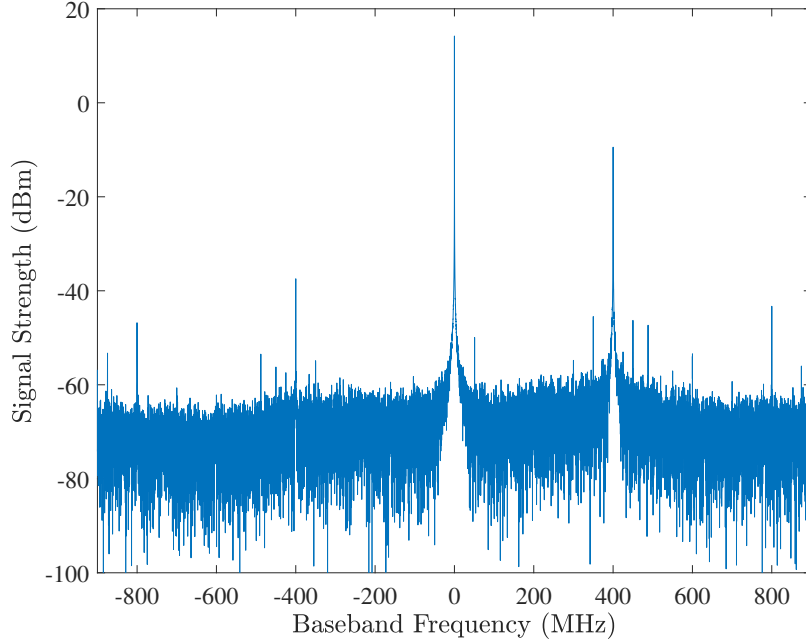


Fig. 4.6.: The magnitude spectrum for a single frequency tone transmitted through the channel sounder at  $f = +400$  MHz.

dynamic ranges of  $30 - 40$  dB [56]. Therefore, the image rejection obtained by the channel sounder is found to be appropriate.

Moreover, two distinct tones are observed in Fig. 4.6 at  $+800$  MHz and  $-800$  MHz with similar magnitudes of  $-43.3$  dBm and  $-46.8$  dBm, respectively. In particular, these tones are at twice the frequency of the transmitted complex tone, suggesting that these harmonics could be introduced in the analog baseband signal either in the transmitter or receiver side. The devices that could cause non-linearities in the analog baseband signal are the signal generators and the ADC in the transmitter and receiver sides, respectively.

Additional tones observed in Fig. 4.6 at  $\pm 490$  MHz,  $\pm 450$  MHz,  $\pm 350$  MHz possibly arise from the amplifiers in the transmitter and receiver. Power amplifiers are known to be highly non-linear devices in communication systems [57]. An additional source of non-linearity is the frequency and phase offsets introduced by the local oscillator according to (4.7). However, all these tones present in the baseband spectrum are approximately 40 dB

below the desired complex tone. Accordingly, they can be ignored.

#### 4.7 Post-Processing of the Received Signal

As noted in section 4.3, a frequency sweep is performed over the 1 GHz bandwidth from 59.5 GHz to 60.5 GHz to characterise the channel. Complex frequency tones are transmitted through the channel sounder at a specified frequency step. The ADC samples each received complex tone at a rate of 1.8 GSa/s. A number of  $2^{14} = 16384$  samples are captured by each I- and Q-channel of the ADC. The ADC full-scale-register (FSR) is  $V_{\text{FSR}} = 800$  mVpeak-to-peak which is the voltage range the ADC uses to convert the analog signal into a binary number. The step size (i.e., the voltage resolution) of the ADC is given by

$$\Delta V = \frac{V_{\text{FSR}}}{2^n}, \quad (4.8)$$

where  $n = 12$  bits [58]. The binary representations of the in-phase and quadrature signals are converted to a voltage by multiplication with  $\Delta V$  given by (4.8). The obtained voltage value,  $y$ , is converted to power (in dBm) by  $10 \log_{10}(y^2/R) + 30$ , where  $R = 50 \Omega$  is the baseband impedance [48], [49].

The DC tone in the centre of the baseband spectrum observed in Fig. 4.6 is suppressed by a moving average filter. This is implemented by convolving the in-phase and quadrature signals separately with a rectangular window which was found to be appropriate given the scope of this research. The average is then subtracted from the input signal. Therefore, the filtered signal,  $z[i]$ , is

$$z[i] = y[i] - \frac{1}{M} \sum_{j=-M/2}^{M/2} y[i+j] \quad (4.9)$$

where  $y[i]$  is the received baseband frequency tone and  $M$  is the length of the rectangular window, which is required to be wide enough to suppress the DC tone and avoid distortion of the desired frequency tone. An empirically determined window length of  $M = 100$  was found to be suitable for the moving average filter. A side effect of this process is that the output signal is truncated by the window length, therefore, reducing the number of sam-

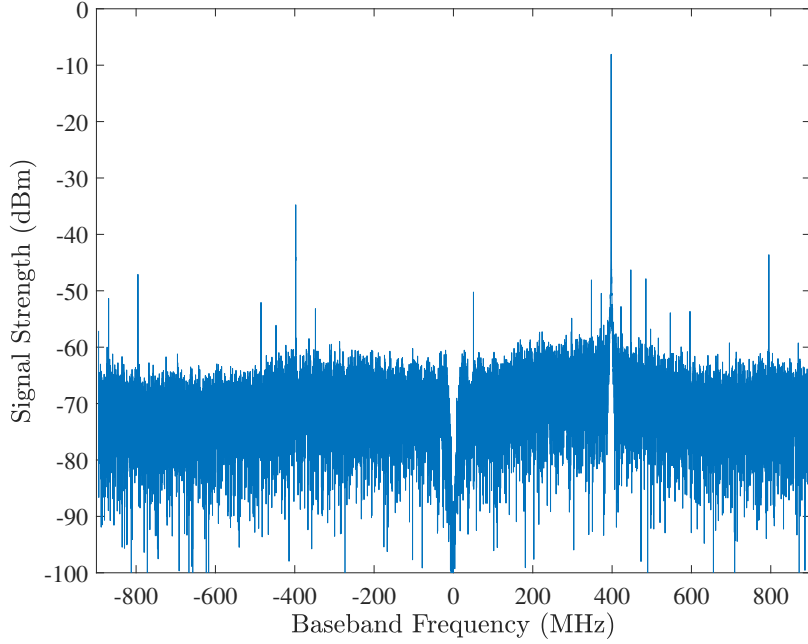


Fig. 4.7.: The magnitude spectrum for a single frequency tone transmitted through the channel sounder at  $f = +400$  MHz. The DC tone in the centre of the spectrum is removed with a moving average filter.

ples to 16284. Fig. 4.7 shows the received magnitude spectrum of the baseband frequency tone after applying the moving average filter using (4.9). It is observed that the DC tone is suppressed, and the originally transmitted complex tone at +400 MHz in the baseband spectrum has remained without distortion.

A frequency sweep with a 10 MHz frequency resolution was performed from 59.5 GHz to 60.5 GHz. Fig. 5.2 shows the measurement configuration with the transmit and receive open-ended waveguides boresight aligned and placed 480 mm apart (measured between the reference planes shown in Fig. 4.2 and Fig. 4.3). A total number of 100 complex frequency tones were received over the 1 GHz channel with a 10 MHz frequency resolution. The frequency response is directly computed by the fast Discrete Fourier Transform (DFT). The maximum magnitude in the received baseband spectrum represents the received power of the complex frequency tone at that frequency step. Fig. 4.8 shows the received power (in

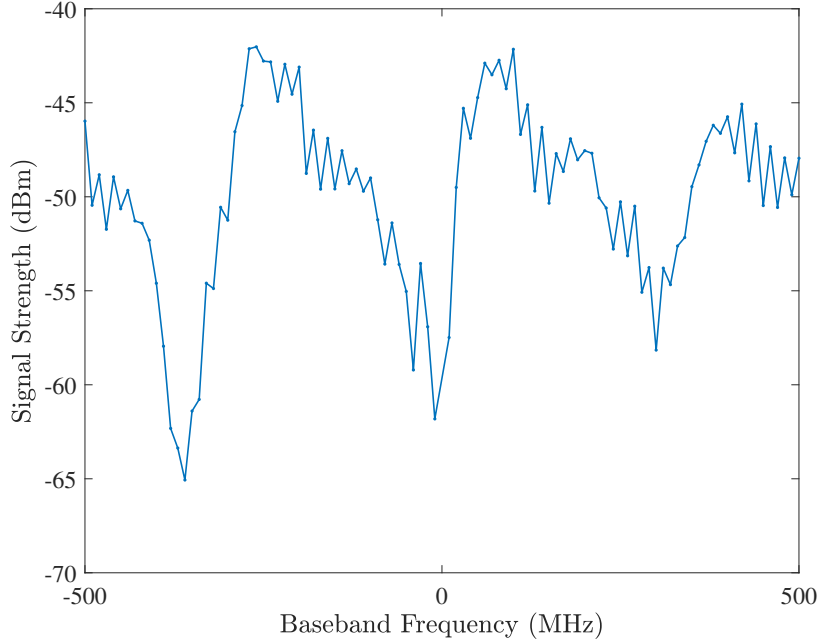


Fig. 4.8.: Frequency sweep computed with DFT.

dBm) of the frequency sweep performed with a 10 MHz frequency resolution<sup>1</sup>.

The frequency sweep in Fig. 4.8 shows two characteristics: small-scale variations with the received power varying within approximately 5 dB between frequency steps, and large-scale variations where the received power varies between  $-65.1$  dBm and  $-42.0$  dBm. The large-scale variations are thought to be introduced by the channel and will be discussed in section §5.3. The small-scale variations between adjacent frequency steps observed in Fig. 4.8 are resulting from *spectral leakage* which is an artefact of the DFT-based processing [53, p. 305].

The DFT calculates the spectrum at discrete frequencies which are  $\Delta f = F_s/N = 1.8 \text{ GHz}/16284 = 110.54 \text{ kHz}$  apart. The magnitude of complex tones that do not exactly fall onto the integer multiples of  $\Delta f$  ‘leaks’ into the surrounding frequencies. For example, in Fig. 4.7 the received signal at  $+400$  MHz falls onto the frequency bin  $397.7$  MHz and the power of the sample is shared between the surrounding frequency bins, e.g.,  $397.6$  MHz and

---

<sup>1</sup>The frequency sweep in Fig. 4.8 was performed using open-ended waveguides, therefore the received power levels are lower compared to that in Fig. 4.7, which was conducted with high gain horn antennas.

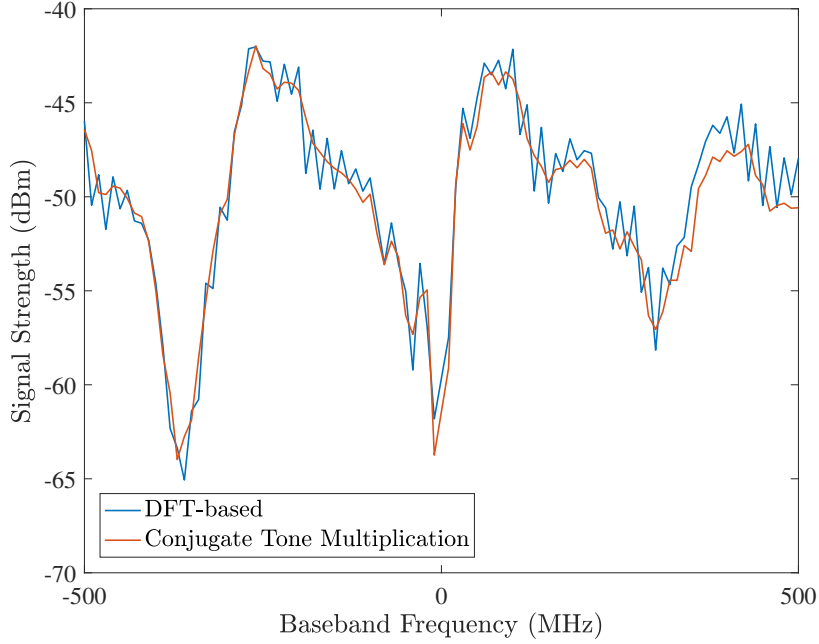


Fig. 4.9.: Comparison of the DFT and the complex conjugate multiplication methods.

397.8 MHz. This effect occurs at each complex frequency tone that does not fall onto  $\Delta f$  and is responsible for the small-scale variations observed in Fig. 4.8.

In order to overcome the spectral leakage, it can be noted the complex frequency tones are transmitted at a specified frequency step, and therefore, the frequency of the received frequency tone is already *known*. Thus, a vector of the conjugate frequency tones can be generated and multiplied with the vector of the input frequency tones,  $z[n]$ :

$$Z[k] = \frac{1}{N} \sum_{n=1}^N z[n] z^*[n] \quad (4.10)$$

where  $N$  is the number of samples, and  $z[n] = e^{-2\pi f_k n}$  with frequency vector  $f_k$ . In Fig. 4.9 the data set computed with DFT is compared to the method, where the input frequency tone is multiplied by its complex conjugate according to (4.10). In Fig. 4.9 the small-scale variations are reduced significantly when the magnitude of the frequency tones are calculated using (4.10). The power of the received frequency tones calculated with the proposed method provides an improved estimate of the measured frequency tone, as the magnitude of the *exact* frequency tone is computed.

#### 4.8 Summary

In this chapter, the system architecture of the swept-tone 60 GHz channel sounder constructed using OTS components was discussed. The channel sounder uses pyramidal horn antennas for the transmitter and receiver. A frequency sweep is performed using the channel sounder over a 1 GHz measurement bandwidth from 59.5 GHz to 60.5 GHz. The angular dependency of the 60 GHz channel is investigated by rotating the receiver in the azimuth plane.

The baseband tone generation and post-processing methodologies described in this chapter will be applied in the forthcoming channel measurements. Chapter 5 focuses on the performance validation of the channel sounder.

## 5. CHANNEL SOUNDER PERFORMANCE VALIDATION

### 5.1 Introduction

One of the contributions of this thesis is to use the channel sounder to experimentally investigate the millimetre wave indoor channel. Prior to conducting experimental measurements, it is necessary to validate the performance of the channel sounder. Therefore, the aim of the validation stage is to demonstrate that the transmitted and received signals are as expected. This is achieved by comparing the received signals to those predicted using theoretical channel models.

In Chapter 2, deterministic techniques to model electromagnetic wave propagation were discussed. In particular, it was noted that ray-optical techniques are well suited to model the propagation of millimetre waves. The two-ray model is considered for the validation of the received signals, and the mathematical derivation of this simple ray-optical model is described in section §5.2. Consequently, the experimental configuration for the performance validation is developed and described in section §5.3. This leads to a discussion of the experimental results and the extension to the three-ray channel model in section §5.4. In section §5.5, the transmit power of the channel sounder is determined by free-space measurements in the anechoic chamber. Finally, section §5.6 briefly summarises Chapter 5.

### 5.2 The Two-Ray Propagation Model

The two-ray channel model can be applied to characterise a simple propagation environment which consists of a line-of-sight (LOS) or direct ray propagating through free space, and a reflected ray resulting from reflection from the ground. The two-ray model is illustrated in Fig. 5.1.

The electric field of the direct component,  $\mathbf{E}_{dir}$ , at the receiving antenna is given by [59, p. 59]

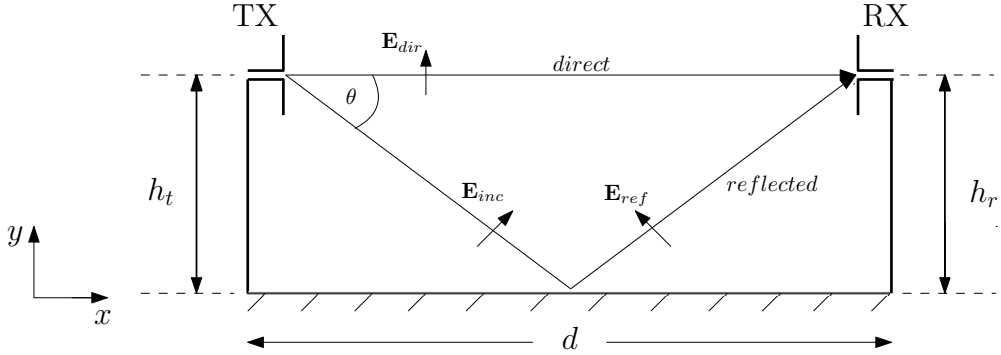


Fig. 5.1.: Two-ray model.

$$\mathbf{E}_{dir} = j \frac{e^{-jkL_{dir}}}{L_{dir}} \sqrt{\frac{\eta P_t}{2\pi}} \mathbf{a}_y F_{dir}(\phi, \theta), \quad (5.1)$$

where  $P_t$  (in Watts) is the transmitted power,  $L_{dir}$  the length of the direct ray,  $\mathbf{a}_y$  is the unit vector, and  $\eta$  (in  $\Omega$ ) the intrinsic impedance of free-space. In (5.1)  $k = 2\pi/\lambda$  is the wavenumber and  $F_{dir}(\phi, \theta)$  is the angular-dependent antenna pattern function.

Similarly, the reflected field,  $\mathbf{E}_{ref}$ , is given by

$$\mathbf{E}_{ref} = \rho j \frac{e^{-jkL_{ref}}}{L_{ref}} \sqrt{\frac{\eta P_t}{2\pi}} \mathbf{a}_y F_{ref}(\phi, \theta), \quad (5.2)$$

where  $L_{ref}$  is the length of the reflected ray,  $F_{ref}(\phi, \theta)$  is the angular-dependent antenna pattern function, and  $\rho$  is the reflection coefficient of the ground. For a perfectly conducting surface, the reflection coefficient is equal to +1 for vertical polarisation<sup>1</sup> [60, p. 345].

The total electric field at the receiver is given by

$$\mathbf{E}_{tot} = \mathbf{E}_{dir} + \mathbf{E}_{ref}. \quad (5.3)$$

The received power is obtained by determining the received open-circuit voltage,  $V_{oc}$ , defined by [60, p. 302]

$$V_{oc} = \mathbf{h} \cdot \mathbf{E}_{tot}, \quad (5.4)$$

---

<sup>1</sup>It should be noted that the reflection coefficient is *not* equal to  $-1$ , as this would be the case for horizontal polarisation.

where  $\mathbf{h}$  is the complex effective length parameter of the receiving antenna, given by

$$\mathbf{h} = \frac{2}{k} \sqrt{\frac{\pi R_r}{\eta}} \mathbf{a}_y , \quad (5.5)$$

where  $R_r$  (in  $\Omega$ ) is the receiving antenna radiation resistance.

Substituting (5.3) and (5.5) into (5.4) yields

$$V_{oc} = \frac{j}{k} \sqrt{2R_r P_t} \left[ \frac{e^{-jkL_{dir}}}{L_{dir}} F_{dir}(\phi, \theta) + \frac{e^{-jkL_{ref}}}{L_{ref}} F_{ref}(\phi, \theta) \right] . \quad (5.6)$$

The received power,  $P_r$ , defined by [59, p. 61] is described as

$$P_r = \frac{|V_{oc}|^2}{8R} , \quad (5.7)$$

where  $R = R_r$  for maximum power transfer.

The *path gain* (in dB) is obtained by substituting (5.6) into (5.7)

$$\frac{P_r}{P_t} = \frac{1}{4k^2} \left| \frac{e^{-jkL_{dir}}}{L_{dir}} F_{dir}(\phi, \theta) + \frac{e^{-jkL_{ref}}}{L_{ref}} F_{ref}(\phi, \theta) \right|^2 . \quad (5.8)$$

As shown in Fig. 5.1,  $d$  denotes the separation distance between the transmit and receive antennas,  $h_t$  and  $h_r$  the transmitter and receiver heights, respectively. For the validation experiments,  $h_t = h_r$ , therefore, the length of the direct path is

$$L_{dir} = d . \quad (5.9)$$

Let  $h = h_t = h_r$ . Applying Pythagoras' Theorem, the length of the reflected path is

$$L_{ref} = \sqrt{4h^2 + d^2} . \quad (5.10)$$

An estimation of the path gain determined by (5.8) can be compared in experimental measurements obtained by the channel sounder.

### 5.3 Description of the Experimental Configuration

In section §4.3, it was noted that the transmit and receive pyramidal horn antennas are mounted onto vertical mounts which have got an open-ended waveguide aperture. The

half-power beamwidths of the horn antennas are  $26^\circ$  in the vertical plane [50], which are not expected to produce sufficient reflection, given the separation distance and antenna heights. In order to have a meaningful comparison with the estimation of the path gain obtained by (5.8), it is necessary to produce a reflection from the ground. Therefore, the open-ended waveguide is more suitable for the validation measurements, as opposed to the narrow-beam horn antennas. Thus, the expression for  $F(\phi, \theta)$  in (5.8) is the radiated field for an open-ended waveguide on a ground plane defined by [61, p. 290]

$$F_E(\theta) = \frac{\sin \left[ \frac{\beta b}{2} \sin \theta \right]}{\frac{\beta b}{2} \sin \theta} \quad \phi = 90^\circ, \quad (5.11)$$

where  $b = 1.88$  mm and is the height of the waveguide [62].

The position of the transmitter and receiver boards are fixed on an optical table which consists of arrays of mounting holes that enable exact alignment of the transmit and receive open-ended waveguides. The transmitter and receiver heights,  $h = 9.74$  cm, which is measured from the surface of the optical table to the centre of the open-ended waveguide aperture. Fig. 5.2 shows the experimental configuration.

The mounting holes on the optical table have a diameter and a depth of approximately 5 mm, which is on the order of the wavelength ( $\lambda = 5$  mm). Thus, these could potentially scatter the ground reflection component. For this reason, the surface between the transmit and receive antenna is fully covered with aluminium tape, such that a smooth surface is established. Furthermore, absorbers are placed in front of the wall to prevent potential reflections, as shown in Fig. 5.2.

The separation distance,  $d$ , between the transmitter and receiver is measured between the reference planes shown in Fig. 4.2 and Fig. 4.3. The maximum separation distance that can be considered is 600 mm, which corresponds to  $120\lambda$ , and is limited by the length of the USB cables used to communicate with the control boards. Additionally, a frequency sweep is performed with a 10 MHz frequency resolution from 59.5 GHz to 60.5 GHz. The post-

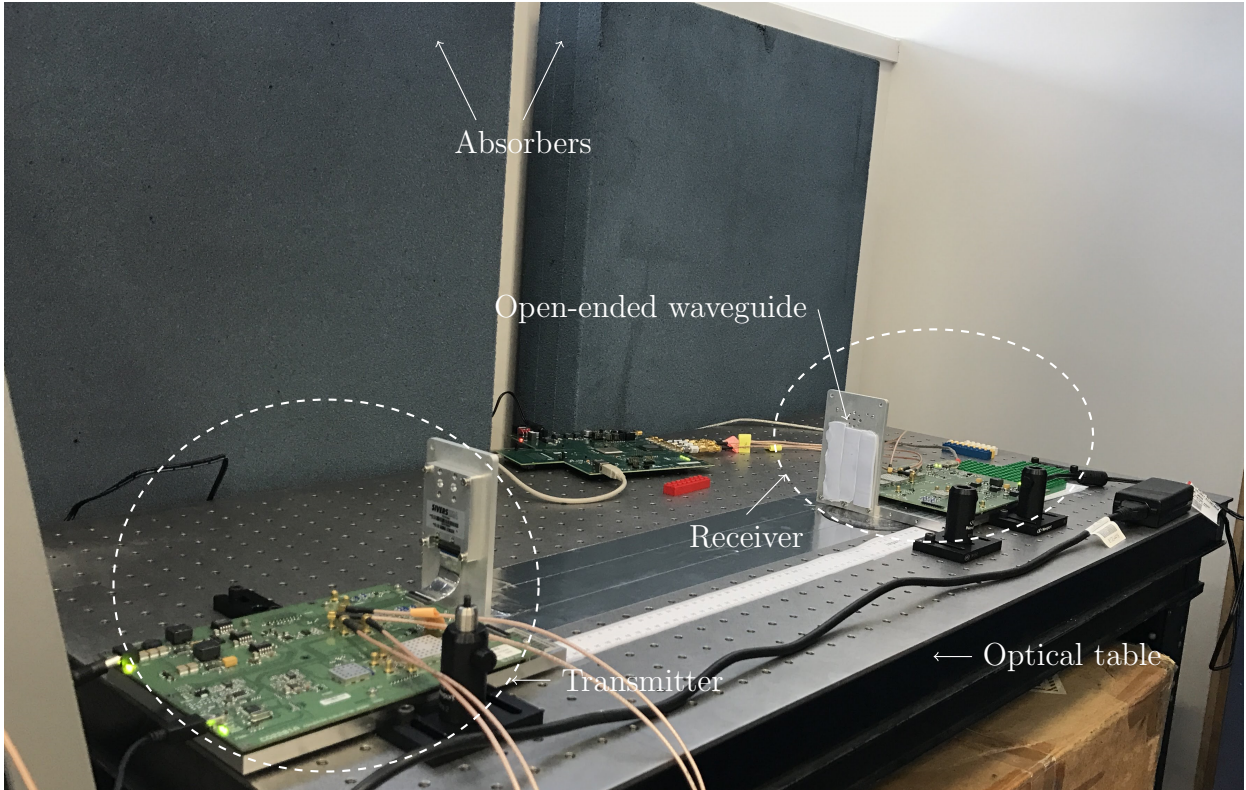


Fig. 5.2.: The transmit and receive open-ended waveguides are boresight aligned on the optical table.

processing of the received signal is performed using the methods described in section §4.7.

In Fig. 5.3 the received signal at  $d = 500$  mm is compared to the path gain estimate obtained by the two-ray model using (5.8). As discussed in section §4.7, the reduction in the signal strength around 60 GHz occurs due to the LO leakage. A significant disagreement between the measured signal and the path gain estimate is observed in Fig. 5.3. In particular, the path gain estimate displays a slow decrease in strength with increasing frequency. In contrast, the measured signal strength varies between  $-62.73$  dBm and  $-75.95$  dBm with four maxima and two minima across the channel bandwidth. These variations are the characteristics of constructive and destructive interference observed in the multipath phenomenon [63, p. 37].

The results shown in Fig. 5.3 suggest that the two-ray model is insufficient to report the propagation process. Section §5.4 describes how the channel model can be improved to describe the propagation process in the experimental configuration.

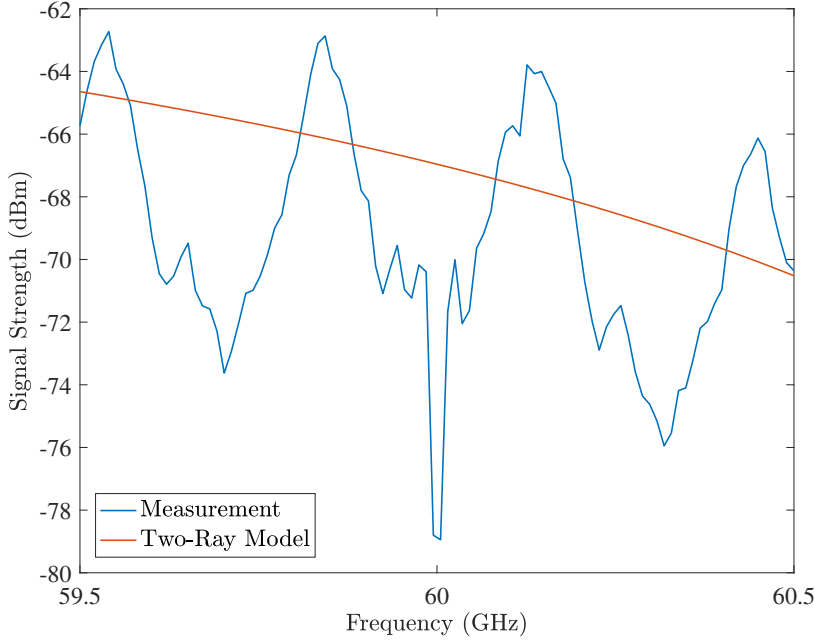


Fig. 5.3.: The received power (in dBm) as a function of frequency (in GHz) for the transmitter and receiver separated by  $d = 500$  mm on the optical table. The measured signal is compared to the path gain estimate obtained by the two-ray model.

#### 5.4 Extension to the Three-Ray Model

The fundamental assumption made for the two-ray model is that the received signal consists of two components: a direct ray and a reflected ray from the ground. However, the experimental configuration in Fig. 5.2 can also support a third ray which arises due to specular reflections from the vertical mounts. Fig. 5.4 illustrates how the third ray can be formed. Similar to the two-ray model, geometrical optics can be applied to model this additional ray. As these reflections from the vertical mounts occur on smooth surfaces, the angle of incidence at each reflection point equals the angle of reflection [64, p. 1014]. The dashed lines in Fig. 5.4 are extensions of the reflected ray back to a virtual receiver RX' at a distance  $d$  behind the real receiver RX. Similarly, a virtual image of the transmitter TX' can be located at a distance  $d$  behind the real transmitter TX. Therefore, the virtual image of the reflected ray appears to be formed between TX' and RX' and has the same geometry as the real reflected ray formed between TX and RX.

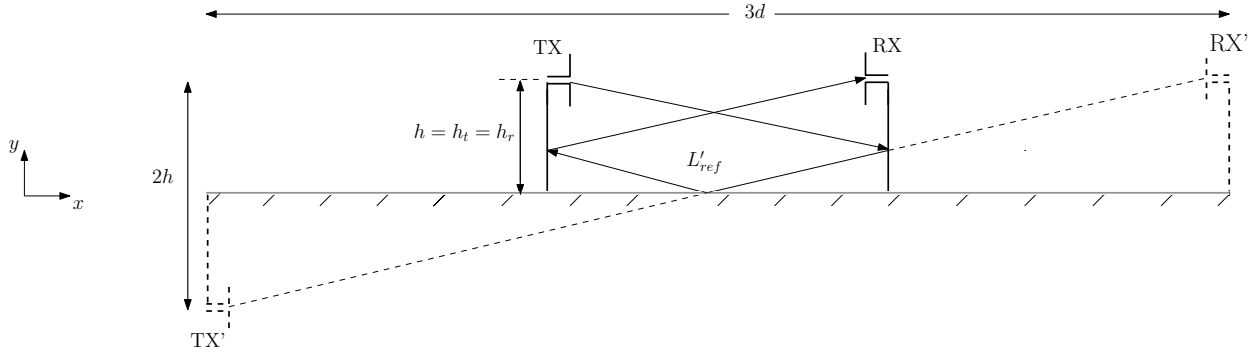


Fig. 5.4.: The third ray component arises due to specular reflections from the vertical mounts.

Similar to the derivation of the two-ray model described in section §5.2, the reflected field of the third ray is

$$\mathbf{E}'_{ref} = \rho j \frac{e^{-jkL_{ref\ 3ray}}}{L_{ref\ 3ray}} \sqrt{\frac{\eta P_t}{2\pi}} \mathbf{a}_y F'_{ref}(\phi, \theta), \quad (5.12)$$

where  $\rho = +1$ .  $F'_{ref}(\phi, \theta)$  in (5.12) denotes the angular-dependent pattern function of the open-ended waveguide given by (5.11).

The total electric field seen at the receiver consists of the direct ray, reflected ray from the ground reflection and the additional third ray. Therefore, the total electric field becomes

$$\mathbf{E}_{tot} = \mathbf{E}_{dir} + \mathbf{E}_{ref} + \mathbf{E}'_{ref}. \quad (5.13)$$

The received power can be obtained by substituting (5.13) into (5.6), and the resulting expression for  $V_{oc}$  into (5.7). The path gain (in dB) with the third ray component is given by

$$\frac{P_r}{P_t} = \frac{1}{4k^2} \left| \frac{e^{-jkL_{dir}}}{L_{dir}} F_{dir}(\phi, \theta) + \frac{e^{-jkL_{ref}}}{L_{ref}} F_{ref}(\phi, \theta) + \frac{e^{-jkL'_{ref}}}{L'_{ref}} F'_{ref}(\phi, \theta) \right|^2. \quad (5.14)$$

As shown in Fig. 5.4, the expression for the length of the third ray  $L'_{ref}$  can be found using Pythagoras' Theorem

$$L'_{ref} = \sqrt{(2h)^2 + (3d)^2}. \quad (5.15)$$

The measured signal shown in Fig. 5.3 can now be compared to the path gain estimate that is calculated using (5.14). Fig. 5.5(a) and (b) show the received power (in dBm) over the channel bandwidth compared to estimated distances of  $d = 500$  mm and  $d = 497.5$  mm,

respectively. In Fig. 5.5(a) the locations of the maxima and minima in the path gain estimate are aligned with those of the measured signal, when  $d$  in (5.15) is identical to the measured distance ( $d = 500$  mm). The root-mean-square deviation (RMSD) between the measured signal and the estimated path gain is 2.83 dBm. It should be noted that the data set between 59.98 GHz and 60.02 GHz corresponding to two frequency tones are excluded from the RMSD calculation.

On the other hand, Fig. 5.5(b) shows the comparison of the measured signal and the path gain estimate when  $d$  in (5.15) is changed to 497.5 mm. In this case, the magnitude of the first and third minima in the model have become more predominant. The RMSD between the measured signal and path gain estimate for  $d = 497.5$  mm is 1.98 dBm, suggesting that the three-ray model is more accurately representing the measured signal when the distance in the model is changed to 497.5 mm. The separation distance between the transmit and receive antennas was measured between the reference planes shown in Fig. 4.2 and Fig. 4.3. The disagreement between the measured and estimated distances can arise

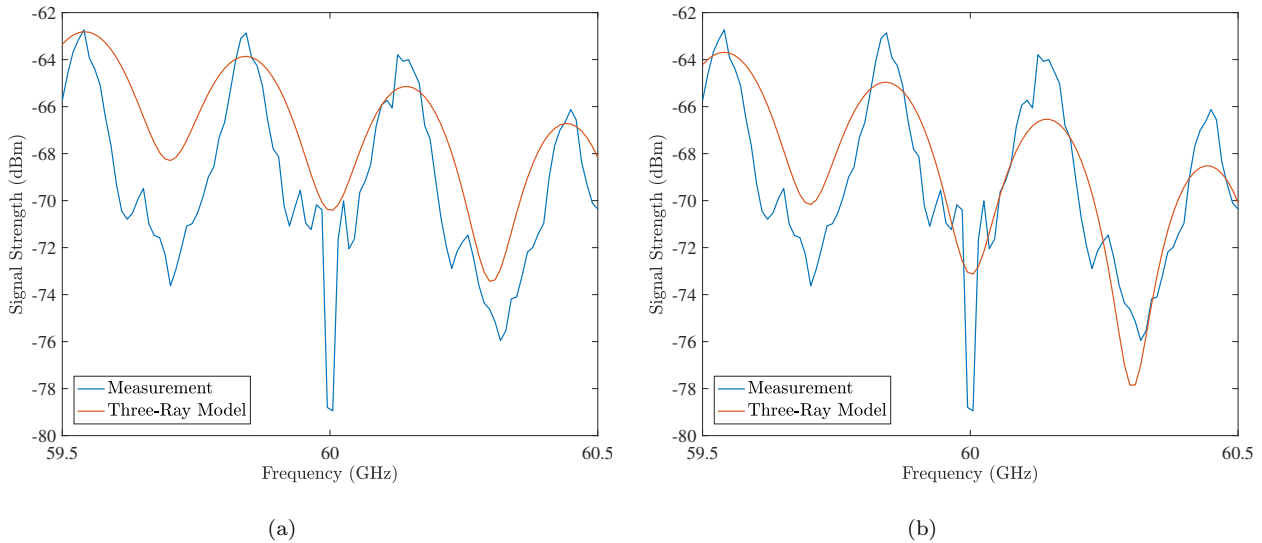


Fig. 5.5.: The received power (in dBm) as a function of frequency (in GHz) for the transmitter and receiver separated by  $d = 500$  mm on the optical table. The measured signal is compared to the path gain estimates obtained by the three-ray model, where the estimated distance is considered as (a)  $d = 500$  mm, and (b)  $d = 497.5$  mm.

from a misalignment of the phase centre in the aperture plane of the open-ended waveguide.

Furthermore, the experimental results in Fig. 5.5(a) and (b) demonstrate that millimetre wave propagation is very sensitive to small variations in the environment due to the small wavelength. Specifically, a 2.5 mm shift in the geometry of the environment corresponds to a half of the wavelength and therefore has an impact on the corresponding path gain estimate. In order to improve the path gain estimate using the three-ray model, the surface of the optical table is required to be perfectly smooth. That is, the imperfections introduced by covering the mounting holes with aluminium tape can potentially scatter the waves.

## 5.5 Free Space Measurement in the Anechoic Chamber

### 5.5.1 The Measurement Procedure

The available documentation for the up-converter is insufficient to precisely determine the output power from the power amplifier chain at the transmitter [48]. An indication of the transmitted power is necessary to evaluate the path loss in indoor environments.

Alternatively, the frequency response of the channel sounder can be measured in free space conditions to determine the transmit power from the free space path loss. In addition, the rotation of the receiver in the azimuth plane under free space conditions enables identification of the back lobe and side lobes of the transmit and receive antennas. Therefore, a measurement using the channel sounder is conducted in an anechoic chamber.

The channel sounder configuration is shown in Fig. 4.1. In particular, the transmitter and receiver pyramidal horn antennas [50] that will be used for the indoor measurements are mounted onto the vertical mounts, as shown in Fig. 4.2 and Fig. 4.3, respectively. Additionally, the receiver is installed on the rotator to perform an angular sweep in the azimuth plane, as shown in Fig. 4.3. The transmit and receive antennas are separated by 2 m, which is measured between the reference planes depicted in Fig. 4.2 and Fig. 4.3. The transmit and receive antennas are boresight aligned and elevated 1.2 m from the ground. Specifically,

the vertical and horizontal alignments of the transmit and receive antennas are verified with an alignment laser.

A frequency sweep from 59.5 GHz to 60.5 GHz with 20 MHz frequency resolution is performed. The receiver is rotated from  $0^\circ$  to  $360^\circ$  in  $10^\circ$  angular steps. The receiver measures the transmitted complex tone of a fixed frequency,  $f$ , during one full rotation. Once the rotation is complete, a complex tone at the next frequency step is generated and transmitted, which again is captured by the receiver during the following rotation. At the completion of the frequency sweep along the entire bandwidth, a total number of 50 frequency tones are captured at each angular position. The frequency response received at an angular position is averaged to obtain the mean received power. The mean received power as a function of angle,  $\bar{P}_r(\theta)$ , (in Watts) at an angular position,  $\theta$ , is given by

$$\bar{P}_r(\theta) = \frac{1}{N} \sum_f \frac{|V_f/V_o|^2}{R} \quad \theta = 0^\circ : 360^\circ, \quad (5.16)$$

where  $V_f$  (in Volts) is the voltage of the received complex frequency tone,  $N$  is the total number of tones in the frequency sweep (and is equal to 50), and  $R = 50 \Omega$ .  $V_o$  in (5.16) denotes the reference voltage received in the boresight angle and is used to normalise the received voltage.

Fig. 5.6 shows the polar plot of the frequency-averaged received power (in dBm) measured with a  $10^\circ$  angular resolution. The received power is calculated using (5.16), where  $V_o = 34$  mV and is the average received voltage at  $0^\circ$ . As shown in Fig. 5.6, the maximum power is received at  $0^\circ$  when the transmit and receive antennas are boresight aligned. The 3-dB beamwidth is  $24^\circ$ , and the two side lobes are approximately 23 dB below the maximum received power at  $0^\circ$ , located at  $50^\circ$  and  $310^\circ$ .

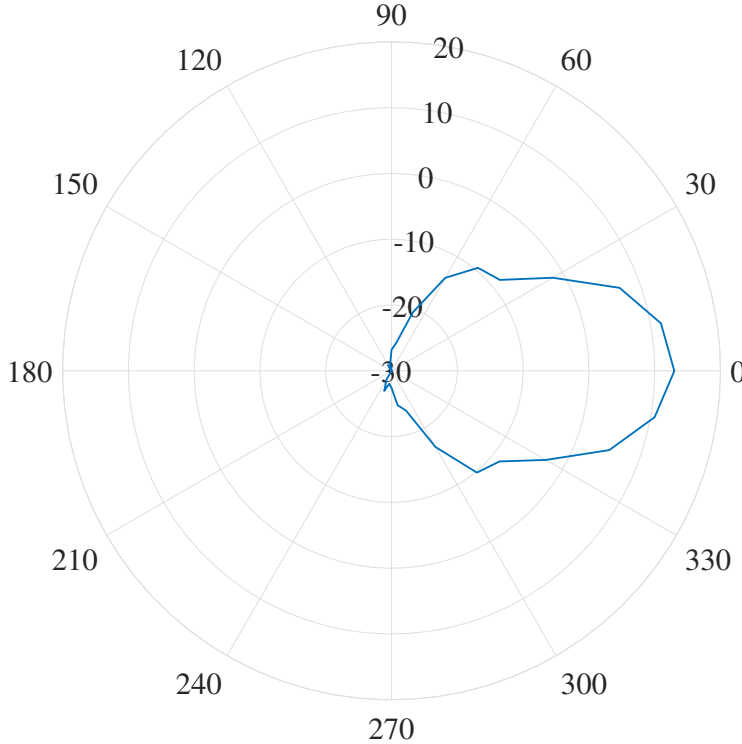


Fig. 5.6.: The polar plot of the frequency-averaged received power (in dBm) measured with a  $10^\circ$  angular resolution in the anechoic chamber.

### 5.5.2 Link Budget Analysis

The received power  $P_r$  (in dBm) at the receiver is given by

$$P_r = P_t + G_t - \text{PL} + G_r , \quad (5.17)$$

where PL is the measured path loss (in dB),  $P_t$  is the transmitted power (in dBm), and  $G_t$  and  $G_r$  (in dBi) are the transmit and receive antenna gains, respectively. In this case, PL is the free-space path loss,  $G_t = G_r = 17$  dBi [50], and  $P_r$  is the received power when transmit and receive antennas are boresight aligned and is equal to  $-16.4$  dBm ( $P = V_o^2/R$ , where  $V_o = 34$  mV and  $R = 50 \Omega$ ).

Free-space path loss (in dB) between the transmitter and receiver, assuming isotropic antennas, is

$$\text{PL}_{\text{FS}} = -10 \log_{10} \left( \frac{\lambda}{4\pi d} \right)^2 \quad (5.18)$$

where  $\lambda$  is the wavelength, and  $d$  is the separation distance between the transmit and receive antennas (and is equal to 2 m). Substituting  $\lambda = 5$  mm at 60 GHz, and  $d = 2$  m into (5.18) results with  $PL_{FS} = 74.1$  dB. Thus, solving for  $P_t$  using (5.17) yields 23.7 dBm.

## 5.6 Summary

In this chapter, measurements using the channel sounder were compared to two-ray and three-ray channel models. In the first case, the path gain estimate obtained from the two-ray model was observed to agree well with the measured signal from the channel sounder, when an additional ray component corresponding to a higher order reflection from the vertical mounts was taken into consideration. Additionally, the results demonstrate that millimetre wave propagation is very sensitive to small-scale variations (on the order of the wavelength) in the environment.

In the second case, the channel sounder was taken to an anechoic chamber to calculate the transmit power using free-space path loss measurements. The transmit power can be used to determine the path loss for the office measurements that will be discussed in Chapter 6. Thus far, the signal response from the channel sounder has been observed in a laboratory environment under simplified propagation conditions. Chapter 6 involves investigation of the millimetre wave propagation in a confined office environment that contains varying levels of environmental clutter.

## 6. OFFICE MEASUREMENTS WITH THE CHANNEL SOUNDER

### 6.1 Introduction

Following the description of the system architecture in Chapter 4, the performance of the channel sounder has been validated in Chapter 5. As noted in Section §3.2, previous research for indoor millimetre wave propagation has largely focused on hallways [34], [28], portions of a building floor [65], [35], and open-plan office environments [40]. Confined offices represent an important deployment case as these are a typical feature of most office buildings throughout the world. However, indoor propagation in confined offices has not been investigated in detail. Therefore, the primary aim of the indoor measurements reported in this chapter is to undertake a preliminary investigation in a confined office environment.

An overview of the three measurement phases is provided in section §6.2, where the strategy and investigation objectives of each phase are briefly described. The measurement environment is also described in section §6.2. Section §6.3 describes the measurement procedure including the impact of the frequency sweep resolution on the analysis of the received channel information. The channel measurements are organised as follows: section §6.4 (Phase A) focuses on multipath propagation in a confined office environment; section §6.5 (Phase B) focuses on the potential impact of the human body on the propagation of millimetre waves; and section §6.6 (Phase C) considers measurements between two adjacent offices. The main findings from the indoor measurements reported in this chapter are briefly summarised in section §6.7.

### 6.2 An Overview of the Measurement Phases

The measurement environment consists of two adjacent offices, office 1 and office 2. The dimensions of offices 1 and 2 are similar with width ( $W$ ) = 2.98 m, length ( $L$ ) = 3.75 m and

height ( $H$ ) = 3 m<sup>1</sup>. Both offices contain varying levels of environmental clutter, including desks, tables, filing cabinets, bookshelves, and whiteboards. The partition between the two offices consists of drywall on timber stud framing. Additionally, the offices are separated from the corridor with a frosted glass window surrounded by metal frames. Fig. 6.1 shows a photo of office 1<sup>2</sup>.

The channel measurements in this chapter are performed with the channel sounder described in section §4.3, where pyramidal horn antennas [50] are used both for the transmitter and receiver. For each measurement, it should be noted that the transmitter is fixed at a particular orientation and only the receiver is rotated in the azimuth plane. Additionally, the transmit power is 23.7 dBm, which is obtained from the free-space measurement described in section 5.5, and remained constant for all measurements presented in this chapter.

Measurement Phase	Measurement Scenario	Measurement Description	Investigation Objective
Phase A	LOS/NLOS	The transmitter is left static in office 1, five LOS receiver locations and one NLOS receiver location in the corridor are considered.	Analyse the propagation of millimetre waves in a confined office environment and the multipath propagation.
Phase B	NLOS	The receiver path is blocked with absorbers.	Investigate the impact of the human body blockage.
Phase C	NLOS	The transmitter is moved to office 2, while the receiver remains in office 1.	Examine the inter-office propagation.

Table 6.1.: An overview of the measurement phases and their investigation objectives.

Table 6.1 summarises the measurement phases with a description of the experiment and the investigation objectives. In Phase A, the transmitter is located within office 1, and five LOS receiver locations within the office are considered. Then, the receiver is moved to the corridor for a single NLOS measurement. The aim in Phase A is to analyse the propagation of millimetre waves in a confined office environment. Additionally, Phase A enables analysis of the impact of the varying levels of environmental clutter on the multipath propagation channel.

<sup>1</sup>These offices are located in the Electrical and Computer Engineering building (extensively renovated in 2014) at the Newmarket Campus of the University of Auckland.

<sup>2</sup>Office 2 contains similar office furniture, with the exception of the table and additional bookshelf.



Fig. 6.1.: A photo of office 1 with the measurement coordinates (receiver is parallel to the door when rotated to  $0^\circ$ ). Annotations show the transmitter, the receiver positioned on the table (in LOC 1), signal generators and the oscilloscope.

In Phase B, the impact of body blockage on millimetre wave propagation is investigated. This measurement is performed in office 1 where the LOS path between the receiver and the transmitter is blocked with absorbers in order to emulate obstruction by a human body.

Phase C involves measurements between office 1 and office 2. The transmitter location and orientation are varied in office 2 and the receiver remains in office 1. The measurement results from Phase C enables investigation of propagation mechanisms in NLOS scenarios, and comparisons with the results from Phase A provides an insight into the interference challenges that may be encountered for millimetre wave system deployments in confined office environments.

### 6.3 The Measurement Procedure

The three phases described in section §6.2 consider various transmitter and receiver locations. A frequency sweep from 59.5 GHz to 60.5 GHz is performed at each receiver location. Additionally, an angular sweep is performed by rotating the receiver in the azimuth

plane from  $0^\circ$  to  $360^\circ$  in  $10^\circ$  angular steps, while the orientation of the transmit antenna remains fixed. In order to account for multipath in the propagation environment, the channel frequency response for each angular position is averaged to obtain the mean received power as a function of angle. The mean received power as a function of angle,  $\bar{P}_r(\theta)$ , (in Watts) is given by (5.16) and is repeated here for convenience

$$\bar{P}_r(\theta) = \frac{1}{N} \sum_f \frac{|V_f/V_o|^2}{R} \quad \theta = 0^\circ : 360^\circ , \quad (6.1)$$

where  $V_f$  (in Volts) is the voltage of the received frequency tone,  $N$  is the total number of tones in the frequency sweep, and  $R = 50\Omega$ . The received voltage is normalised by  $V_o$  which is the reference voltage obtained from the free-space measurement described in section §5.5 (and is equal to 34 mV).

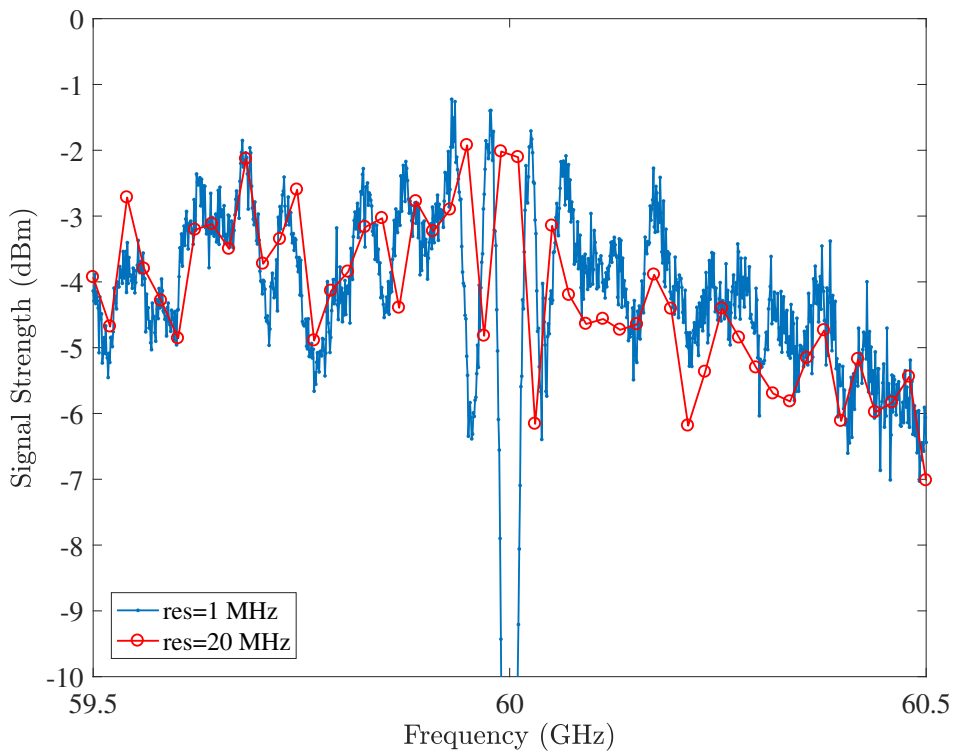


Fig. 6.2.: Signal strength (dBm) as a function of frequency (GHz). Comparison of two frequency sweep measurements performed with frequency resolutions of 1 MHz and 20 MHz.

The measurement time is proportional to the resolution of the angular and frequency sweeps. An angular resolution of  $10^\circ$  was found to provide an appropriate trade-off between capturing the channel characteristics in the azimuth plane and the measurement time. In order to investigate the impact of the frequency resolution a fine frequency sweep with 1 MHz frequency resolution ( $N = 1000$ ) is compared to a coarse frequency sweep with 20 MHz ( $N = 50$ ). During these measurements, the transmit and receive antennas were boresight aligned, approximately 3 m apart, and located in office 1 and office 2, respectively. In order to provide a meaningful comparison, the transmitter and receiver locations remained unchanged between each measurement set. Fig. 6.2 shows the comparison of these two frequency sweep measurements. The reduction in signal strength around 60 GHz occurs due to the LO leakage, as described in section §4.7.

In Fig. 6.2, it is observed that the frequency sweep with 1 MHz resolution captures the fine variations in the channel. However, the measurement time is approximately 2 hours for this frequency sweep. The average received power calculated using (6.1) is  $P_r = -3.94$  dBm, where the data set between 59.98 GHz and 60.02 GHz corresponding to 39 frequency tones are excluded from the  $P_r$  calculation, as these values surround the suppressed DC tone. In comparison, the coarse frequency sweep at 20 MHz resolution takes approximately 7.5 minutes. While the fine variations in the channel are not captured, the average received power for the coarse resolution is  $P_r = -4.08$  dBm. The difference in the average power between the fine and coarse frequency sweeps is 0.14 dB. This result indicates that the variation between the two frequency sweeps is small in comparison to the expected angular differences. Therefore, the coarse resolution at 20 MHz is appropriate to fulfil the requirement to remove the multipath effects. The indoor channel measurements reported in this chapter are performed with a 20 MHz frequency resolution.

## 6.4 Phase A: In-Office Measurements

### 6.4.1 Transmitter and Receiver Parameters

Fig. 6.1 shows a photo of the main office with the transmitter elevated 149.5 cm above the ground (measured from the centre of the antenna aperture). When the receiver is orientated at  $0^\circ$ , it is parallel to the frosted glass window and the corridor. The azimuth of the transmit antenna is set to  $135^\circ$  and a mechanical downtilt of approximately  $4^\circ$  is applied to prevent overshoot of the receive antenna. The transmitter location and parameters are selected to emulate a typical deployment of a millimetre wave access point. Alternative transmitter configurations are also considered in Appendices A and B. The signal generators and the oscilloscope are placed on a trolley, as shown in Fig. 6.1. The vertical clearance between the transmit antenna and the equipment trolley is approximately 0.3 m. In order to confirm whether this clearance is sufficient, the first Fresnel zone is computed. The radius of the  $n$ th Fresnel zone from the direct path is given by [19, p. 36]

$$r_n = \sqrt{\frac{n\lambda d_1 d_2}{d_1 + d_2}}, \quad (6.2)$$

where  $n = 1$  for the first Fresnel zone,  $d_1$  and  $d_2$  are the distances between the obstacle and receiver, and the obstacle and transmitter, respectively. In the configuration shown in Fig. 6.1,  $d_1 = 0.5$  m,  $d_2 = 2.2$  m, and the first Fresnel zone calculated using (6.2) at the location of the trolley is 0.045 m. As  $r$  is significantly less than the 0.3 m vertical clearance, the LOS path between the transmit and receive antenna in Fig. 6.1 is free of obstructions.

Fig. 6.3 shows a floor plan of offices 1 and 2 with all the receiver locations identified. It should be noted that the dimensions and positions of the objects shown in Fig 6.3 were accurately measured and correspond to the actual office clutter in the measurement environment. Additionally, the location of the timber framing studs within the drywall were identified using a stud finder device. The corresponding heights of the receiver,  $h_r$  are provided in Table 6.2. At LOC 1, the receiver is positioned on the table, as depicted in Fig. 6.1, and  $h_r = 95.7$  cm. At LOC 2, it is positioned on the desk, and  $h_r = 100.7$  cm, and placed in the corner of the room at LOC 3. For the remaining receiver locations, LOC 4 to 8, the receiver is positioned on a trolley for ease of transport, and  $h_r = 102.9$  cm. At LOC 4, the

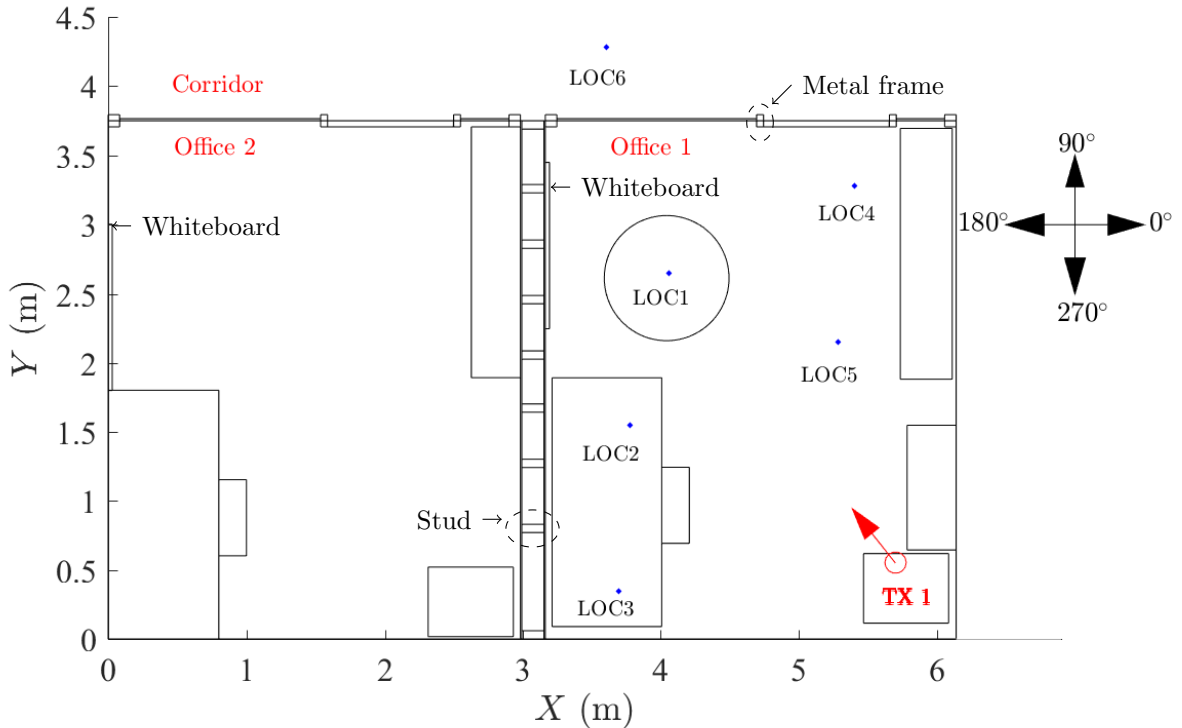


Fig. 6.3.: The floor plan of the measurement environment with the receiver locations. The partition between office 1 and office 2 is a drywall with timber stud framing. Frosted glass window with metal framing is separating each office from the corridor. The receiver is parallel to the corridor when it is orientated to  $0^\circ$ .

Measurement Scenario	Receiver Location	Receiver Location Description	$h_r$ (cm)
LOS	LOC 1	Table	95.7
	LOC 2, 3	Office desk	100.7
	LOC 4, 5	Adjacent to the bookshelf	102.9
NLOS	LOC 6	Corridor	102.9

Table 6.2.: Receiver locations and receiver heights for Phase A.

receiver is adjacent to the bookshelf and in front of the door, and at LOC 5, it is moved physically closer to the transmitter and towards the centre of the office. At LOC 6, the receiver is positioned in the corridor.

#### 6.4.2 LOS Measurement Results

Fig. 6.4(a) and (b) show the frequency-averaged received power (in dBm) measured with a  $10^\circ$  angular resolution in the azimuth plane at LOC 1 and LOC 2, respectively. As described in section §6.3, the frequency average is performed using (6.1) with  $N = 50$  corresponding to a 20 MHz resolution frequency sweep. Fig. 6.4(a) shows two multipath components with power above  $-10$  dBm observed at LOC 1: the strongest component is measured at  $310^\circ$  with  $P_r = 7.6$  dBm which represents the LOS path, and the second strongest component is received at  $130^\circ$  with  $P_r = -6.3$  dBm.

Similarly, in Fig. 6.4(b), the strongest component at LOC 2 is received at  $330^\circ$  with  $P_r = 0.1$  dBm which represents the LOS path, while the second strongest component is observed at  $120^\circ$  with  $P_r = -5.2$  dBm. Although the receiver gained 5 cm elevation and 0.5 m proximity to the transmitter when moved to LOC 2, as a consequence of the  $20^\circ$  misalignment between the boresights for the transmitting and receiving antennas, the power measured for the LOS component is reduced by 7.5 dB.

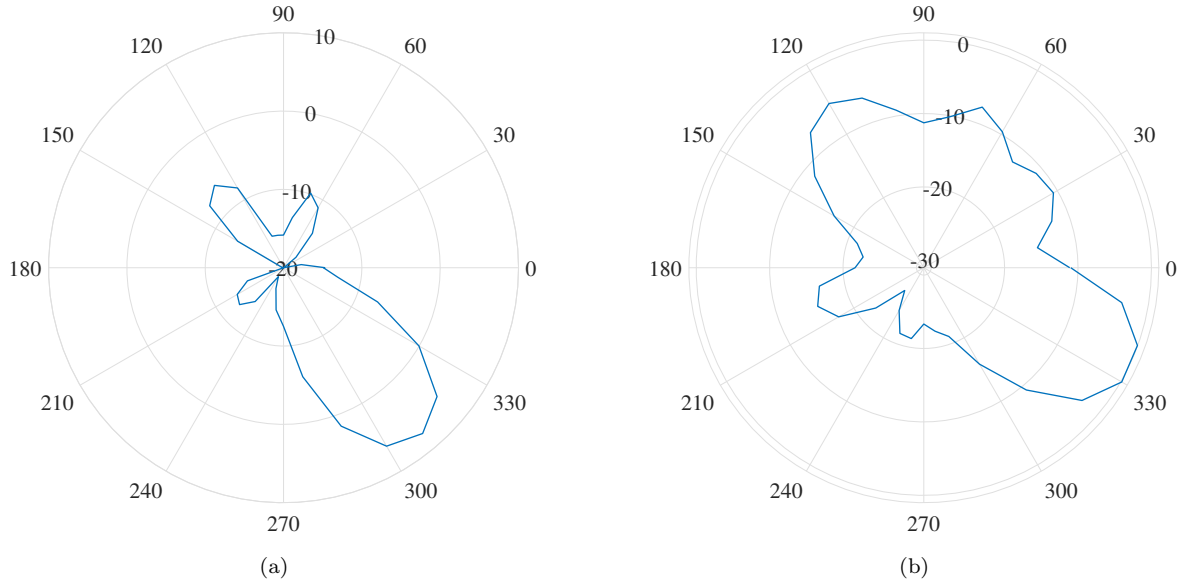


Fig. 6.4.: The polar plots show the frequency-averaged received power (dBm) at (a) LOC 1, and (b) LOC 2.

The results from the free-space measurements in section 5.5 showed the pyramidal horn antenna does not have a distinct back lobe. Therefore, the second strongest component received in Fig. 6.4(a) at  $130^\circ$  for LOC 1, and in Fig. 6.4(b) at  $120^\circ$  for LOC 2, are likely to arise from reflections or scattering in the environment. The positions of the transmitter, receiver and objects in the environment are accurately measured. The polar plot of the received power (in linear units) can be superimposed on the floor plan, thus allowing rays based on laws of geometrical optics to be manually drawn. As shown in Fig. 6.5, the source and direction of each multipath component can be estimated, such that angle of reflection at each point is equal to the angle of incidence. From this analysis, the second strongest component in Fig. 6.4(b) at  $120^\circ$  can be shown to result from a second-order reflection. Specifically, the first reflection occurs at the frosted glass window, where the second reflection occurs from the whiteboard. Additionally, Fig. 6.5 shows that the multipath component received at  $70^\circ$  could be caused by a first-order reflection. As the reflection point is at the edge of the metal door frame, it is difficult to conclude this is a specular reflection caused by the metal door frame. In particular, the received power is 2.5 dB lower than the second-order reflection suggesting this wave component may be scattered. The multipath component at  $70^\circ$  in Fig. 6.4(b) is further investigated in Appendix C.

Fig. 6.6(a) shows a polar of the frequency-averaged received power (in dBm) measured at LOC 5 with a  $10^\circ$  angular resolution. At this location, two strong components are observed with received powers of  $-3.3$  dBm and  $-2.3$  dBm at  $280^\circ$  and  $140^\circ$ , respectively. The multipath component at  $280^\circ$  arises from the LOS path. The component at  $140^\circ$  is observed to point away from the transmitting antenna. Similar to Fig. 6.5, rays can be manually drawn to estimate the source and direction of the multipath component for LOC 5. As shown in Fig. 6.6(b) the transmitted wave can be shown to firstly reflect from the whiteboard, and from the whiteboard to the frosted glass window before propagating to the receiver. It is interesting to note that the second-order reflection component at  $140^\circ$  has approximately the same strength as the LOS component.

Additionally, comparing the polar plots of Fig. 6.4(a) and Fig. 6.6(a) shows the received power on the LOS path has reduced by 10.9 dB in Fig. 6.6(a), when the receiver is posi-

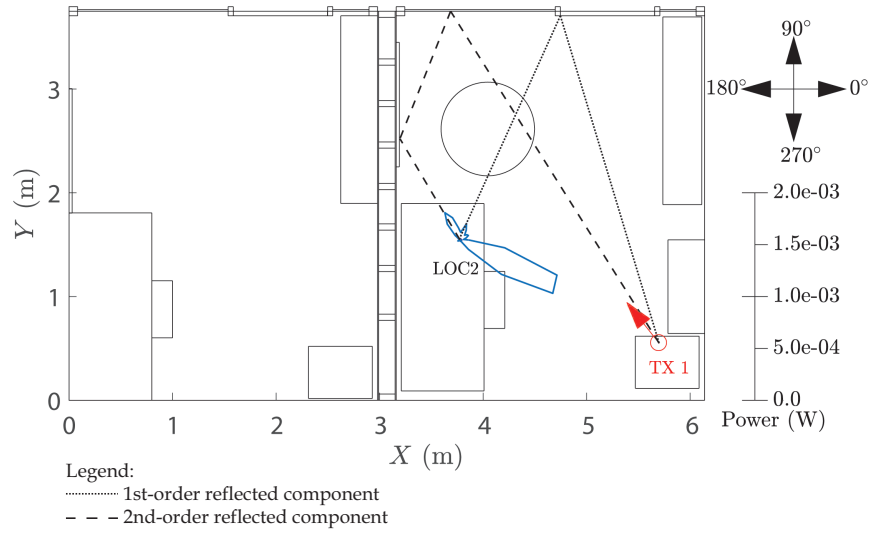


Fig. 6.5.: Manually drawn rays on the office floor plan showing how the second-order reflection (from the whiteboard and the frosted glass window) gives rise to the multipath component at LOC 2. Also shown is the first-order reflected component from the edge of the metal door frame.

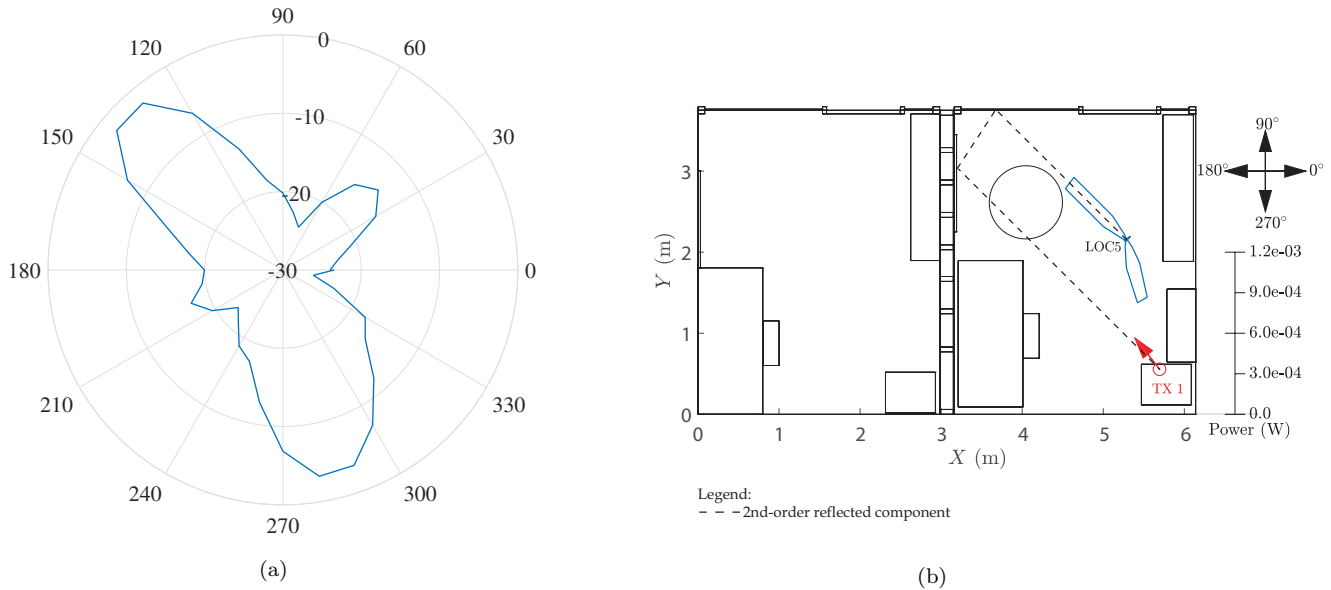


Fig. 6.6.: (a) The polar plot of the frequency-averaged received power (in dBm) at LOC 5, and (b) manually drawn rays for LOC 5 show a second-order reflection (from the whiteboard and frosted glass window) giving rise to the strongest multipath component.

tioned at LOC 5. The  $30^\circ$  misalignment between the boresights of the transmit and receive antennas could be the main contributor to the power reduction in the LOS path.

Fig. 6.7(a) and (b) show the polar plots of the frequency-averaged received power (in dBm) at LOC 4 and LOC 3, respectively. Both receiver locations are positioned in the corners of office 1. In Fig. 6.7(a), the three strongest multipath components at LOC 4 are the following: the strongest multipath component occurs at  $150^\circ$  with  $P_r = -3.6$  dBm, the second strongest component is observed at  $270^\circ$  with  $P_r = -13.14$  dBm, and the third component occurs at  $200^\circ$  with  $P_r = -12.35$  dBm. The component received at  $270^\circ$  represents the LOS path, and the remaining two components arise when the receiver is faced away from the transmitter. The manually performed ray analysis in Fig. 6.8 shows that a second-order reflection from the metal door frame and the whiteboard give rise to the component at  $150^\circ$ . Interestingly, the received power caused by the second-order reflection is 9.5 dB higher than the LOS component.

In contrast, as shown in Fig. 6.7(b), the received power levels are below  $-10$  dBm for all azimuth angles at LOC 3. The received power in the estimated LOS path at  $0^\circ$  is

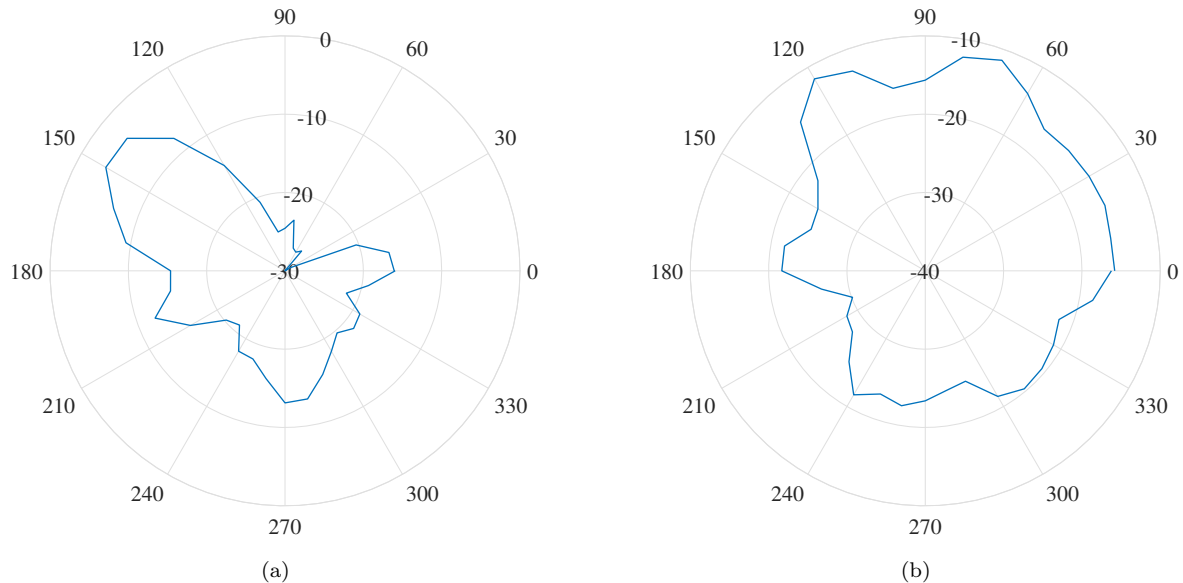


Fig. 6.7.: The polar plots show the frequency-averaged received power (in dBm) at (a) LOC 4, and (b) LOC 3.

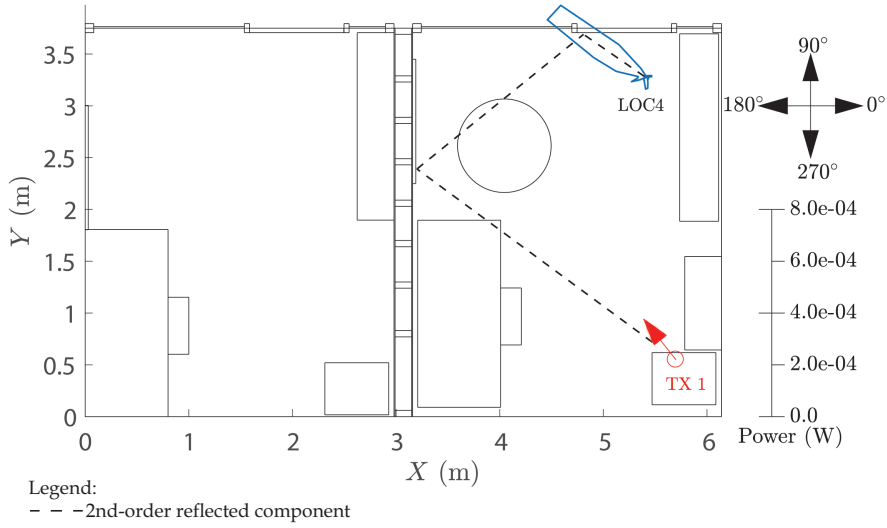


Fig. 6.8.: Manually drawn rays on the office floor plan showing how the second-order reflection (from the whiteboard and metal door frame) give rise to the strongest multipath component received at LOC 4.

$-16.2$  dBm, which is the lowest received power compared to all Phase A LOS measurements. It is noted that the misalignment in the boresights between transmit and receive antennas is greater than  $40^\circ$  for this receiver location, suggesting that this could be the main contributing factor to the weak power levels. Additionally, no dominant multipath components are observed in Fig. 6.7(b) suggesting that LOC 3 does not support strong first- and second-order reflections from the environment.

#### 6.4.3 Corridor Measurement Result

When the receiver is positioned in the corridor at LOC 6 outside office 1, two strong multipath components are observed, as shown in Fig. 6.9(a): the strongest component is observed at  $300^\circ$  with  $P_r = -2.6$  dBm, which represents the direct path, and the second

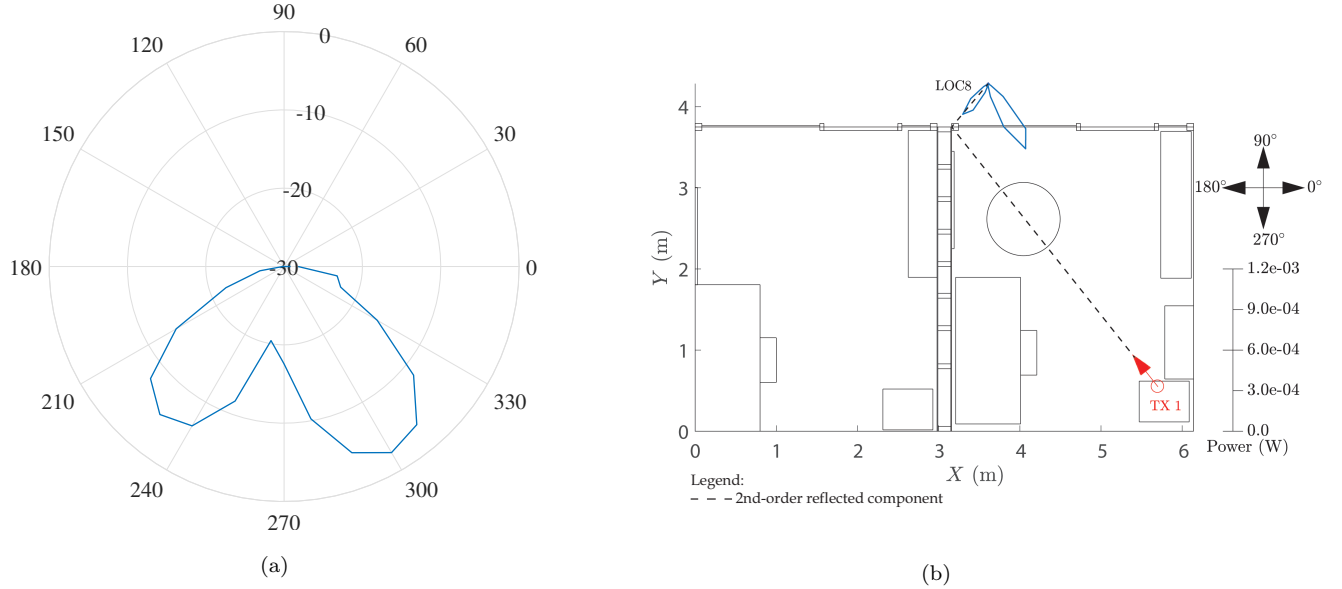


Fig. 6.9.: (a) The polar plot of the frequency-averaged received power (in dBm) at LOC 6, and (b) manually performed ray analysis for LOC 6 shows a first-order reflection near the metal frame.

component is approximately 3 dB weaker at  $230^\circ$  ( $P_r = -5.3$  dBm). Fig. 6.9(b) indicates that the second component could result from a first-order reflection. However, the specular reflection surface is uncertain as the reflection point is close to the metal frame next to the wall<sup>3</sup>. By comparing the received power on the LOS path between Fig. 6.4(a) and Fig. 6.9(a), an estimate of the attenuation experienced when penetrating through the glass can be obtained. In this case, the attenuation is approximately 10.2 dB, however it should be noted that this also includes reflection.

#### 6.4.4 Path Loss Analysis

The path loss (PL) between the transmitter and receiver is given by rearranging (5.17)

$$\text{PL(dB)} = P_t + G_t + G_r - P_r , \quad (6.3)$$

<sup>3</sup>Videos from a site visit during renovation in 2013 indicate a metal pole with circular edges located inside the drywall. It is possible this internal metal pole may be contributing (or responsible) for the reflected component.

Measurement Scenario	Receiver Location	Distance (m)	$P_r$ (dBm)	Path Loss (dB)	$\Delta\theta$ (°)
<b>LOS</b>	LOC 1	2.7	7.6	50.0	0
	LOC 2	2.2	0.1	57.5	24.7
	LOC 3 <sup>4</sup>	2.0	-16.2	73.9	46.2
	LOC 4	2.7	-13.1	70.8	31.8
	LOC 5	1.7	-3.3	60.9	23.4
<b>NLOS</b>	LOC 6	4.3	-2.6	60.2	8.6

Table 6.3.: Summary of Phase A in-office measurement results.

where  $G_t = G_r = 17$  dBi at 60 GHz [50], and  $P_t = 23.7$  dBm (obtained from the free-space measurement in the anechoic chamber in section 5.5).

Table 6.3 summarises the measurement results for Phase A: the path loss is calculated using (6.3), and  $P_r$  (in dBm) is the received power of the LOS (direct) component at each receiver location discussed in sections 6.4.2 and 6.4.3. The distance denotes the separation distance between the transmit and receive antennas and is calculated using Pythagoras Theorem. Also provided in Table 6.3 is the misalignment between the boresights of the transmit and receive antennas,  $\Delta\theta$  (in degrees), at each receiver location calculated relative to LOC 1 using trigonometry. Specifically, the angle between the LOS component and the transmit antenna is calculated for a particular receiver location, which is then subtracted from the angle between the LOS component at LOC 1 and the transmit antenna.

Comparing the path loss values for the LOS scenarios in Table 6.3, the highest path loss is observed at LOC 3 (when  $\Delta\theta = 46.2^\circ$ ). In contrast, the lowest path loss is observed at LOC 1, when the receiver antenna is in the boresight of the transmit antenna ( $\Delta\theta = 0^\circ$ ). Interestingly, LOC 1 and LOC 4 are the same distance from the transmitter, the path loss at LOC 4 is 20.8 dB higher compared to LOC 1. This observation can be explained by noting that at LOC 4 the boresight misalignment between the transmit and receive antennas is

---

<sup>4</sup>Although, Fig. 6.7(b) did not provide a clear indication of the LOS path, for the path loss analysis the LOS path is estimated to occur at  $0^\circ$ .

$31.8^\circ$ .

At LOC 5 the receiver is in proximity to the receiver, however, the path loss, in this case, is increased by 10.9 dB compared to LOC 1. Also, the difference between the path loss values for LOC 5 and LOC 2 is 3.4 dB. In particular,  $\Delta\theta$  for LOC 5 and LOC 2 are very similar which suggests that reflections from the environment could be contributing to the LOS component at LOC 2 resulting with a lower path loss.

When the receiver is at LOC 6, the separation distance is approximately twice compared to most of the LOS receiver locations. Although the transmitter and receiver are separated by the frosted glass window, in this case, the path loss is lower compared to LOC 3 and LOC 4 due to the improved alignment of the transmit and receive antennas ( $\Delta\theta = 8.6^\circ$ ).

The path loss is observed to increase with greater misalignment between the boresights of transmitting and receiving antennas. While the variation in distances at receiver locations is less than 1 m for most LOS scenarios, the difference between the maximum and minimum path loss is found to be 23.9 dB in the confined office environment, indicating the impact of beam misalignment for directional antennas.

## 6.5 Phase B: Impact of the Human Body

User equipment are commonly used in close proximity to the human body, i.e. hand-held devices. In such cases, the propagation channel is influenced by the user. However, at millimetre wave frequencies diffraction cannot be relied upon to bend energy around the human body (as described in section 2.3). Therefore, it is essential to investigate the potential impact of the blockage of the LOS path (by a phantom) on the millimetre wave propagation in a confined office environment.

As depicted in Fig. 6.10, the blockage of the LOS path by a human body was emulated by placing absorbers with dimensions of  $L = 60$  cm,  $W = 22.4$  cm and  $H = 71$  cm on an office chair elevated 56 cm from the ground. The transmitter and receiver parameters

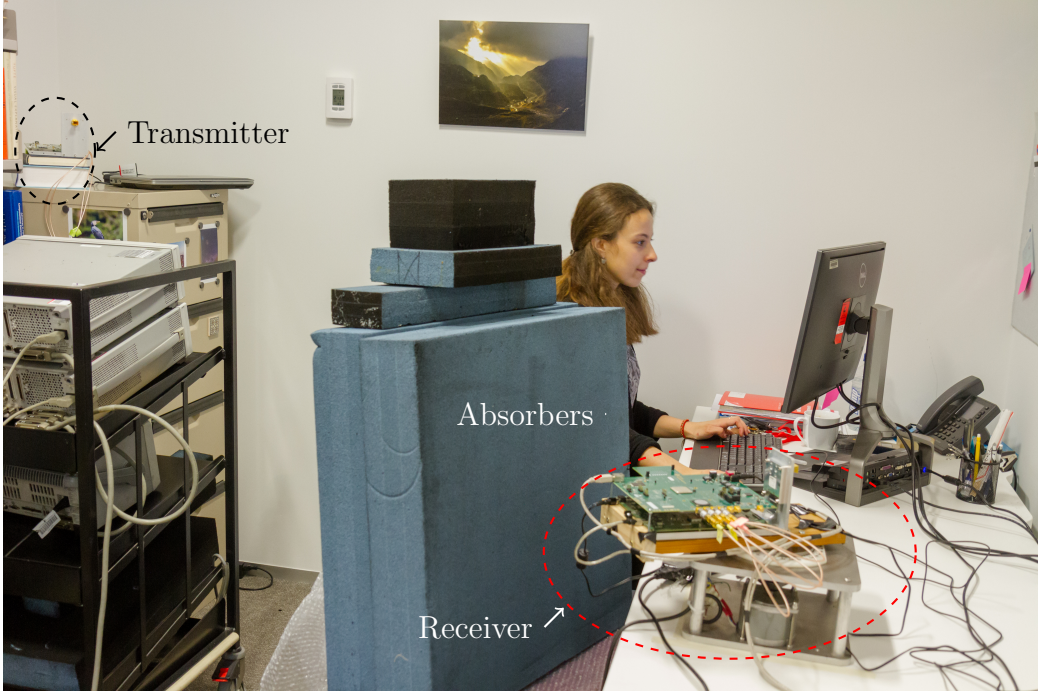


Fig. 6.10.: The measurement configuration with the absorbers placed on an office chair such that the LOS path of the receiver is blocked.

described in section §6.4.2 were also used for this measurement performed in office 1. The same receiver location as in Fig. 6.3 was used, in order to have a meaningful comparison with the “non-blocked” case. Fig. 6.11(a) shows the frequency-averaged received power (in Watts) with the absorbers marked on the floor plan for the receiver at LOC 2.

Fig. 6.11(b) shows the frequency-averaged received power (in dBm) measured with a  $10^\circ$  angular resolution with the absorbers blocking the LOS path at LOC 2. In comparison, the results from Fig. 6.4(b), i.e. the “without blockage” case also shown in Fig. 6.11(b). When the LOS path of the receiver is shadowed by the absorbers, the received power is reduced to  $-23.4$  dBm at  $330^\circ$ . In comparison, when the absorbers were not blocking the LOS path, the received power was  $0.1$  dBm. This implies that the absorbers introduced approximately  $23.4$  dB attenuation to the LOS path. These findings are similar to those reported in the literature, e.g.,  $20$  dB attenuation is observed in [44] and [45] for a  $60$  GHz system shadowed by a human body.

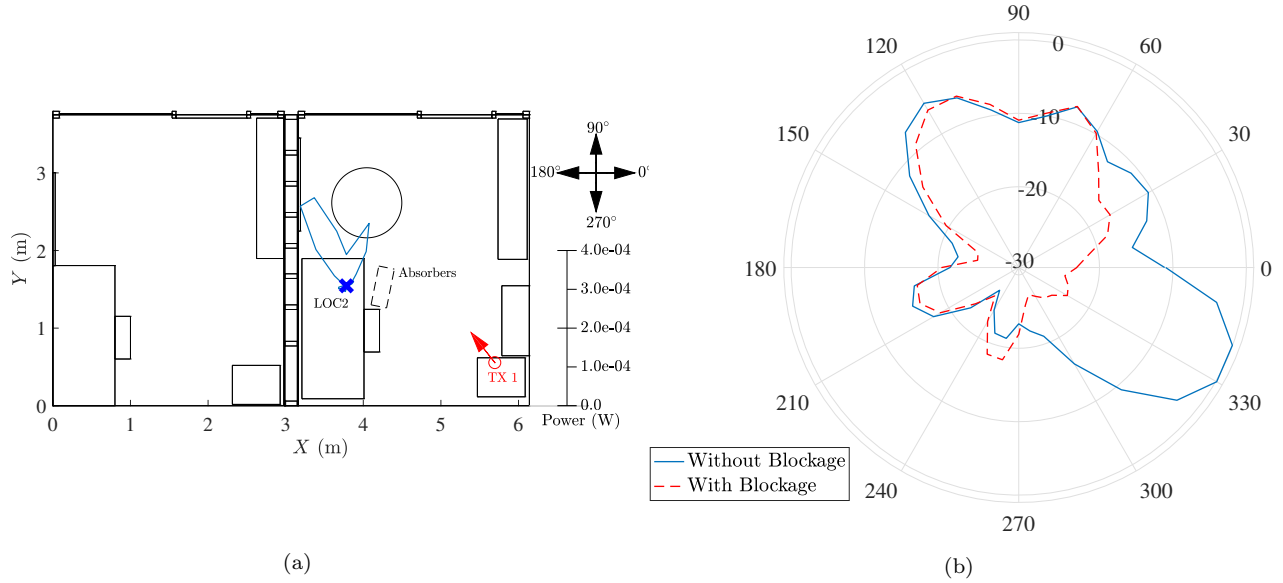


Fig. 6.11.: (b) The location of the absorbers shown on the floor plan. Also shown is the received power (in W). (a) The frequency-averaged received power (in dBm) at LOC 2 when a phantom is placed to block the LOS path.

Significantly, by blocking the LOS path, the first- and second-order reflections contributing to the multipath components at  $70^\circ$  and  $120^\circ$ , respectively, are the only propagation mechanisms that are dominant in this location.

## 6.6 Phase C: Inter-Office Measurements

In order to provide coverage to office 2 shown in Fig. 6.3, a separate millimetre wave access point could be deployed in this office. However, co-channel interference could occur, when this access point reuses the same frequency as the access point in office 1. As a consequence of this co-channel interference, the system performance, signal quality, and throughputs could be degraded below acceptable levels. The aim of the investigation described in this section is to analyse inter-office propagation, i.e., when the transmitter location is varied within office 2, and while the receiver is still located within the office 1.

In the first experiment, the transmitter is located on the desk in office 2 with an azimuth of  $0^\circ$ , such that the transmit antenna directly faces office 1. The transmit antenna height is 100.7 cm which is identical to the receiver antenna height located on the desk in office 1

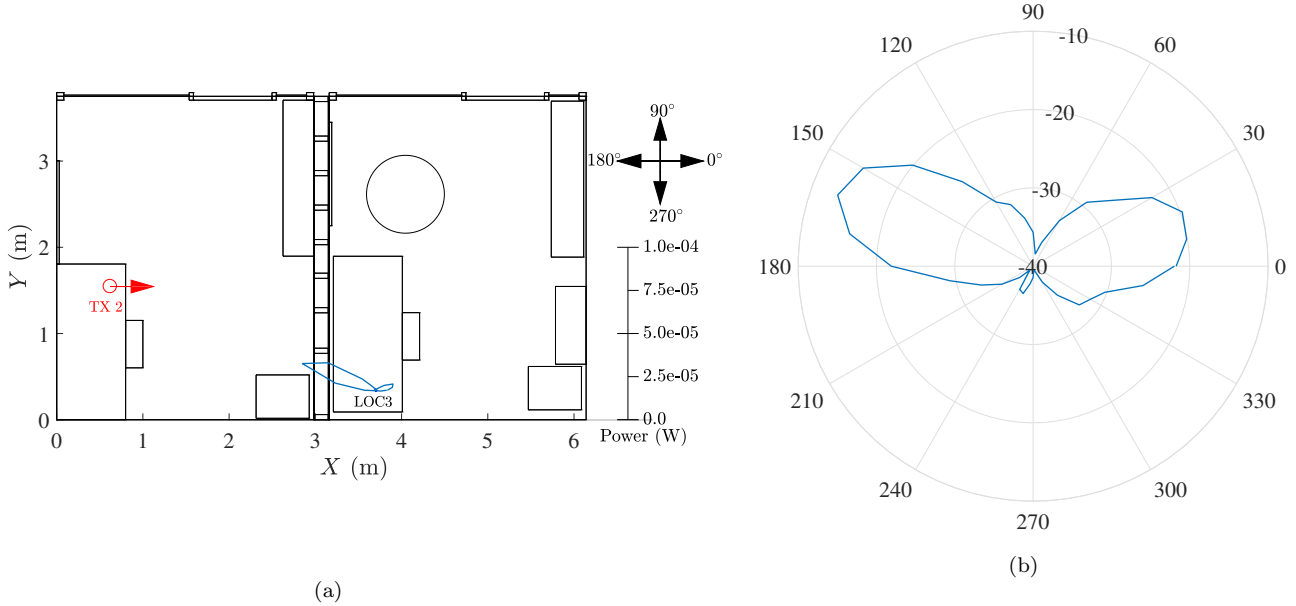


Fig. 6.12.: (a) The frequency-averaged received power (in Watts) at LOC 3 shown on the floor plan with TX 2, and (b) the polar plot of the frequency-averaged received power (in dBm) at LOC 3 from TX 2.

(refer to Table 6.2 for Phase A receiver antenna heights). The transmitter location in office 2 was chosen to emulate a potential dominant interference signal for the receivers positioned at LOC 2 and LOC 3 in office 1 (refer to Fig. 6.3 for Phase A receiver locations). Fig. 6.12(a) shows the location of the transmitter, TX 2, in office 2 and the receiver positioned at LOC 3 in office 1. Fig. 6.12(b) shows the frequency-averaged received power (in dBm) measured with a  $10^\circ$  angular resolution in the azimuth plane. In Fig. 6.12(b), two distinct multipath components above  $-30$  dBm are observed: the strongest component occurs at  $160^\circ$  (with  $P_r = -13.44$  dBm), which represents the LOS path, and a second strong component is observed at  $20^\circ$  (with  $P_r = -19.7$  dBm).

In comparison, when the receiver at LOC 3 and TX 1 were positioned within office 1, in Fig. 6.7(b) the received power was below  $-10$  dBm at all azimuth angles. Comparing Fig. 6.7(b) to Fig. 6.12(b) shows that the received power at  $160^\circ$  in Fig. 6.12(b) is 2.7 dB higher than the estimated LOS component at  $0^\circ$  in Fig. 6.7(b). The implication is that an interfering service from TX 2 could dominate the service from TX 1, in cases where the

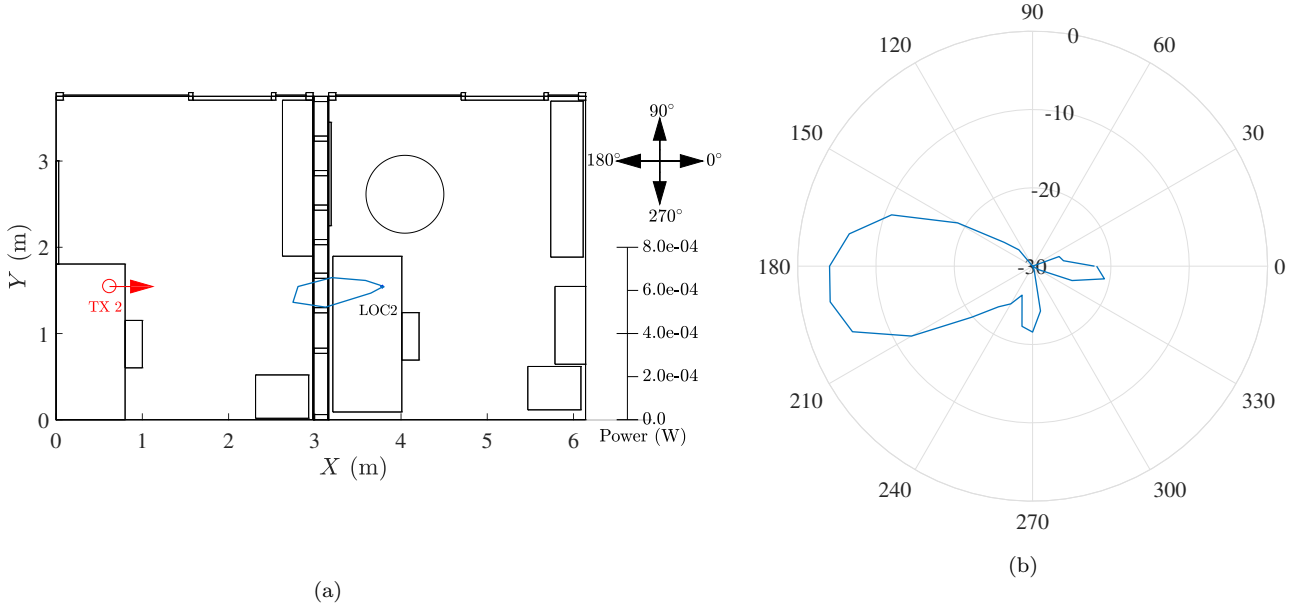


Fig. 6.13.: (a) The frequency-averaged received power (in Watts) at LOC 2 shown on the floor plan with TX 2, and (b) the polar plot of the frequency-averaged received power (in dBm) at LOC 2 from TX 2.

receiver does not measure any strong LOS component from TX 1 due to beam misalignment.

As shown in Fig. 6.13(a), while the transmitter location remains unchanged at TX 2, the receiver is moved to LOC 2. In this measurement configuration, the transmit and receive antennas become boresight aligned when the receiver antenna rotates to approximately 180°. Fig. 6.13(b) shows the polar plot of the frequency-averaged received power (in dBm) for this measurement configuration. The strongest component in Fig. 6.13(b) is received at 190° with  $P_r = -3.8$  dBm, which represents the direct path, and two other multipath components are observed at 270° and 0° with received powers below -20 dBm.

In comparison, when the LOS path of the receiver at LOC 2 was blocked by an absorber phantom representing a human body, in Fig. 6.11(b) the first- and second-order reflections received at 70° and 120° were the only dominant multipath components. In Fig. 6.13(b) the received power at 190° is 1.4 dB higher than the second-order reflected component at 120° in Fig. 6.11(b). This implies that blockage of the LOS path for a receiver in office 1 could result with a larger direct component to be received from TX 2. Accordingly, when

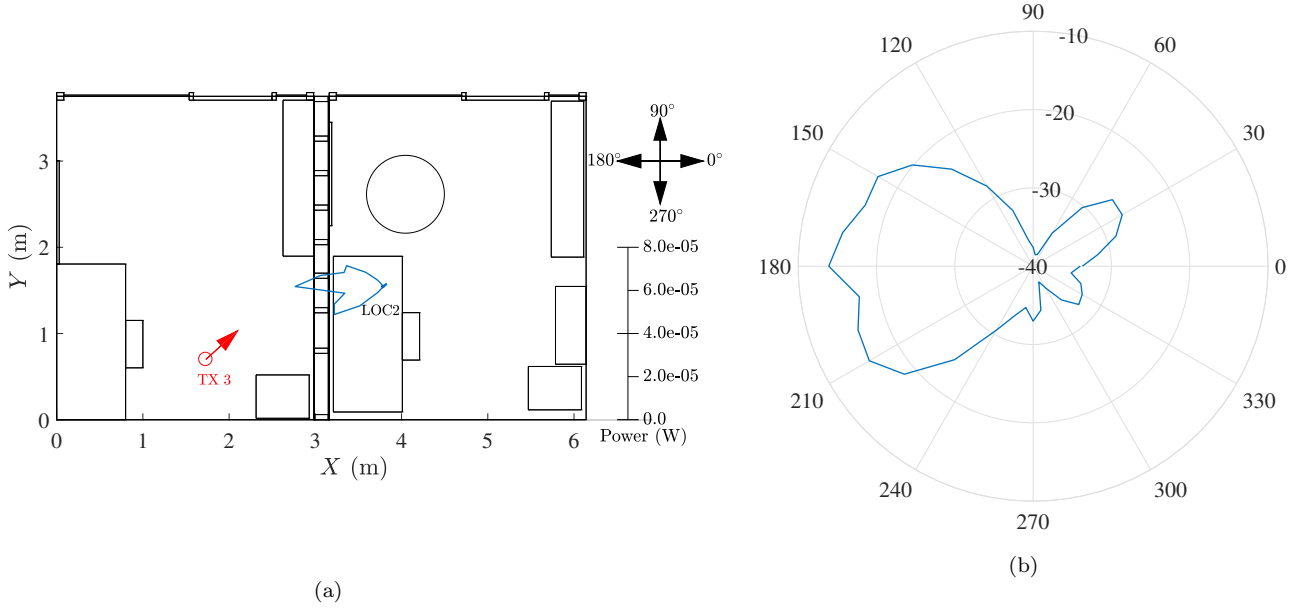


Fig. 6.14.: (a) The frequency-averaged received power (in Watts) at LOC 2 shown on the floor plan with TX 3, and (b) the polar plot of the frequency-averaged received power (dBm) at LOC 2 from TX 3.

the receiver in a shadowed region detects signals from TX 1 and TX 2 simultaneously, it could potentially prefer the weak interfering service from TX 2.

As shown in Fig. 6.14(a), the receiver at LOC 2 remains unchanged in office 1, while the transmitter, TX 3, is moved closer to the receiver. The orientation of the transmit antenna is varied, such that the azimuth is approximately  $40^\circ$ . In this configuration, TX 3 is elevated 124.5 cm from the ground and a mechanical downtilt of  $4^\circ$  is also applied to prevent overshoot of the receive antenna. Fig. 6.14(b) shows the frequency-averaged received power (in dBm) with three multipath components observed above  $-20$  dBm at azimuth angles  $210^\circ$ ,  $180^\circ$ , and  $150^\circ$ .

In contrast to Fig. 6.13(a), the timber studs in Fig. 6.14(a) obstruct the direct path between the TX 3 and the receiver at LOC 2. In Fig. 6.14(b) the timber studs give rise to the scattered multipath components observed at  $210^\circ$ ,  $180^\circ$ , and  $150^\circ$ . In comparison, the received power of the second-order reflected component at  $120^\circ$  in Fig. 6.11(b) is 8.71 dB higher than the strongest scattered component observed at  $180^\circ$  in Fig. 6.14(b). This implies

that the change of the location and transmitter parameters (antenna orientation and height) for TX 3 resulted in multipath components with weak received powers to be received from LOC 2. Specifically, the timber studs within the drywall are observed to obstruct the direct path, giving rise to scattered components.

## 6.7 Summary

For the LOS scenarios considered in the confined office environment, free-space propagation and reflection are the dominant propagation mechanisms at 60 GHz. Geometrical optics can be used to estimate the first- and second-order reflected components. The results of this analysis suggest that the LOS and second-order reflected waves contribute to the majority of the received power in a confined office environment.

The strong multipath components can result from strong reflectors within the office, such as, whiteboards, frosted glass windows, and metal door frames. When a strong reflection is supported at a given receiver location, the magnitude of the reflected component can be comparable to the LOS component. In particular, for shadowed regions, reflections resulting from the environment can become crucial. This observation was also made when the LOS path of the receiver was blocked by an absorber phantom representing a human body, resulting with an attenuation of 23.4 dB in the LOS path.

For NLOS scenarios, although the direct path is attenuated by the drywall, the received power from the direct path can dominate over the LOS component for a receiver in a shadowed region. For non-shadowed receiver locations, the magnitude of the received power of the direct path can be comparable to the reflected multipath components. For all measurements, antenna misalignment between the transmitter and receiver is shown to have a very strong impact on the received power levels.

## 7. RECOMMENDATIONS FOR FUTURE WORK

### 7.1 Introduction

In this chapter, recommendations for future investigations will be briefly discussed. Section §7.2 focuses on the hardware recommendations for the channel sounder. Future recommendations for indoor measurements will be considered in section § 7.3. Finally, section §7.3 provides a brief summary of this chapter.

### 7.2 System Hardware

In section 6.3, it was noted the measurement time for a single frequency sweep over the 1 GHz measurement bandwidth (with a 20 MHz resolution) is approximately 7.5 minutes. When an angular sweep is performed simultaneously in the azimuth plane with a 10° angular resolution, the total measurement time is approximately 3 hours for each receiver location. Importantly, the environment has to remain static between each measurement to have a meaningful comparison between measurements. The signal generation stage discussed in section 4.3 (with the oscilloscope feedback loop) are the main contributors to the long measurement time. It should be noted, however, that the entire baseband signal generation stage could be replaced with a more efficient ‘IQ signal generator’, e.g., an arbitrary waveform generator. Once the measurement time is reduced significantly, more measurement configurations and increased spatial resolution of the receiver location could be considered.

In Chapter 6, the transmit antenna orientation was fixed during the indoor office measurements. In future iterations of the channel sounder, the transmit antenna could also be rotated in the azimuth plane to investigate the best possible transmit antenna orientation for each receiver location. It was also noted that the misalignment in the boresights of the transmit and receive antennas resulted in increased path loss values in section §6.4.4. An omnidirectional antenna for the transmitter could be considered to reduce the impact of the beam misalignment.

## 7.3 Experimental Recommendations

### 7.3.1 LOS Measurement Recommendations

In the LOS measurement results presented in section §6.4.2, it was observed the whiteboard contributed significantly to the reflected components, resulting in high power levels. It would thus be interesting to remove the whiteboard and perform measurements to investigate the reflection from the wall. Additionally, the receiver could be positioned in the adjacent office to investigate inter-office propagation without the attenuation/reflection introduced by the whiteboard.

In Fig. 6.7(b) the received power levels at all azimuth angles is relatively low compared to other LOS locations, as no reflections/scattering from the environment was supported at this location, and the beam misalignment between the transmit and receive antennas was significantly high. To improve coverage to this region, an object with a smooth surface, i.e., a reflector, could be introduced in the environment, such that a strong multipath component is created for this location. Additionally, the transmit antenna azimuth and mechanical downtilt could also be varied specifically for this location to improve the received power levels and gain an insight into beam-steering requirements for future iterations of the channel sounder.

In section 6.5, the LOS path of the receiver was obstructed with an absorber phantom representing a human body. In this scenario, the receiver was positioned on the desk. However, in practice, obstructions with the human body can occur in various configurations, and as shown in Fig. 6.6(b) the received power of a reflected component can be comparable to the LOS path. In future measurements, obstructions by the human body from different azimuth angles could be investigated in more detail. Additionally, in real-world scenarios, more than one person could be present in an environment. In future measurements, two absorbers could be placed in the confined office environment to represent two people, such that additional to the LOS path, the strong multipath components are also obstructed.

### 7.3.2 NLOS Measurement Recommendations

In Fig. 6.14(b) the received power at LOC 2 was observed to be reduced when the transmitter was moved to a location where the timber studs within the drywall were obstructing the direct path. In order to predict potential interference challenges in future deployment of millimetre wave access points in adjacent offices, the following parameters could be investigated to quantify their impact on inter-office propagation: a) separation distance between transmit and receive antennas; b) position of timber stud framing within the drywall; c) the transmit and receive antenna heights; and d) beam misalignment between the transmit and receive antennas.

In Fig. 6.9(a) a strong direct component was observed when the receiver was positioned in the corridor. A frequency sweep with a fine resolution (e.g., 1 MHz) could be performed with aligned boresights of transmitting and receiving antennas to investigate the propagation through the glass over the 1 GHz channel bandwidth. Additionally, this measurement would also provide an indication of the penetration loss through the frosted glass window at 60 GHz.

In section 6.6, inter-office measurements between office 1 and office 2 have been considered. The received power levels in NLOS scenarios were relatively high, suggesting that dry wall partitions could be fairly transparent for inter-office propagation at millimetre wave frequencies. In practice, office 2 is adjacent to office 1, and another office, e.g., office 3. Each office could be deployed with a separate access point reusing the same frequency. In future measurements, propagation between confined offices that are not immediately adjacent to each other could also be investigated.

## 7.4 Summary

Recommendations for future investigation have been suggested in this chapter. The hardware recommendations for the system hardware focused on the signal generation stage

to reduce the measurement time. The experimental recommendations considered a number of LOS and NLOS measurement scenarios.

## 8. CONCLUSIONS

The propagation characteristics at millimetre wave frequencies necessitate an investigation of the indoor channel using experimental methods to gain insight into system deployment strategies. In particular, knowledge of how electromagnetic waves propagate in various indoor use-case scenarios is important for the design and deployment of future millimetre wave systems. While previous indoor studies mainly focused on propagation at 60 GHz in large indoor environments, this thesis has focused on experimentally investigating the angular-dependency of the 60 GHz channel in a confined office environment using a channel sounder.

The channel measurements presented in this thesis were performed with a channel sounder constructed using off-the-shelf components. This cost-effective and practical channel sounder enables a channel characterisation based on a swept-tone architecture. In particular, the millimetre wave channel is characterised over a 1 GHz bandwidth between 59.5 GHz and 60.5 GHz using pyramidal horn antennas for the transmitter and receiver. The performance of the channel sounder has been validated through comparisons to known theoretical propagation models. Specifically, the two-ray channel model was observed to agree well with the measured signal, when a higher order reflected component was taken into consideration.

The channel sounder has achieved the major objectives to experimentally investigate the propagation channel. However, there is scope to improve the hardware, specifically in the signal generation stage to reduce the duration of the measurements. In future iterations of the channel sounder, the signal generators used for generating the baseband frequency tone could be replaced with alternative solutions.

The indoor channel measurements presented in this thesis were performed with transmitter and receiver locations representing common use-case scenarios in a confined office with varying levels of environmental clutter. In particular, the experimental measurements

focused on the following characteristics of millimetre wave propagation: a) propagation within a confined office; b) inter-office propagation between two adjacent offices; and c) propagation mechanisms in the case when the LOS component is blocked by an absorber phantom representing a human body.

The measurement results from the confined office environment indicate that millimetre waves rely on the LOS path between the transmitter and receiver to achieve high power levels. The narrow beamwidth of pyramidal horn antennas can result in a large misalignment between the boresights of transmitting and receiving antennas. This beam misalignment is the main contributing factor to high path loss within a confined office. For example, in a LOS scenario, a receiver was found to receive weak power levels, where no LOS path existed. Alternative deployment solutions, such as transmit and receive antennas with three-dimensional beam-steering capability could help to improve the received power levels in such cases. The results in this thesis show that achieving adequate indoor coverage without utilising beam-steering antennas will be challenging, even in confined office environments.

The measurement results also show reflection is an important propagation mechanism at 60 GHz within a confined office. The strong reflectors in the environment, including whiteboards, metal door frames, and frosted glass windows, were found to give rise to first- and second-order reflected components with high corresponding power levels. These reflected components are particularly important when the LOS path between the transmitter and receiver is blocked, e.g., by the human body. In this scenario, the received power on the LOS path was attenuated by approximately 23 dB, and first- and second-order reflected components were the only propagation mechanisms providing a signal at this location. This is an important finding, as many user devices are hand-held. The implication is that receivers in confined office environments could frequently be shadowed by the user. The measurement results presented in this thesis suggest that objects with smooth surfaces in a confined office environment also need to be taken into consideration when developing deployment strategies for millimetre wave systems. In particular, objects with smooth surfaces could provide advantages, especially, for receivers operating in radio shadow regions.

This thesis also experimentally investigated propagation between two adjacent offices. The measurement results demonstrated that drywall is largely transparent at millimetre wave frequencies and may not be sufficient to isolate two transmitters (reusing the same frequencies) deployed in adjacent offices. The comparison between inter-office and LOS measurement results show that a receiver could potentially prefer the service from an interfering transmitter (in an adjacent office), in locations where the power levels from the ‘desired’ transmitter (in the same office) are weak. The implications are that interference mitigation techniques need to be considered in future millimetre wave systems (when the access points reuse the same frequencies) deployed in adjacent offices in close proximity to each other.

Wireless communication networks are facing new challenges as Internet usage continues to grow rapidly. The plentiful spectral resources available at millimetre wave bands (particularly at 60 GHz) are expected to be key to addressing these challenges in data growth. The millimetre wave communications are widely anticipated to usher in new capabilities for wireless networks and transform how people live and work. The measurement results presented in this thesis provide a preliminary understanding of millimetre wave propagation in confined office environments, and the channel sounder developed for this research may be utilised for future applications.

## APPENDICES

## A. AN ALTERNATIVE TRANSMITTER LOCATION

In section §6.4, the transmitter location was chosen to emulate a typical deployment of a millimetre wave access point in office 1. However, alternative transmitter locations can also be considered. In Fig. A.1(a) the transmitter is positioned on the bookshelf, such that the azimuth of the transmit antenna is  $180^\circ$ . In this case, the transmit antenna height is 139.4 cm and a mechanical downtilt of  $4^\circ$  is also applied. Fig. A.1(b) shows the polar plot of the frequency-averaged received power (in dBm) for the receiver positioned at LOC 1. In Fig. A.1(b) two strong multipath components are observed at  $330^\circ$  (with  $P_r = -0.4$  dBm) and at  $190^\circ$  (with  $P_r = 3.1$  dBm). The component observed at  $330^\circ$  corresponds to the LOS path, whereas the component at  $190^\circ$  is likely to arise from reflections or scattering in the environment.

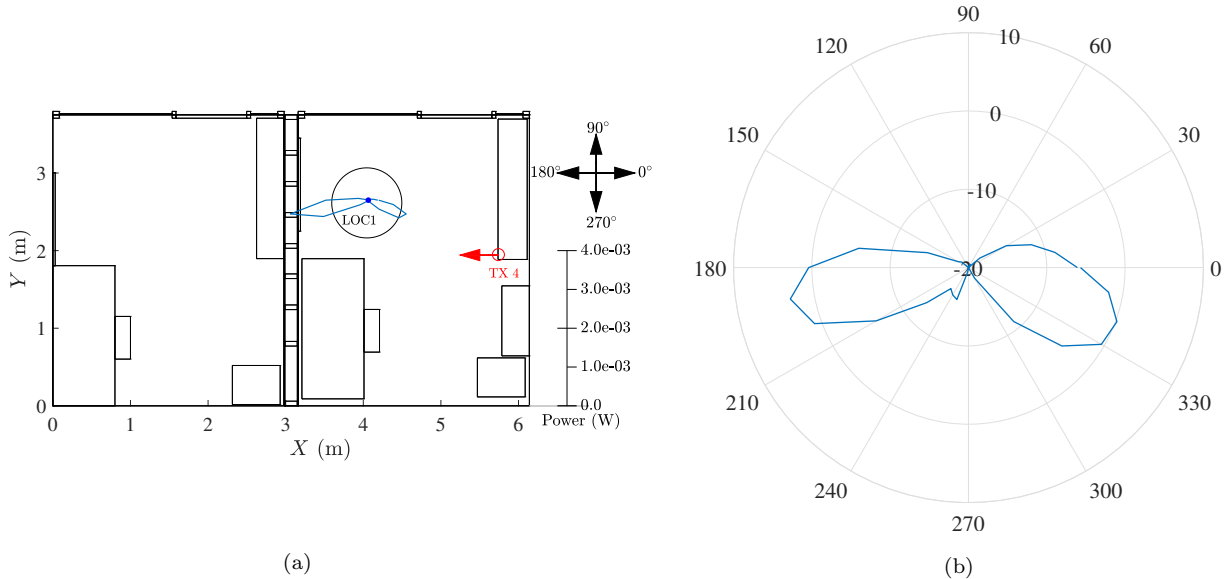


Fig. A.1.: (a) The frequency-averaged received power (W) at LOC 1 from TX 4 positioned on the bookshelf, and (b) the polar plot of the frequency-averaged received power (dBm) at LOC 1.

In Fig. 6.4(a) the received power on the LOS path was 7.6 dBm for the receiver also positioned at LOC 1. However, in this configuration TX 1 was located at the corner of office 1,

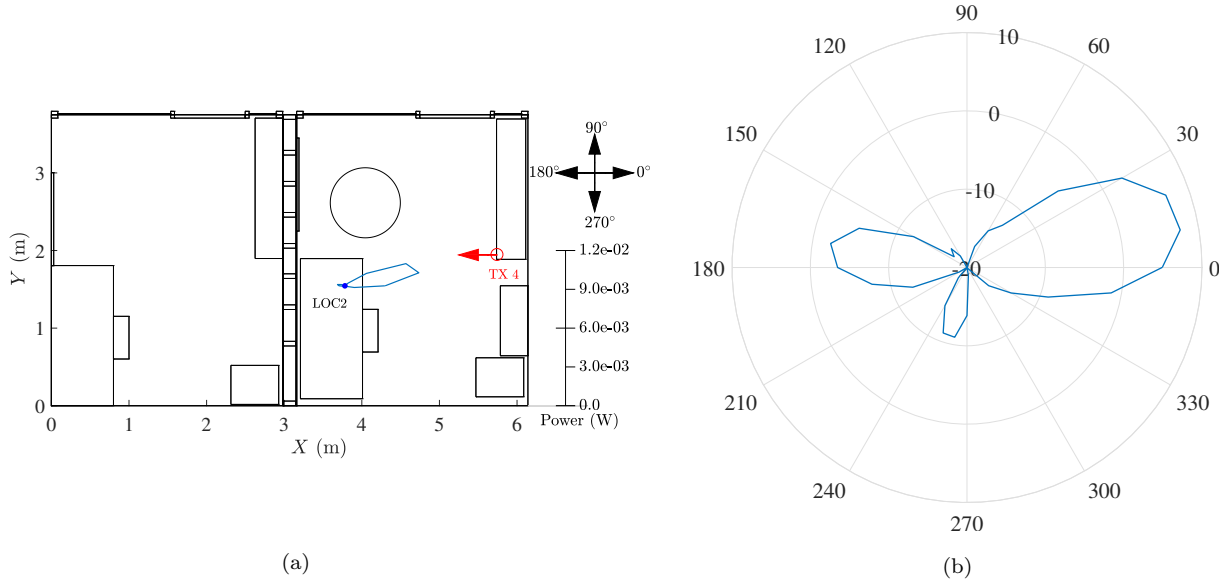


Fig. A.2.: (a) The frequency-averaged received power (W) at LOC 2 from TX 4 positioned on the bookshelf, and (b) the polar plot of the frequency-averaged received power (dBm) at LOC 2.

as shown in Fig. 6.3. When the transmitter is positioned on the bookshelf in Fig. A.1(a), the received power at  $330^\circ$  is reduced by approximately 8 dB compared to the LOS path in Fig 6.4(a). It should be noted that while TX 4 is moved physically closer to the receiver at LOC 1, the misalignment between the boresights of the transmit and receive antennas is increased, suggesting that the reduction in the received power could result from this beam misalignment.

As shown in Fig. A.2(a), TX 4 remains unchanged in office 1, while the receiver is moved to LOC 2. Fig. A.2(b) shows two components with power above  $-10$  dBm: the strongest component is observed at  $10^\circ$  with ( $P_r = 7.6$  dBm), corresponding to the LOS path, and the second strongest component is observed at  $170^\circ$  with ( $P_r = -2.3$  dBm), which is likely to arise from reflections or scattering in the environment.

In Fig. 6.4(b) the received power on the LOS path from TX 1 was  $0.1$  dBm, when the receiver was also positioned at LOC 2. The received power at  $10^\circ$  from TX 4 is increased by 7.5 dB compared to the LOS path in Fig. 6.4(b). This implies that moving the transmitter to the bookshelf improved the received power on the LOS path for the receiver at LOC 2.

## B. IMPACT OF INCREASED TRANSMITTER HEIGHT

An alternative transmitter location is considered in Fig. B.1(a). TX 5 is elevated 190 cm above the ground, and the azimuth of the transmit antenna is similar to TX 1 in Fig. 6.3. It should be noted that a mechanical downtilt of  $12^\circ$  was applied to the transmit antenna to receive powers above  $-10$  dBm at LOC 1, as shown in Fig. B.1(b). Fig. B.1(b) shows the polar plot of the frequency-averaged received power (in dBm) at LOC 1. The strongest multipath component is received at  $320^\circ$  (with  $P_r = -4.4$  dBm), which corresponds to the LOS path, and the components observed at  $210^\circ$  and  $130^\circ$  have received powers above  $-10$  dBm and are likely to arise from reflections or scattering in the environment.

In Fig. 6.4(a), when the height of the transmit antenna was 149.5 cm for TX 1 (mechanical downtilt= $4^\circ$ ), the received power at LOC 1 on the LOS path was 7.6 dBm. This implies that increasing the transmitter height reduced the received power on the LOS path by 12 dB. In particular, an additional mechanical downtilt of  $8^\circ$  was found to be necessary to improve the received power at LOC 1 from TX 5.

As shown in Fig. B.2(a), TX 5 remains unchanged in office 1, while the receiver is moved to LOC 2. In Fig. B.2(b) the strongest component is observed at  $70^\circ$  (with  $P_r = -9.7$  dBm), which is likely to arise from reflections or scattering in the environment and the second strongest component is observed at  $340^\circ$  (with  $P_r = -13.6$  dBm), representing the LOS path.

In Fig. 6.4(b), the received power at LOC 2 on the LOS path was 0.1 dBm. In comparison, when the transmitter height is increased in Fig. B.2(b), the received power at  $340^\circ$  corresponding to the LOS path is reduced by 13.7 dB.

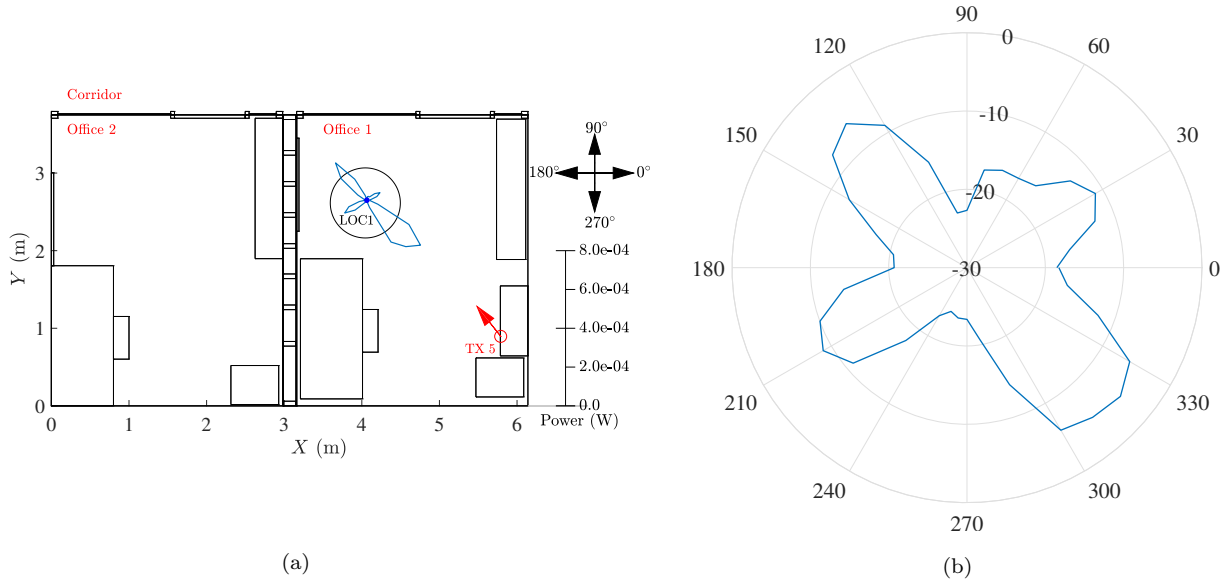


Fig. B.1.: (a) The frequency-averaged received power (W) at LOC 1 from TX 5 with increased transmitter height, and (b) the polar plot of the frequency-averaged received power (dBm) at LOC 1.

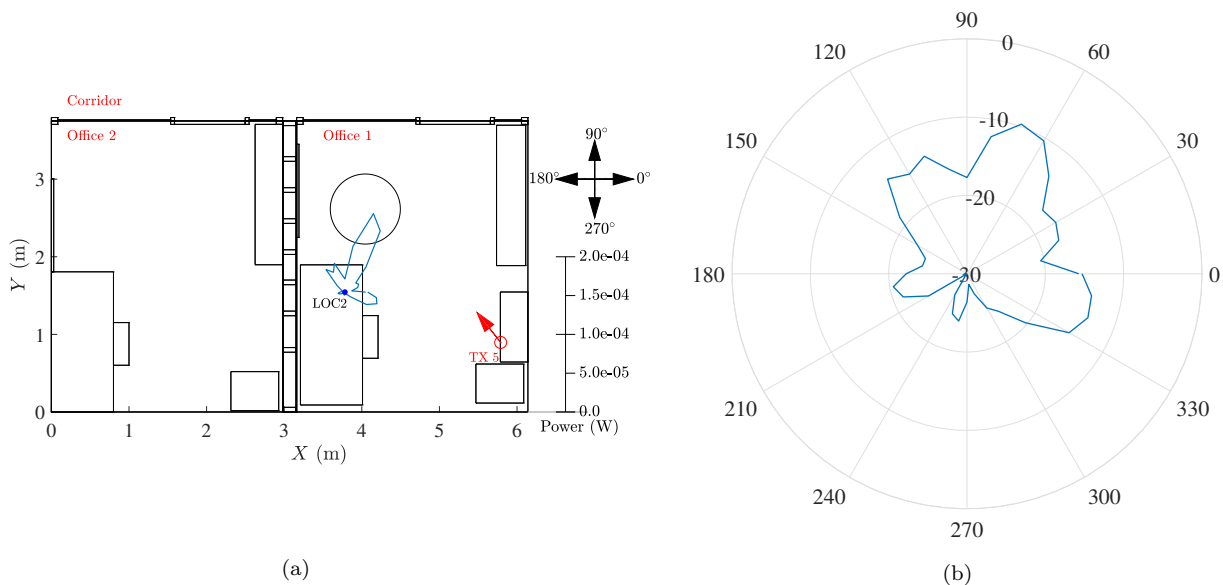


Fig. B.2.: (a) The frequency-averaged received power (W) at LOC 2 from TX 5 with increased transmitter height, and (b) the polar plot of the frequency-averaged received power (dBm) at LOC 2.

## C. ANALYSIS OF THE MULTIPATH COMPONENT

In Fig. 6.4(b) a multipath component was observed at  $70^\circ$  for a receiver positioned at LOC 2. The manually performed ray analysis in Fig. 6.5 indicated that a first-order reflection from the edge of the metal door frame gives rise to this component. In order to confirm the source of this component observed at  $70^\circ$ , absorbers are placed at the receiver height to cover the metal door frame, door handle and partially the frosted glass window adjacent to the metal frame, as shown in Fig. C.1(a). The transmitter and receiver locations remained unchanged to have a meaningful comparison to Fig. 6.4(b).

Fig. C.1(b) shows the received power (in dBm) with the absorbers blocking the metal door frame and adjacent materials. In comparison, the results from Fig. 6.4(b), i.e., the “without absorbers” case, is also shown in Fig. C.1(b). When the absorbers are present, the received power is reduced to  $-23.3$  dBm at  $70^\circ$ . In contrast, when the absorbers were not blocking the metal door frame (and adjacent materials), the received power was  $-7.7$  dBm. This implies that the absorbers introduced  $15.6$  dB attenuation on the component observed at  $70^\circ$ . Interestingly, there is a significant agreement between the two measurements for all the remaining azimuth angles, suggesting that the only change in the environment occurred at  $70^\circ$  (and  $30^\circ$ ).

It is evident from Fig. C.1(b) that the metal door frame and possibly the adjacent materials are giving rise to the component at  $70^\circ$ . Additionally, the received power of the component at  $30^\circ$  is reduced by approximately  $8$  dB, suggesting that introducing the absorbers in the environment also resulted in an attenuation on the received power of this component.

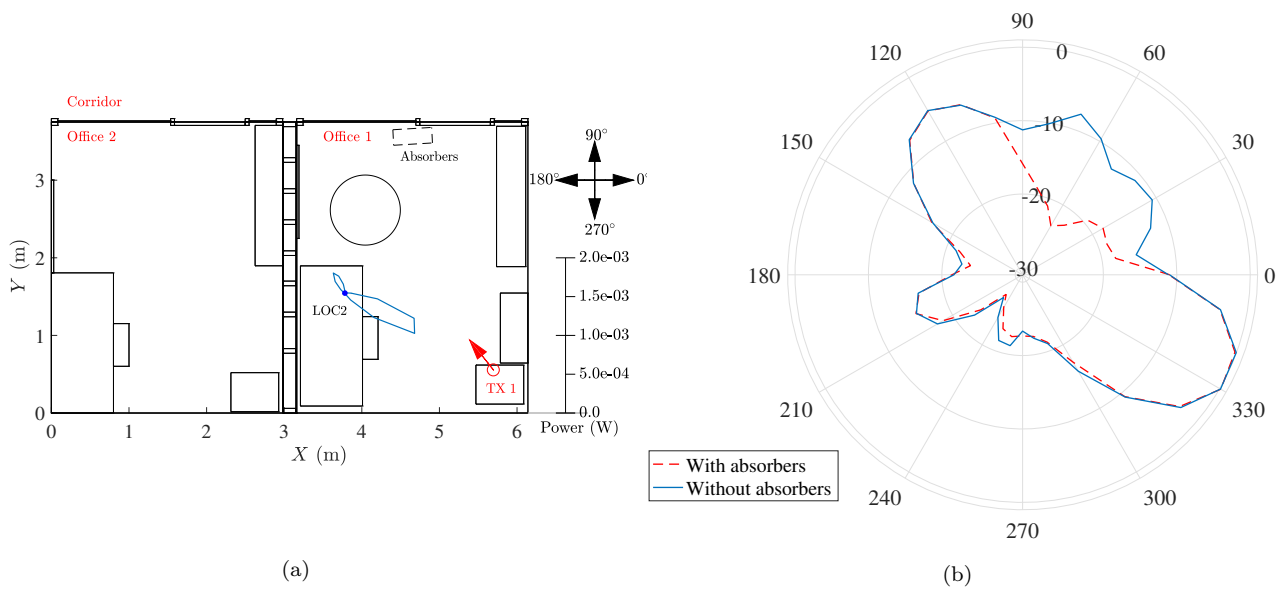


Fig. C.1.: (a) The frequency-averaged received power (W) at LOC 2 with the location of the absorbers shown on the floor plan, and (b) the polar plot of the frequency-averaged received power (dBm) at LOC 2, when absorbers are positioned to cover the source of the multipath component at  $70^\circ$ .

## REFERENCES

## REFERENCES

- [1] J. Korhonen, *Introduction to 4G Mobile Communications*. California: Artech House, 2014.
- [2] The evolution of mobile technologies: 1G, 2G, 3G and 4G. [Online]. Available: <https://www.qualcomm.com/media/documents/files/the-evolution-of-mobile-technologies-1g-to-2g-to-3g-to-4g-lte.pdf>
- [3] IEEE 5G and beyond technology roadmap white paper. [Online]. Available: <https://5g.ieee.org/images/files/pdf/ieee-5g-roadmap-white-paper.pdf>
- [4] Cisco visual networking index: Global mobile data traffic forecast update, 2016–2021 white paper. [Online]. Available: <https://www.cisco.com/c/en/us/solutions/collateral/service-provider/visual-networking-index-vni/mobile-white-paper-c11-520862.html>
- [5] S. Rangan, T. S. Rappaport, and E. Erkip, “Millimeter-wave cellular wireless networks: potentials and challenges,” *Proceedings of the IEEE*, vol. 102, no. 3, pp. 366–385, March 2014.
- [6] A. Ghosh, T. A. Thomas, M. C. Cudak, R. Ratasuk, P. Moorut, F. W. Vook, T. S. Rappaport, G. R. MacCartney, S. Sun, and S. Nie, “Millimeter-wave enhanced local area systems: a high-data-rate approach for future wireless networks,” *IEEE Journal on Selected Areas in Communications*, vol. 32, no. 6, pp. 1152–1163, June 2014.
- [7] Z. Pi and F. Khan, “An introduction to millimeter-wave mobile broadband systems,” *IEEE Communications Magazine*, vol. 49, no. 6, pp. 101–107, June 2011.
- [8] T. S. Rappaport, R. W. Heath Jr., R. C. Daniels, J. N. Murdock, *Millimeter Wave Wireless Communications*. United States: Prentice Hall, 2014.
- [9] The 1000x mobile data challenge, white paper. [Online]. Available: <https://www.qualcomm.com/media/documents/files/1000x-mobile-data-challenge.pdf>
- [10] Electronic Code for Federal Regulations: Part 15 - Radio Frequency Device Regulations. [Online]. Available: <http://fcc.gov/oet/info/rules>
- [11] R. C. Daniels, J. N. Murdock, T. S. Rappaport, and R. W. Heath, “60 GHz wireless: Up close and personal,” *IEEE Microwave Magazine*, vol. 11, no. 7, pp. 44–50, Dec 2010.
- [12] Planning for 60 GHz millimeter wave data communication link. [Online]. Available: [http://archive.acma.gov.au/WEB/STANDARD/pc=PC\\_2848](http://archive.acma.gov.au/WEB/STANDARD/pc=PC_2848)
- [13] Table of Radio Spectrum Usage in New Zealand (PIB 21), Issue 9.1, June 2017. [Online]. Available: <https://www.rsm.govt.nz/online-services-resources/pdf-and-documents-library/publications-and-guides/pibs/pib21>
- [14] Preparing for 5G in New Zealand Discussion Document, March 2018. [Online]. Available: <https://www.rsm.govt.nz/projects-auctions/current-projects/preparing-for-5g-in-new-zealand/technical-consultation/5g-spectrum-road-map-discussion-document.pdf>

- [15] H. J. Liebe, "MPM-An atmospheric millimeter-wave propagation model," *International Journal of Infrared and Millimeter Waves*, vol. 10, no. 6, pp. 631–650, Jun 1989.
- [16] D. Johnson. A beam-steering antenna for 5G mobile phones. [Online]. Available: <https://spectrum.ieee.org/tech-talk/telecom/wireless/a-beam-steering-antenna-for-real-world-mobile-phones>
- [17] K. R. Mahmoud and A. M. Montaser, "Design of dual-band circularly polarised array antenna package for 5G mobile terminals with beam-steering capabilities," *IET Microwaves, Antennas Propagation*, vol. 12, no. 1, pp. 29–39, 2018.
- [18] K. D. Wong, *Fundamentals of Wireless Communication Engineering Technologies*. United States: Wiley, 2011.
- [19] J.D.Parsons, *The Mobile Radio Propagation Channel*, 2nd ed. London: Wiley, 2000.
- [20] M. Rumney. Testing 5G: Time to throw away the cables. [Online]. Available: <https://pdfs.semanticscholar.org/d061/8b84b8bd97805009c677659feb83c590fc79.pdf>
- [21] T. S. Rappaport, E. Ben-Dor, J. N. Murdock, and Y. Qiao, "38 GHz and 60 GHz angle-dependent propagation for cellular amp; peer-to-peer wireless communications," in *2012 IEEE International Conference on Communications (ICC)*, June 2012, pp. 4568–4573.
- [22] J. Vehmas, J. Jarvelainen, S. L. H. Nguyen, R. Naderpour, and K. Haneda, "Millimeter-wave channel characterization at Helsinki airport in the 15, 28, and 60 GHz bands," in *2016 IEEE 84th Vehicular Technology Conference (VTC-Fall)*, Sept 2016, pp. 1–5.
- [23] A. Taflove and K. R. Umashankar, "Finite-difference time-domain (FD-TD) modeling of electromagnetic wave scattering and interaction problems," *IEEE Antennas and Propagation Society Newsletter*, vol. 30, no. 2, pp. 5–20, April 1988.
- [24] A. C. M. Austin, "Interference Modelling for Indoor Wireless Systems using Finite-Difference Time-Domain Method," Ph.D. dissertation, Auckland, New Zealand, 2011.
- [25] A. C. M. Austin, M. J. Neve, and G. B. Rowe, "Modeling propagation in multifloor buildings using the FDTD method," *IEEE Transactions on Antennas and Propagation*, vol. 59, no. 11, pp. 4239–4246, Nov 2011.
- [26] A. C. M. Austin, N. Sood, J. Siu, and C. D. Sarris, "Application of polynomial chaos to quantify uncertainty in deterministic channel models," *IEEE Transactions on Antennas and Propagation*, vol. 61, no. 11, pp. 5754–5761, Nov 2013.
- [27] C. A. L. Diakhate, J. M. Conrat, J. C. Cousin, and A. Sibille, "Millimeter-wave outdoor-to-indoor channel measurements at 3, 10, 17 and 60 GHz," in *2017 11th European Conference on Antennas and Propagation (EUCAP)*, March 2017, pp. 1798–1802.
- [28] H. Xu, V. Kukshya, and T. S. Rappaport, "Spatial and temporal characteristics of 60-GHz indoor channels," *IEEE Journal on Selected Areas in Communications*, vol. 20, no. 3, pp. 620–630, Apr 2002.
- [29] K. Haneda, J. Järveläinen, A. Karttunen, M. Kyrö, and J. Putkonen, "A statistical spatio-temporal radio channel model for large indoor environments at 60 and 70 GHz," *IEEE Transactions on Antennas and Propagation*, vol. 63, no. 6, pp. 2694–2704, June 2015.
- [30] R. J. Pirkle and G. D. Durgin, "Optimal sliding correlator channel sounder design," *IEEE Transactions on Wireless Communications*, vol. 7, no. 9, pp. 3488–3497, September 2008.

- [31] A. Hammoudeh, R. Stephens, and M. Al-Nuaimi, "Characterisation and modelling of scatter, attenuation and depolarisation of millimetre waves due to foliage," in *1996 26th European Microwave Conference*, vol. 2, Sept 1996, pp. 916–919.
- [32] C. X. Wang, F. Haider, X. Gao, X. H. You, Y. Yang, D. Yuan, H. M. Aggoune, H. Haas, S. Fletcher, and E. Hepsaydir, "Cellular architecture and key technologies for 5G wireless communication networks," *IEEE Communications Magazine*, vol. 52, no. 2, pp. 122–130, February 2014.
- [33] P. F. M. Smulders and A. G. Wagemans, "Wide-band measurements of mm-wave indoor radio channels," in *The Third IEEE International Symposium on Personal, Indoor and Mobile Radio Communications*, Oct 1992, pp. 329–333.
- [34] S. Geng, J. Kivinen, X. Zhao, and P. Vainikainen, "Millimeter-wave propagation channel characterization for short-range wireless communications," *IEEE Transactions on Vehicular Technology*, vol. 58, no. 1, pp. 3–13, Jan 2009.
- [35] C. R. Anderson and T. S. Rappaport, "In-building wideband partition loss measurements at 2.5 and 60 GHz," *IEEE Transactions on Wireless Communications*, vol. 3, no. 3, pp. 922–928, May 2004.
- [36] T. Zwick, T. J. Beukema, and H. Nam, "Wideband channel sounder with measurements and model for the 60 GHz indoor radio channel," *IEEE Transactions on Vehicular Technology*, vol. 54, no. 4, pp. 1266–1277, July 2005.
- [37] A. Maltsev, R. Maslennikov, A. Sevastyanov, A. Khoryaev, and A. Lomayev, "Experimental investigations of 60 GHz WLAN systems in office environment," *IEEE Journal on Selected Areas in Communications*, vol. 27, no. 8, pp. 1488–1499, October 2009.
- [38] H. Sawada, K. Fujita, S. Kato, K. Sato, and H. Harada, "Impulse response model for the cubicle environments at 60 GHz," in *2010 Asia-Pacific Microwave Conference*, Dec 2010, pp. 2131–2134.
- [39] M. Kyro, K. Haneda, J. Simola, K. Nakai, K. i. Takizawa, H. Hagiwara, and P. Vainikainen, "Measurement based path loss and delay spread modeling in hospital environments at 60 GHz," *IEEE Transactions on Wireless Communications*, vol. 10, no. 8, pp. 2423–2427, August 2011.
- [40] X. Wu, C. X. Wang, J. Sun, J. Huang, R. Feng, Y. Yang, and X. Ge, "60-GHz millimeter-wave channel measurements and modeling for indoor office environments," *IEEE Transactions on Antennas and Propagation*, vol. 65, no. 4, pp. 1912–1924, April 2017.
- [41] A. C. M. Austin, M. J. Neve, and D. Guven, "Indoor millimetre wave channel measurements for 5G wireless systems," *2018 12th European Conference on Antennas and Propagation (EUCAP)*, April 2018.
- [42] K. Haneda, J. Järveläinen, A. Karttunen, M. Kyrö, and J. Putkonen, "Indoor short-range radio propagation measurements at 60 and 70 GHz," in *The 8th European Conference on Antennas and Propagation (EuCAP 2014)*, April 2014, pp. 634–638.
- [43] S. Collonge, G. Zaharia, and G. E. Zein, "Influence of the furniture on 60 GHz radio propagation in a residential environment," in *2003 International Symposium on Signals, Circuits and Systems*, vol. 2, 2003, pp. 413–416 vol.2.
- [44] L. Zhang, A. McKernan, S. L. Cotton, and W. G. Scanlon, "The influence of elevation angle on 60 GHz near-body path gain," in *2018 12th European Conference on Antennas and Propagation (EUCAP)*, April 2018.

- [45] S. Collonge, G. Zaharia, and G. E. Zein, "Influence of the human activity on wide-band characteristics of the 60 GHz indoor radio channel," *IEEE Transactions on Wireless Communications*, vol. 3, no. 6, pp. 2396–2406, Nov 2004.
- [46] L. Simic, N. Perpinias, and M. Petrova, "60 GHz outdoor urban measurement study of the feasibility of multi-Gbps mm-wave cellular networks," in *2016 IEEE Conference on Computer Communications Workshops (INFOCOM WKSHPS)*, April 2016, pp. 554–559.
- [47] Texas Instruments, Dallas, TX, USA. ADC-WB-BB Balun User's Guide. [Online]. Available: <http://www.ti.com/lit/ug/snau123/snau123.pdf>
- [48] SiversIMA, Kista, Sweden. FC2121V/01 57–66 GHz Up-Converter with LO. [Online]. Available: [https://www.siversima.com/wp-content/uploads/FC2121V01\\_revB.pdf](https://www.siversima.com/wp-content/uploads/FC2121V01_revB.pdf)
- [49] ——. FC2221V/01 57–66 GHz Down-Converter with LO. [Online]. Available: [https://www.siversima.com/wp-content/uploads/FC2221V01\\_revA.pdf](https://www.siversima.com/wp-content/uploads/FC2221V01_revA.pdf)
- [50] Sage Millimeter, Torrance, CA, USA. SAR-1725-15-S2 WR-15 Pyramidal Horn Antenna. [Online]. Available: <https://www.sagemillimeter.com/content/datasheets/SAR-1725-15-S2.pdf>
- [51] Texas Instruments, Dallas, TX, USA. ADC12D1X00RFRB Reference Board Users Guide. [Online]. Available: <http://www.ti.com/lit/ug/snau017/snau017.pdf>
- [52] L. Smaini, *RF Analog Impairments Modeling for Communication Systems Simulation*, 1st ed. United Kingdom: Wiley, 2012.
- [53] B. Lathi, *Signal Processing and Linear Systems*. California: Berkeley-Cambridge, 1998.
- [54] G. Vallant, M. Epp, W. Schlecker, U. Schneider, L. Anttila, and M. Valkama, "Analog IQ impairments in Zero-IF radar receivers: Analysis, measurements and digital compensation," in *2012 IEEE International Instrumentation and Measurement Technology Conference Proceedings*, May 2012, pp. 1703–1707.
- [55] R. Svitek and S. Raman, "DC offsets in direct-conversion receivers: characterization and implications," *IEEE Microwave Magazine*, vol. 6, no. 3, pp. 76–86, Sept 2005.
- [56] B. Razavi, "Design considerations for direct-conversion receivers," *IEEE Transactions on Circuits and Systems II: Analog and Digital Signal Processing*, vol. 44, no. 6, pp. 428–435, Jun 1997.
- [57] D. Korpi, T. Riihonen, V. Syrjälä, L. Anttila, M. Valkama, and R. Wichman, "Full-duplex transceiver system calculations: analysis of ADC and linearity challenges," *IEEE Transactions on Wireless Communications*, vol. 13, no. 7, pp. 3821–3836, July 2014.
- [58] Texas Instruments, Dallas, TX, USA. ADC12D1800RF 12-Bit, Single 3.6 GSPS RF Sampling ADC. [Online]. Available: <http://www.ti.com/lit/ds/symlink/adc12d1800rf.pdf>
- [59] M. J. Neve, "Mobile Radio Propagation Prediction in Built-Up Environments Using Ray-Methods," Ph.D. dissertation, Auckland, New Zealand, 1992.
- [60] R. E. Collin, *Antennas and Radiowave Propagation*. Singapore: McGraw-Hill College, 1985.
- [61] W. L. Stutzman and G. A. Thiele, *Antenna Theory and Design*, 2nd ed. New York: Wiley, 1981.

- [62] everythingRF. WR15 Specifications. [Online]. Available: <https://www.everythingrf.com/tech-resources/waveguides-sizes/wr15>
- [63] A. Goldsmith, *Wireless Communications*, 3rd ed. New York: Cambridge University Press, 2005.
- [64] R. A. Serway and J. W. Jewett, *Physics for Scientists and Engineers with Modern Physics*, 8th ed. California: Cengage Learning, 2010.
- [65] S. Deng, M. K. Samimi, and T. S. Rappaport, “28 GHz and 73 GHz millimeter-wave indoor propagation measurements and path loss models,” in *2015 IEEE International Conference on Communication Workshop (ICCW)*, June 2015, pp. 1244–1250.